

Directly imaging damped Ly α galaxies at $z > 2$. II: Imaging and spectroscopic observations of 32 quasar fields.

Michele Fumagalli^{1,2*}, John M. O’Meara³, J. Xavier Prochaska^{4,5}, Nissim Kanekar⁶, Arthur M. Wolfe⁷

¹Institute for Computational Cosmology, Department of Physics, Durham University, South Road, Durham, DH1 3LE, UK

²Carnegie Observatories, 813 Santa Barbara Street, Pasadena, CA 91101, USA

³Department of Chemistry and Physics, Saint Michael’s College, One Winooski Park, Colchester, VT 05439, USA

⁴Department of Astronomy and Astrophysics, University of California, 1156 High Street, Santa Cruz, CA 95064 USA

⁵University of California Observatories, Lick Observatory 1156 High Street, Santa Cruz, CA 95064 USA

⁶National Centre for Radio Astrophysics, TIFR, Post Bag 3, Ganeshkhind, Pune 411 007, India

⁷Department of Physics, and Center for Astrophysics and Space Sciences, University of California, San Diego, 9500 Gilman Dr., La Jolla, CA 92093-0424, USA

Accepted xxxx. Received xxxx; in original form xxxx

ABSTRACT

Damped Ly α absorbers (DLAs) are a well-studied class of absorption line systems, and yet the properties of their host galaxies remain largely unknown. To investigate the origin of these systems, we have conducted an imaging survey of 32 quasar fields with intervening DLAs between $z \sim 1.9 - 3.8$, leveraging a technique that allows us to image galaxies at any small angular separation from the background quasars. In this paper, we present the properties of the targeted DLA sample, new imaging observations of the quasar fields, and the analysis of new and archival spectra of the background quasars.

Key words: galaxies: star formation – galaxies: evolution – galaxies: high-redshift – quasars: absorption lines – ultraviolet: ISM – ISM: atoms

1 INTRODUCTION

Damped Ly α absorbers (DLAs), the strongest H I absorption line systems detected in the foreground of UV-bright sources, are easily identifiable in the spectra of high redshift quasars, to the point that recent surveys have uncovered more than 6000 DLAs (e.g. Prochaska & Wolfe 2009; Noterdaeme et al. 2009, 2012a) above $z \gtrsim 2$. Thanks to this large parent sample and dedicated follow-up observations, the statistical properties of DLAs, including their hydrogen distribution, their metallicity, and kinematics, are currently well measured between $z \sim 2 - 4$ (e.g. Prochaska et al. 2003a, 2007; Prochaska & Wolfe 2009; Noterdaeme et al. 2009, 2012a; Rafelski et al. 2012; Jorgenson et al. 2013; Rafelski et al. 2014; Neeleman et al. 2013; Møller et al. 2013; Zafar et al. 2013). However, despite this detailed knowledge of the DLA properties, a fundamental question still remains open: what is the typical galaxy population that gives rise to DLAs?

The quest to find DLA host galaxies¹ is a long-standing one (for a review, see Wolfe et al. 2005). More than 40 years after the discovery of DLAs (Wolfe et al. 1986), many attempts to iden-

tify DLA galaxies have been pursued (see e.g. Appendix B in Fumagalli et al. 2010), most of which have been unsuccessful. At least two reasons can justify the current lack of large samples of DLA galaxies. First, in order to detect $z \gtrsim 2$ galaxies in proximity or superimposed to bright ($m \lesssim 20$) quasars, observers face the challenging task of detecting faint sources against background fluxes that are at least a few orders of magnitude brighter (e.g. Møller & Warren 1998). This is especially true for galaxies lacking strong Ly α emission. Second, if in fact a substantial fraction of DLA galaxies are fainter than ~ 25 mag, as suggested by most theoretical studies (Nagamine et al. 2007; Cen 2012) and some observations (e.g. Fynbo et al. 1999; Rauch et al. 2008), then very deep imaging surveys are needed. And while current 8–10 m telescopes can reach sensitive detection limits for imaging ($m \gtrsim 26 - 27$ mag), at these magnitudes, spectroscopic redshifts for the candidate DLA galaxies are extremely difficult (if not impossible) to obtain. Furthermore, the number of candidates detected in proximity to the quasars rapidly increases as one probes the fainter end of the galaxy luminosity function, increasing the number of low- and high-redshift interlopers.

Despite these challenges, previous efforts and especially more recent searches that have employed efficient spectroscopic techniques (e.g. Fynbo et al. 2010; Péroux et al. 2011; Noterdaeme et al. 2012b; Jorgenson & Wolfe 2014), have resulted in a dozen confirmed DLA galaxies. While useful for some in-

* E-mail: michele.fumagalli@durham.ac.uk

¹ We will often refer to the system seen in absorption as “DLA gas” or simply DLA, while we will refer to the (candidate) host galaxy as “DLA galaxy”.

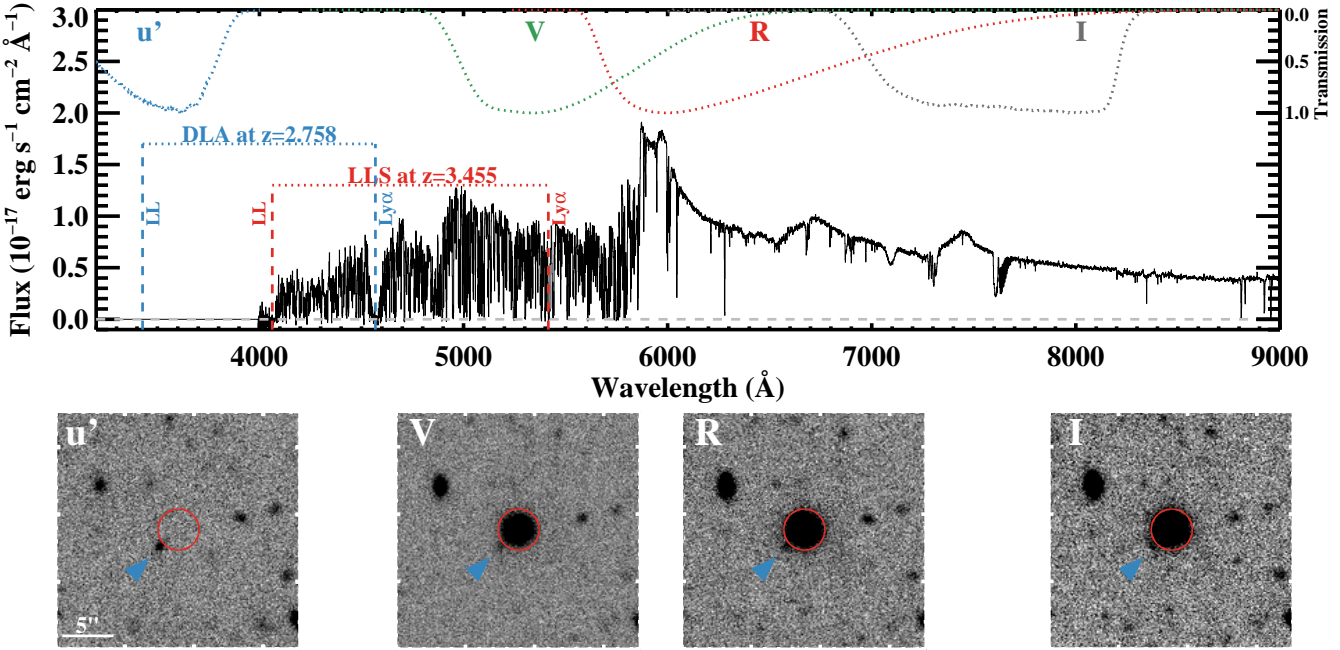


Figure 1. (Top:) ESI/Keck spectrum of the quasar J094927+111518 with, superimposed, the mirrored transmission curves of the u' , V , R , and I filters of LRIS at Keck. The corresponding y-axis of the transmission curves is shown on the top right. The Ly α line and the Lyman limit of the targeted DLA and of the LLS that acts as a blocking filter are also marked. (Bottom:) LRIS/Keck images of a $20'' \times 20''$ region centered at the quasar position in these four filters. Because of the intervening LLS, the quasar light which dominates the inner $\sim 2''$ (red circles) in the redder filters is instead completely absorbed in the u' band. This enables the detection of faint galaxies at all impact parameters, including objects that are aligned or in close proximity to the quasar location. The blue arrow highlights one such galaxy.

vestigations (Krogager et al. 2012), this sample is obviously small compared to the known DLAs or compared to the galaxy populations that are selected with imaging techniques (e.g. the Lyman break galaxies or LBGs). Furthermore, the sample of confirmed host galaxies includes both serendipitous discoveries and targeted observations of DLAs, which have been pre-selected according to their absorption properties. It is therefore difficult to establish a rigorous census of non detections, critical to empirically constrain the luminosity function of DLA hosts.

To overcome some of these limitations, we have undertaken a new imaging survey that targets 32 quasar fields with intervening DLAs between $z \sim 1.9 - 3.8$. As we discuss in the following sections, this sample represents an unbiased selection with respect to DLA hydrogen column densities and metallicities. Moreover, we have targeted fields blindly, that is without prior knowledge of the presence of DLA galaxy candidates near the quasars. Therefore, the census of candidate DLA galaxies in these fields is representative of the generic population of DLAs, simply defined as absorbers with $\log N_{\mathrm{HI}} \geq 20.3 \text{ cm}^{-2}$. Our survey resembles some of the previous HST imaging searches that have targeted quasar fields known to host absorbers which are representative of the general DLA population. Among those, we recall the survey conducted by Warren et al. (2001), who imaged 16 quasar fields with $z \sim 1.8 - 4.0$ DLAs across a wide range of column densities, extending the pioneering search for intermediate-redshift absorbers by Le Brun et al. (1997). A novel key element in our survey, however, is the use of the technique discussed in Section 2, which takes advantage of the presence of high-redshift absorption line systems along the line of sight to “block” the quasar glare (Steidel & Hamilton 1992; O’Meara et al. 2006; Christensen et al. 2009; Fumagalli et al. 2010). This tech-

nique allows us to achieve the same sensitivity at any distance from the quasars, including angular separations as small as $\sim 0.2 - 1''$. However, as it will become clear from the following analysis, our deep imaging observations uncover galaxies that are fainter than $m \sim 25$ mag, the limit beyond which spectroscopic follow-up is currently too expensive even with the largest ground-based telescopes. Therefore, our study will be limited to a statistical analysis, which nevertheless will offer unique constraints on the properties of DLA galaxies.

This paper presents the results of our imaging campaign based on the mentioned technique which avoids the contamination from background quasars. The design of the survey has been presented in the first paper of the series (Fumagalli et al. 2010). Here, after a brief review of the adopted technique and of the sample selection (Section 2), we present new ground-based and space-based imaging observations for the 32 quasar fields, together with new and archival spectra of the studied quasars (Section 3 and Section 4). In the third paper of the series (Fumagalli et al. in prep.), we will use these data to study the *in-situ* SFRs of DLAs and the connection between DLAs and star-forming galaxies, also in comparison to previous work.

In this work, unless otherwise noted, distances are in proper units and magnitudes are in the AB system, and we adopt the following cosmological parameters: $H_0 = 70.4 \text{ km s}^{-1} \text{ Mpc}^{-1}$, $\Omega_m = 0.27$ and $\Omega_\Lambda = 0.73$ (Komatsu et al. 2011).

2 TECHNIQUE AND SAMPLE SELECTION

To overcome the glare of the background quasar that would preclude the detection of faint galaxies at small projected sep-

Table 1. Summary of the sample properties.

Field ^a	R.A. ^b (J2000)	Dec. ^b (J2000)	z_{qso}^c	z_{dla}^d	z_{lls}^e	$\lambda_{\text{LL,dla}}^f$ (Å)	$\lambda_{\text{LL,lls}}^g$ (Å)	$N_{\text{HI,dla}}^h$ (log cm $^{-2}$)	$N_{\text{HI,lls}}^i$ (log cm $^{-2}$)	$[\text{X/H}]_{\text{dla}}^l$	Element ^m
1:G1	21:14:43.95	-00:55:32.7	3.424	2.9181	3.4420	3572	4050	20.25 ± 0.10	$> 20.0^*$	-0.63 ± 0.11	S
2:G2	07:31:49.50	+28:54:48.6	3.676	2.6878	3.6080	3362	4201	20.60 ± 0.10	> 17.6	-1.45 ± 0.17	Si
3:G3	09:56:04.43	+34:44:15.5	3.427	2.3887	3.3958	3090	4008	21.10 ± 0.15	> 17.5	-1.00 ± 0.17	Zn
4:G4	23:43:49.41	-10:47:42.0	3.616	2.6878	3.3652	3362	3980	20.60 ± 0.10	> 17.5	-1.27 ± 0.20	Si,Zn
5:G5	03:43:00.88	-06:22:29.9	3.623	2.5713	3.5071	3256	4109	20.75 ± 0.20	19.95 ± 0.15	-2.02 ± 0.26	Fe
6:G6	23:51:52.80	+16:00:48.9	4.694	3.7861	4.5835	4364	5091	20.85 ± 0.10	> 17.7	-2.03 ± 0.20	Fe
7:G7	00:42:19.74	-10:20:09.4	3.880	2.7544	3.6287	3423	4220	20.20 ± 0.10	> 17.7	-0.96 ± 0.16	Fe
8:G9	09:49:27.88	+11:15:18.2	3.824	2.7584	3.4559	3427	4063	20.85 ± 0.10	> 17.6	-0.95 ± 0.10	Si
9:G10	10:18:06.28	+31:06:27.2	3.629	2.4592	3.4812	3154	4086	20.35 ± 0.10	20.10 ± 0.10	-1.19 ± 0.28	Si,Zn
10:G11	08:51:43.72	+23:32:08.9	4.499	3.5297	4.4671	4130	4985	21.10 ± 0.10	> 17.8	-1.05 ± 0.15	Zn
11:G12	09:56:05.09	+14:48:54.7	3.435	2.6606	3.4759	3338	4081	20.85 ± 0.10	$20.70 \pm 0.10^*$	-1.46 ± 0.12	Si
12:G13	11:51:30.48	+35:36:25.0	3.581	2.5978	3.4193	3280	4029	20.90 ± 0.10	> 17.5	-1.28 ± 0.11	Si
13:H1	21:23:57.56	-00:53:50.1	3.583	2.7803	3.6251	3447	4217	20.70 ± 0.10	$> 20.6^*$	-1.59 ± 0.15	Si,Zn
14:H2	04:07:18.06	-44:10:14.0	3.000	1.9127	2.6215	2656	3302	20.55 ± 0.10	20.45 ± 0.10	-0.77 ± 0.11	Si
15:H3	02:55:18.58	+00:48:47.6	3.996	3.2530	3.9147	3878	4481	20.60 ± 0.10	$> 21.0^*$	-0.80 ± 0.11	Si
16:H4	08:16:18.99	+48:23:28.4	3.582	2.7067	3.4366	3380	4045	20.70 ± 0.15	20.70 ± 0.15	-2.36 ± 0.15	Si
17:H5	09:30:51.93	+60:23:01.1	3.719	3.0010	3.6373	3648	4228	21.05 ± 0.15	20.40 ± 0.20	-	-
18:H6	09:08:10.36	+02:38:18.7	3.710	2.9586	3.4071	3609	4018	21.10 ± 0.10	20.80 ± 0.20	-0.93 ± 0.12	Si
19:H7	12:20:21.39	+09:21:35.7	4.133	3.3069	4.1215	3927	4670	20.40 ± 0.20	> 17.5	-2.48 ± 0.22	-
20:H8	14:42:33.01	+49:52:42.6	3.175	2.6320	3.1124	3312	3750	20.35 ± 0.15	20.25 ± 0.20	-	-
21:H9	08:44:24.24	+12:45:46.7	2.482	1.8639	2.4762	2611	3169	21.00 ± 0.10	20.80 ± 0.10	-1.54 ± 0.12	Si
22:H10	07:51:55.10	+45:16:19.6	3.341	2.6826	3.2554	3358	3880	20.50 ± 0.10	> 17.5	-1.16 ± 0.13	Si
23:H11	08:18:13.14	+07:20:54.9	4.177	3.2332	3.8399	3860	4413	21.15 ± 0.10	> 17.5	-1.41 ± 0.25	Si,Zn
24:H12	08:18:13.05	+26:31:36.9	4.179	3.5629	4.1629	4160	4707	20.65 ± 0.10	$20.90 \pm 0.15^*$	-0.93 ± 0.24	Si,Zn
25:H13	08:11:14.32	+39:36:33.2	3.073	2.6500	3.0427	3328	3686	20.70 ± 0.15	$> 20.0^*$	-1.44 ± 0.15	Si,Zn
26:H14	15:08:51.94	+51:56:27.7	3.804	2.7333	3.5865	3404	4182	20.30 ± 0.20	20.80 ± 0.20	-	-
27:H15	10:54:30.07	+49:19:47.1	3.998	2.9236	3.7016	3577	4287	20.45 ± 0.15	> 17.4	-	-
28:H16	09:56:25.16	+47:34:42.5	4.478	3.4035	4.2441	4015	4781	21.05 ± 0.10	20.80 ± 0.15	$(-2.09, -1.50)^1$	Si,Ni
29:H17	14:41:47.52	+54:15:38.1	3.467	2.6289	3.3302	3309	3948	20.70 ± 0.15	20.30 ± 0.15	-	-
30:H18	11:55:38.60	+05:30:50.5	3.475	2.6079	3.3260	3290	3944	20.35 ± 0.15	21.00 ± 0.10	-1.60 ± 0.16	Si
31:H19	15:24:13.35	+43:05:37.4	3.920	2.8721	3.8802	3530	4450	20.40 ± 0.15	20.65 ± 0.15	-	-
32:H20	13:20:05.97	+13:10:15.3	3.352	2.6722	3.3411	3348	3958	20.30 ± 0.10	19.50 ± 0.15	-2.30 ± 0.10	Si

^a ID of the field. ^b Right ascension and declination of the quasar. ^c Quasar redshift. ^d Redshift of the targeted DLA. ^e Redshift of the LLS acting as blocking filter. ^f Wavelength corresponding to the Lyman limit of the targeted DLA. ^g Wavelength corresponding to the Lyman limit of the higher redshift LLS. ^h H I column density of the DLA. ⁱ H I column density of the higher redshift LLS. Asterisks mark DLAs that are proximate to the quasars and for which measurements are more uncertain. ^l DLA metallicity. ^m Tracer element used for the metallicity measurement. ¹ The listed values bracket the range of allowed metallicity given upper/lower limits.

arations, we select quasar fields that host both a DLA and a second optically-thick absorber along the line of sight. This “Lyman limit technique” has been already discussed elsewhere (Steidel & Hamilton 1992; O’Meara et al. 2006; Christensen et al. 2009; Fumagalli et al. 2010) and it is only briefly summarized in this section.

We select quasar fields in which there are two optically-thick absorbers, the targeted DLA at redshift z_{dla} and a second optically-thick absorber at redshift z_{lls} that acts as a “blocking filter” for the quasar light. For this survey, we primarily select sightlines from the Sloan Digital Sky Survey (SDSS) DR5 quasar catalogue (Schneider et al. 2007), with the addition of few quasars that lie outside of the SDSS footprint, but for which archival spectra are available. To be considered for imaging follow-up, a quasar has to exhibit a DLA in its optical spectrum, which results in a redshift lower limit of $z_{\text{dla}} \gtrsim 2.3$ for SDSS spectra, and a lower limit of $z_{\text{dla}} \gtrsim 1.8$ for archival spectra with extended blue coverage down to the atmospheric cutoff. Further, each sightline has to have a second, optically-thick absorber with redshift z_{lls} such that the Lyman limit of this system ($\lambda_{\text{LL,lls}}$) falls redward to the transmission curve of the blue filters available at ground-based observatories, or in the UVIS channel of the Wide Field Camera 3 (WFC3) camera

on board of the *Hubble Space Telescope* (HST). The filter choice is further dictated by the DLA redshift in order to prevent the Lyman limit of the DLA ($\lambda_{\text{LL,dla}}$) from entering the transmission curve of the selected filter, or at least to minimize the impact of the intrinsic Lyman limit absorption on the final images.

As shown by Figure 1, these conditions ensure that the quasar light and the light of the galaxy associated with the high-redshift Lyman limit system (LLS) are fully blocked to avoid contamination in the selected blue filters. The above selection criteria restrict the number of quasars for which this experiment can be performed in SDSS/DR5 (plus a few sightlines in the southern sky with known DLAs) to several tens of sightlines, 32 of which enter our final sample purely because of optimal scheduling of the imaging observations. The sample properties are summarized in Table 1. Twenty of these quasar fields (hereafter the HST sample, labeled by the letter “H”) have been selected for imaging with HST, while twelve additional fields have been imaged using ground-based facilities (hereafter the ground-based sample, labeled by the letter “G”).

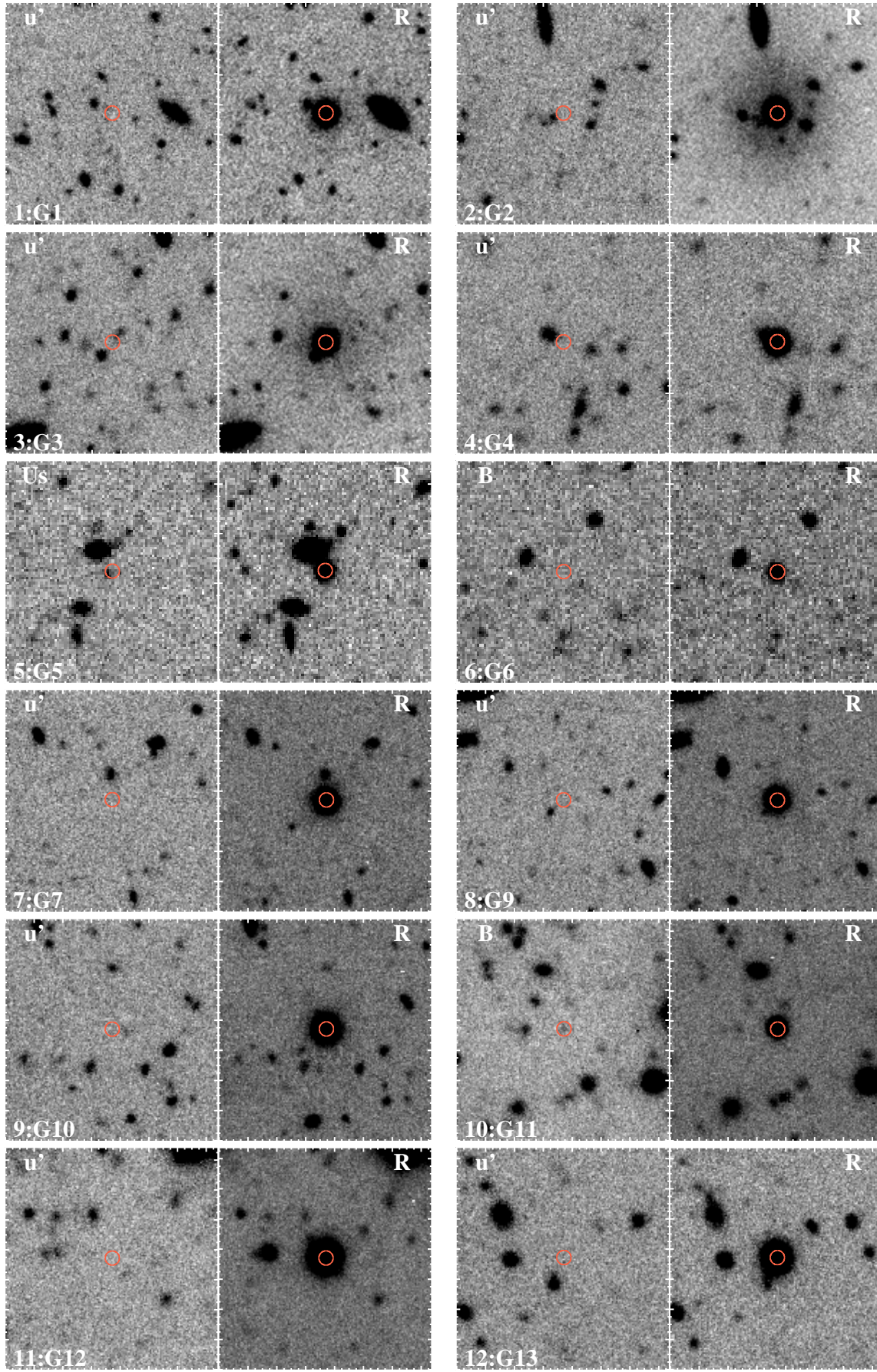


Figure 2. Gallery of the HST and ground-based imaging. For each quasar field, we show on the left imaging in the bluest available filter and on the right imaging in the R -band filter. Each panel is $30''$ on a side, with North up and East to the left. The quasar position is marked by a red circle of $1''$ in radius.

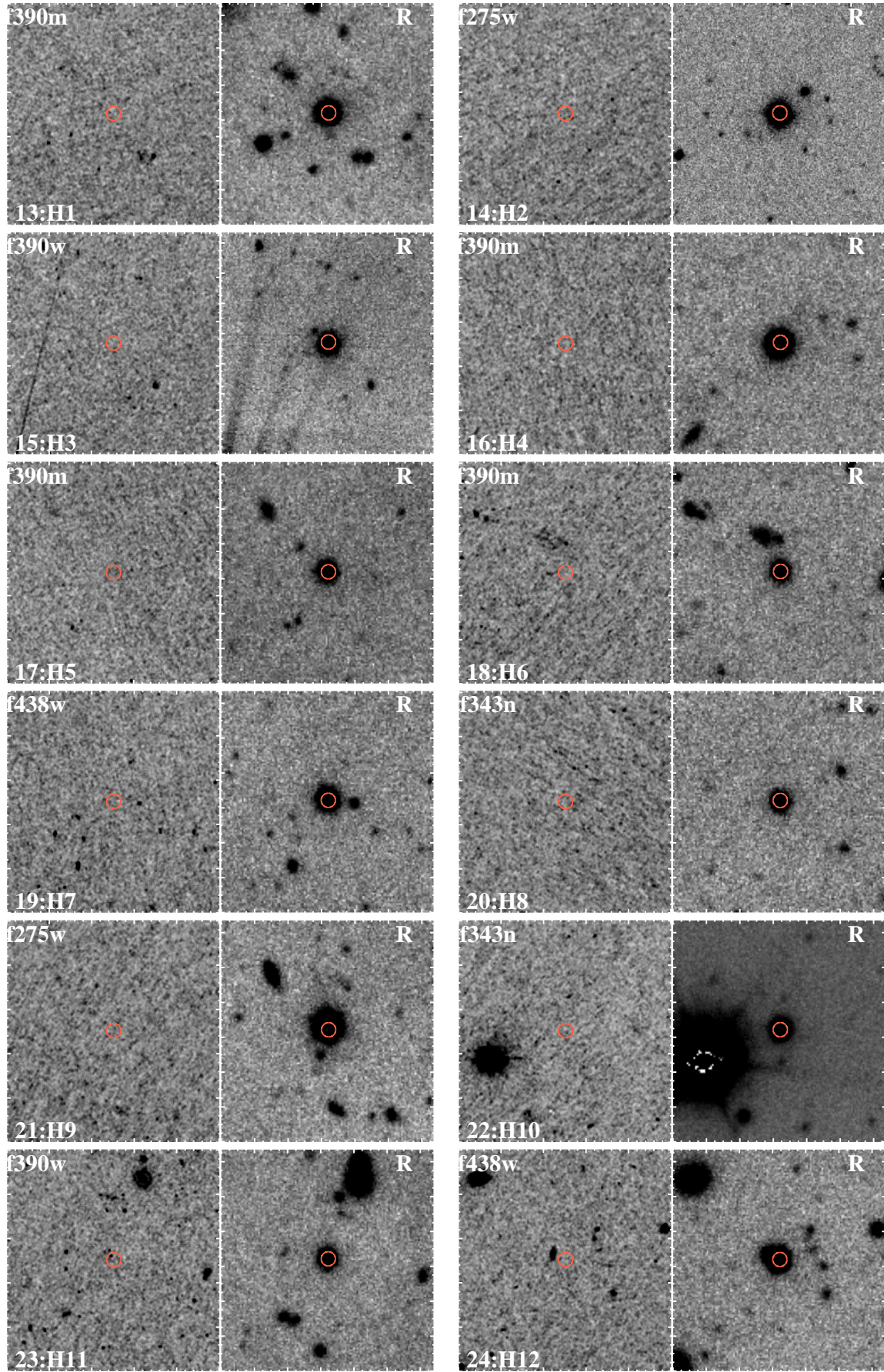


Figure 2 – continued Gallery of the HST and ground-based imaging. For each quasar field, we show on the left imaging in the bluest available filter and on the right imaging in the R -band filter. Each panel is $30''$ on a side, with North up and East to the left. The quasar position is marked by a red circle of $1''$ in radius. © XXXX RAS, MNRAS 000, 1–18

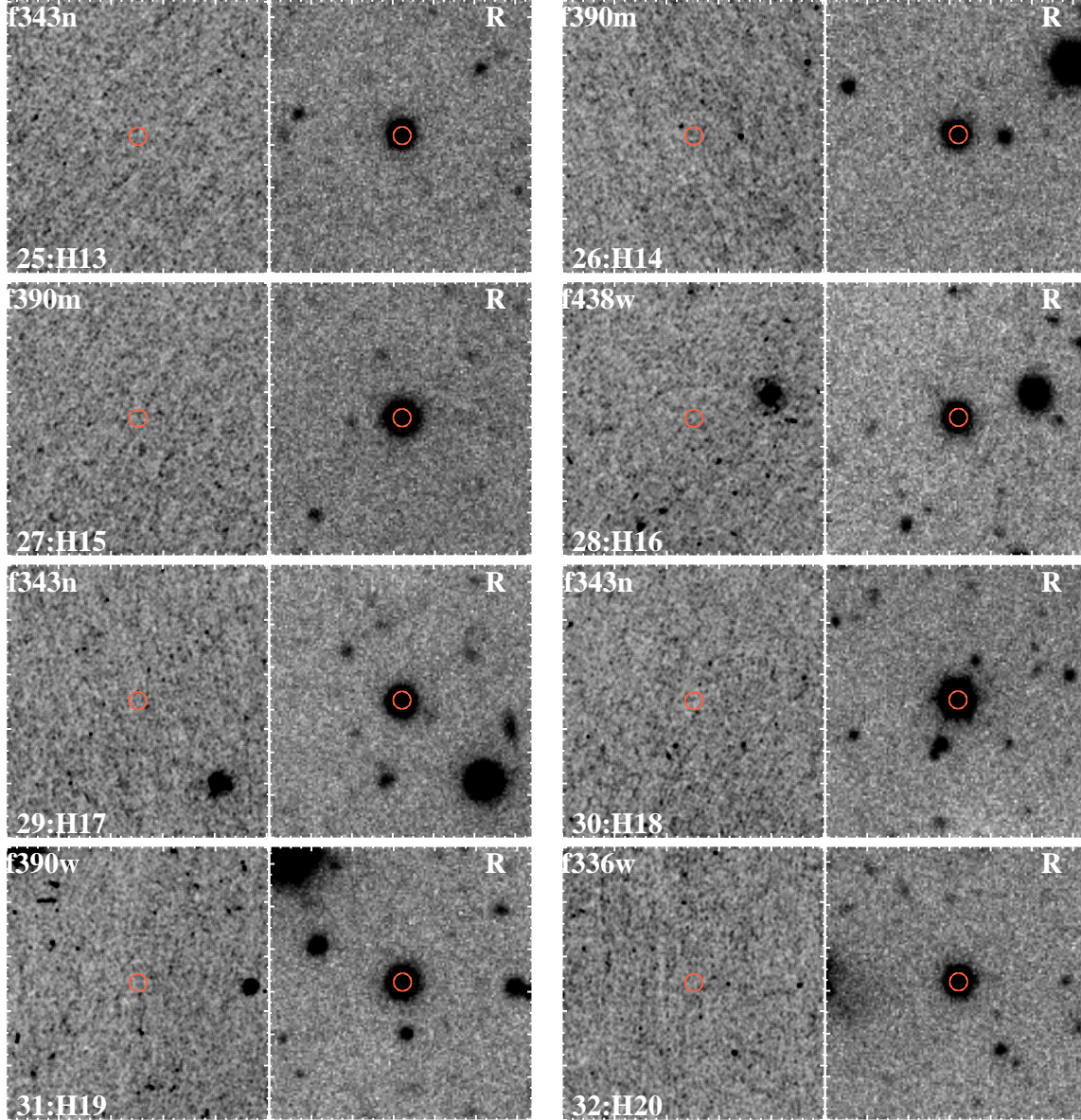


Figure 2 – continued Gallery of the HST and ground-based imaging. For each quasar field, we show on the left imaging in the bluest available filter and on the right imaging in the R -band filter. Each panel is $30''$ on a side, with North up and East to the left. The quasar position is marked by a red circle of $1''$ in radius.

3 IMAGING OBSERVATIONS

In this section we discuss new imaging observations and the data processing for both the HST and the ground-based samples.

3.1 HST Imaging

3.1.1 Data Processing

Imaging observations in the near-UV (NUV) for the HST sample were acquired during cycle 17 (PI O'Meara, PID 11595), using the UVIS channel of WFC3. For each field, observations were conducted in two orbits using the filter that maximizes the overlap between the transmission curve and the wavelength interval defined by the DLA Lyman limit and the LLS Lyman limit (see Figure 1). The dates in which observations were conducted, the filter choices,

and the effective exposure times for each quasar field are listed in Table 2.

The final images presented in this work were retrieved from the Hubble Legacy Archive (DR7) which provides enhanced data products in the form of final co-added images in units of e/s . Data have been re-projected to a regular grid of pixel size $0.04''$ and cleaned from cosmic rays. The inverse variance images that express the associated noise and the maps of the effective exposure time in each pixel are also retrieved from the archive. For photometric calibration, we utilize the zero-points published at the time of imaging retrieval, for which we assume a typical uncertainty of 2%. We further assume a point spread function (PSF) of $0.08''$ full width at half maximum (FWHM). A zoom-in of the processed images centered on the quasars is shown in Figure 2.

Table 2. Log of the imaging observations for the ground-based sample.

Field ^a	R.A. ^b (J2000)	Dec. ^b (J2000)	UT Date ^c	Filter ^d	Instr. ^e	Time ^f (s)	A.M. ^g	Pixel ^h ('')	FWHM ⁱ ('')	Depth ^j (mag)	Compl. ^m	A _X ⁿ (mag)
1:G1	21:14:43.95	-00:55:32.7	2008 Oct, 2 nd	u'	LRIS	5400	1.08	0.135	0.67	29.01	27.2/25.5	0.24
				"	LRIS	1320	1.08	0.135	0.63	28.09		0.15
				"	LRIS	1320	1.07	0.135	0.67	27.88		0.13
				"	LRIS	1515	1.07	0.135	0.79	27.37		0.10
2:G2	07:31:49.50	+28:54:48.6	2009 Jan, 28 th	u'	LRIS	5400	1.10	0.135	0.88	28.61	26.6/25.6	0.21
				"	LRIS	2140	1.10	0.135	0.89	27.43		0.14
				"	LRIS	2420	1.08	0.135	0.83	27.43		0.11
3:G3	09:56:04.43	+34:44:15.5	2009 Jan, 28 th	u'	LRIS	5400	1.16	0.135	1.00	28.88	26.8/26.0	0.05
				"	LRIS	2280	1.15	0.135	0.92	27.82		0.03
				"	LRIS	2280	1.17	0.135	0.90	27.74		0.03
4:G4	23:43:49.41	-10:47:42.0	2009 Jul, 23 rd ¹	u'	LRIS	6300	1.18	0.135	1.31	28.44	26.0/25.2	0.13
				"	LRIS	1400	1.17	0.135	0.99	27.58		0.08
				"	LRIS	1440	1.18	0.135	1.27	27.46		0.07
				"	LRIS	1540	1.17	0.135	1.15	27.22		0.05
5:G5	03:43:00.88	-06:22:29.9	2009 Sep, 20 th	U_s	LBC	3912	1.30	0.224	1.15	28.04	25.7/25.1	0.23
				"	LBC	900	1.30	0.224	1.06	27.62		0.15
				"	LBC	1200	1.29	0.224	0.98	27.71		0.12
				"	LBC	1650	1.35	0.224	0.98	27.40		0.09
6:G6	23:51:52.80	+16:00:48.9	2009 Sep, 21 st	B	LBC	1655	1.09	0.224	1.19	28.32	25.9/25.0	0.12
				"	LBC	450	1.09	0.224	0.97	27.32		0.09
				"	LBC	600	1.11	0.224	0.99	27.40		0.08
				"	LBC	750	1.13	0.224	1.02	27.08		0.06
7:G7	00:42:19.74	-10:20:09.4	2009 Dec, 17 st	u'	LRIS	5400	1.16	0.135	0.75	28.64	26.4/25.4	0.13
				"	LRIS	1400	1.16	0.135	0.83	27.64		0.08
				"	LRIS	1400	1.16	0.135	0.84	27.38		0.07
				"	LRIS	1440	1.16	0.135	0.83	27.03		0.05
8:G9	09:49:27.88	+11:15:18.2	2009 Dec, 17 st	u'	LRIS	5400	1.16	0.135	0.77	28.94	27.1/26.0	0.09
				"	LRIS	1200	1.14	0.135	0.81	27.80		0.06
				"	LRIS	1200	1.16	0.135	0.73	27.68		0.05
				"	LRIS	1440	1.13	0.135	0.75	27.38		0.04
9:G10	10:18:06.28	+31:06:27.2	2009 Dec, 17 st	u'	LRIS	3600	1.02	0.135	0.92	29.08	26.9/25.5	0.12
				"	LRIS	800	1.02	0.135	0.85	27.68		0.08
				"	LRIS	800	1.02	0.135	0.86	27.64		0.06
				"	LRIS	960	1.02	0.135	0.96	27.46		0.05
10:G11	08:51:43.72	+23:32:08.9	2009 Dec, 18 st	B	LRIS	3600	1.19	0.135	1.21	28.69	26.7/25.0	0.10
				"	LRIS	800	1.02	0.135	1.15	27.42		0.08
				"	LRIS	800	1.02	0.135	1.14	27.32		0.07
				"	LRIS	960	1.02	0.135	1.16	26.97		0.05
11:G12	09:56:05.09	+14:48:54.7	2009 Dec, 18 st	u'	LRIS	5400	1.19	0.135	1.30	28.60	26.0/25.4	0.11
				"	LRIS	1200	1.17	0.135	1.20	27.61		0.07
				"	LRIS	1200	1.19	0.135	1.09	27.53		0.06
				"	LRIS	1440	1.16	0.135	1.14	27.18		0.04
12:G13	11:51:30.48	+35:36:25.0	2009 Dec, 18 st	u'	LRIS	3600	1.21	0.135	1.21	28.61	26.4/25.1	0.08
				"	LRIS	1200	1.21	0.135	1.09	27.88		0.05
				"	LRIS	1200	1.20	0.135	1.14	27.78		0.04
				"	LRIS	1440	1.18	0.135	1.10	27.45		0.03

^a ID of the quasar field. ^b Right ascension and declination of the quasar. ^c UT date in which observations were conducted. ^d Adopted filter. ^e Instrument. ^f Total exposure time. ^g Typical airmass during observations. ^h Pixel size of the final reprojected image. ⁱ Point source full-width at half-maximum. ^j Image depth at 2σ measured in a $1''$ aperture. ^m 90% completeness limit from simulated images (left) and as empirically determined based on the recovered number counts (right). ⁿ Galactic extinction in the adopted filter. ¹ Additional observations from 2009 Sep 17th were coadded in the preparation of the final images.

3.1.2 Source extraction and noise properties

To identify galaxies in the field, we use the SExtractor software package (Bertin & Arnouts 1996), following a general procedure similar to the one employed in the CANDELS survey (Galametz et al. 2013; Guo et al. 2013), but adapted to our goals. We run SExtractor with a set of parameters that maximizes the detection of faint and small objects, similar to the “hot” mode in Guo et al. (2013).

Specifically, we convolve the images with a Gaussian filter of 5 pixels in size, and we select sources with a minimum area

of 10 pixels, using a detection threshold of 1.15, and an analysis threshold of 3.0. At the depth of our imaging, blending of unrelated sources is a rare occurrence. Conversely, low-redshift and extended sources in the UV exhibit a clumpy structure, which is typical for star-forming galaxies. To prevent detecting these clumps as individual sources, we reduce the deblending efficiency during source extraction. Given the small width of the Gaussian filter, however, the very extended sources are still fragmented in multiple clumps, a limitation which does not affect significantly our analysis of galaxies at $z \gtrsim 2$. The background is computed locally in regions of 128 pixels and annuli of 48 pixels. Inverse variance maps are used

Table 2 – continued Log of the imaging observations for the HST sample.

Field	R.A. (J2000)	Dec. (J2000)	UT Date	Filter	Instr.	Time (s)	A.M.	Pixel (‘‘)	FWHM (‘‘)	Depth (mag)	Compl.	A_X (mag)
13:H1	21:23:57.56	-00:53:50.1	2009 Dec, 4 th	<i>F390M</i>	UVIS	5130		0.040	0.08	25.97	26.4/25.2	0.14
			2013 Aug, 11 th	<i>V</i>	ESI	360	1.25	0.156	0.94	27.11		0.10
			”	<i>R</i>	ESI	360	1.27	0.156	0.93	26.99		0.08
14:H2	04:07:18.06	-44:10:14.0	2010 Feb, 13 th	<i>F275W</i>	UVIS	5361		0.040	0.08	26.60	27.2/26.3	0.07
			2013 Oct, 06 th	<i>V</i>	IMACS	600	1.10	0.111	0.54	26.67		0.03
			”	<i>R</i>	IMACS	900	1.11	0.111	0.50	26.84		0.03
15:H3	02:55:18.58	+00:48:47.6	2010 Feb, 13 th	<i>F390W</i>	UVIS	5130		0.040	0.08	27.39	27.9/27.2	0.32
			2009 Dec, 17 st	<i>u'</i>	LRIS	4500	1.07	0.135	0.65	28.36	26.5/25.8	0.34
			”	<i>V</i>	LRIS	1000	1.09	0.135	0.67	27.50		0.21
			”	<i>R</i>	LRIS	1000	1.08	0.135	0.75	27.42		0.18
16:H4	08:16:18.99	+48:23:28.4	2010 Feb, 24 th	<i>F390M</i>	UVIS	5456		0.040	0.08	25.97	26.6/26.1	0.19
			2012 Jan, 25 th	<i>V</i>	ESI	360	1.17	0.156	1.06	27.35		0.13
			”	<i>R</i>	ESI	360	1.18	0.156	1.07	26.87		0.10
17:H5	09:30:51.93	+60:23:01.1	2010 Feb, 28 th	<i>F390M</i>	UVIS	5721		0.040	0.08	25.94	26.4/25.5	0.11
			2012 Mar, 17 th	<i>V</i>	ESI	360	1.36	0.156	0.84	27.08		0.07
			”	<i>R</i>	ESI	360	1.37	0.156	0.86	26.80		0.06
18:H6	09:08:10.36	+02:38:18.7	2010 Mar, 20 th	<i>F390M</i>	UVIS	5641		0.040	0.08	26.18	26.8/26.1	0.10
			2012 Jan, 25 th	<i>V</i>	ESI	360	1.25	0.156	1.14	27.24		0.07
			”	<i>R</i>	ESI	360	1.22	0.156	0.84	26.69		0.05
19:H7	12:20:21.39	+09:21:35.7	2010 Apr, 13 th	<i>F438W</i>	UVIS	5657		0.040	0.08	26.98	27.5/26.8	0.08
			2012 Jan, 25 th	<i>V</i>	ESI	360	1.02	0.156	0.83	27.22		0.06
			”	<i>R</i>	ESI	360	1.02	0.156	0.66	26.71		0.05
20:H8	14:42:33.01	+49:52:42.6	2010 Apr, 16 th	<i>F343N</i>	UVIS	5955		0.040	0.08	26.50	27.2/26.3	0.11
			2012 Mar, 17 th	<i>V</i>	ESI	360	1.21	0.156	0.89	27.17		0.07
			”	<i>R</i>	ESI	360	1.20	0.156	0.87	27.08		0.06
21:H9	08:44:24.24	+12:45:46.7	2010 Apr, 24 th	<i>F275W</i>	UVIS	5663		0.040	0.08	26.72	27.5/26.9	0.23
			2012 Jan, 25 th	<i>V</i>	ESI	360	1.10	0.156	0.85	27.14		0.11
			”	<i>R</i>	ESI	360	1.09	0.156	0.84	26.76		0.09
22:H10	07:51:55.10	+45:16:19.6	2010 May, 4 th	<i>F343N</i>	UVIS	5955		0.040	0.08	26.40	27.1/26.6	0.19
			2012 Jan, 25 th	<i>V</i>	ESI	360	1.13	0.156	1.03	27.26		0.12
			”	<i>R</i>	ESI	360	1.14	0.156	0.91	26.72		0.09
23:H11	08:18:13.14	+07:20:54.9	2010 May, 10 th	<i>F390W</i>	UVIS	5657		0.040	0.08	27.40	28.1/26.7	0.07
			2012 Jan, 25 th	<i>V</i>	ESI	360	1.11	0.156	0.83	27.10		0.05
			”	<i>R</i>	ESI	360	1.09	0.156	0.82	26.70		0.04
24:H12	08:18:13.05	+26:31:36.9	2010 May, 13 th	<i>F438W</i>	UVIS	5687		0.040	0.08	26.82	27.4/26.6	0.11
			2012 Jan, 25 th	<i>V</i>	ESI	360	1.09	0.156	0.91	27.15		0.08
			”	<i>R</i>	ESI	360	1.11	0.156	0.98	26.68		0.06
25:H13	08:11:14.32	+39:36:33.2	2010 May, 14 th	<i>F343N</i>	UVIS	5775		0.040	0.08	26.43	27.1/26.0	0.19
			2012 Jan, 25 th	<i>V</i>	ESI	360	1.09	0.156	0.93	27.27		0.12
			”	<i>R</i>	ESI	360	1.09	0.156	0.91	26.73		0.10
26:H14	15:08:51.94	+51:56:27.7	2010 Jun, 1 st	<i>F390M</i>	UVIS	6063		0.040	0.08	26.16	26.8/26.3	0.07
			2012 Mar, 17 th	<i>V</i>	ESI	360	1.22	0.156	0.99	27.13		0.05
			”	<i>R</i>	ESI	360	1.21	0.156	0.88	27.02		0.04
27:H15	10:54:30.07	+49:19:47.1	2010 Jun, 4 th	<i>F390M</i>	UVIS	5955		0.040	0.08	26.18	26.8/26.3	0.07
			2012 Mar, 17 th	<i>V</i>	ESI	360	1.28	0.156	1.16	27.19		0.05
			”	<i>R</i>	ESI	360	1.29	0.156	0.99	27.00		0.04
28:H16	09:56:25.16	+47:34:42.5	2010 Jun, 6 th	<i>F438W</i>	UVIS	5955		0.040	0.08	26.89	27.5/27.2	0.03
			2012 Mar, 17 th	<i>V</i>	ESI	360	1.18	0.156	0.97	27.27		0.03
			”	<i>R</i>	ESI	360	1.19	0.156	0.83	27.06		0.02
29:H17	14:41:47.52	+54:15:38.1	2010 Jun, 9 th	<i>F343N</i>	UVIS	6063		0.040	0.08	26.54	27.3/26.7	0.05
			2012 Jan, 25 th	<i>V</i>	ESI	360	1.26	0.156	1.42	27.20		0.03
			”	<i>R</i>	ESI	360	1.27	0.156	1.17	26.68		0.03
30:H18	11:55:38.60	+05:30:50.5	2010 Jul, 12 th	<i>F343N</i>	UVIS	5657		0.040	0.08	26.39	27.2/26.4	0.07
			2012 Jan, 25 th	<i>V</i>	ESI	360	1.04	0.156	0.80	27.22		0.04
			”	<i>R</i>	ESI	360	1.04	0.156	0.75	26.68		0.03
31:H19	15:24:13.35	+43:05:37.4	2010 Jul, 14 th	<i>F390W</i>	UVIS	5855		0.040	0.08	27.68	28.3/27.3	0.09
			2012 Mar, 17 th	<i>V</i>	ESI	360	1.13	0.156	0.83	27.11		0.06
			”	<i>R</i>	ESI	360	1.12	0.156	0.84	27.01		0.05
32:H20	13:20:05.97	+13:10:15.3	2010 Nov, 23 rd	<i>F336W</i>	UVIS	5663		0.040	0.08	26.82	27.5/26.6	0.10
			2012 Jan, 25 th	<i>V</i>	ESI	360	1.01	0.156	0.88	27.33		0.06
			”	<i>R</i>	ESI	360	1.01	0.156	1.07	26.84		0.05

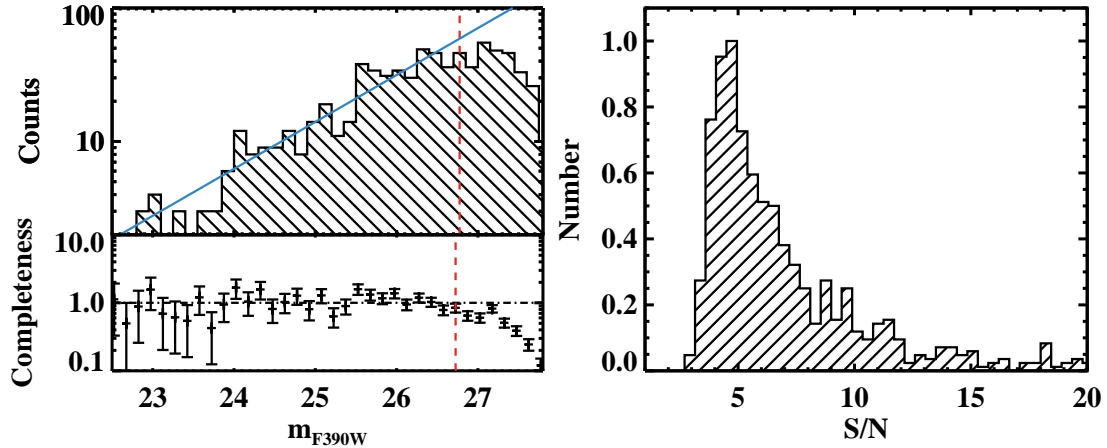


Figure 4. (Left:) Estimate of the empirical completeness for the HST field 23:H11. The dashed histogram in the top panel represents the observed number counts from the final source catalogue, while the blue solid line indicates a model fit to the observed distribution for $m < 26$ mag. The comparison between the observed and the modeled number counts is shown in the bottom panel. The magnitude at which the number counts deviate from the extrapolated model by $> 10\%$ (shown by a red dashed line) is used as empirical estimator for the 90% completeness limit. (Right:) Histogram of the S/N of the extracted sources which enter the final catalogue.

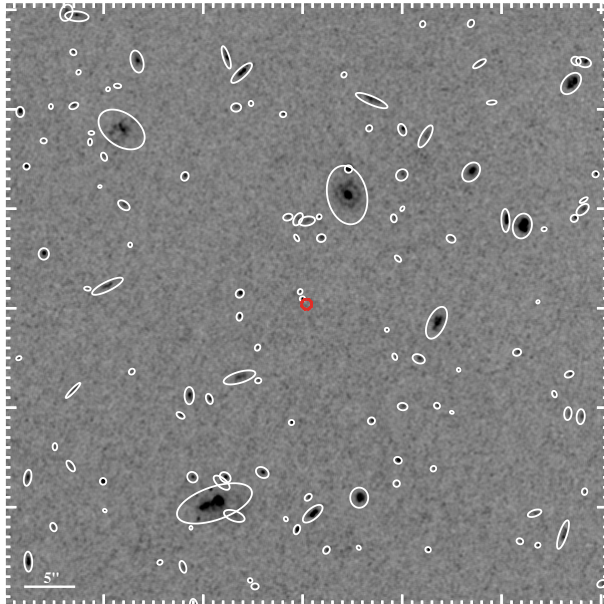


Figure 3. A region of $1' \times 1'$ around the quasar position in the field 23:H11 is shown. The red circle marks the quasar location, while the detected galaxies are identified by the Kron apertures used for photometry.

as weight maps, and we further mask bright artifacts manually, including diffraction spikes from stars and ghost images.

SEXTRACTOR produces source catalogues with magnitudes and errors. However, due to correlated noise in the reprojected images, the derived uncertainties underestimate the true errors. We therefore compute a noise model for each image, by measuring the flux standard deviation in apertures that contain n_{pix} pixels within sky regions which do not overlap with sources according to the segmentation map. To avoid signal from residual large-scale fluctuations in the background, prior to this calculation, we subtract a sky model that has been smoothed on scales of 500 pixels, much larger than the largest aperture here considered with $n_{\text{pix}} = 100$. We then parametrize the size-dependent standard deviation on the

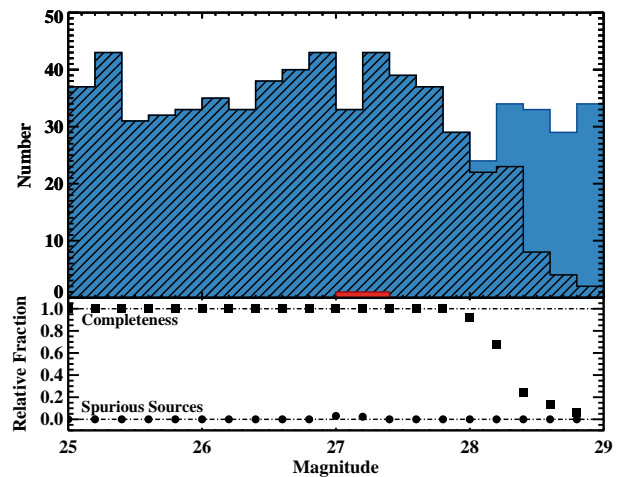


Figure 5. Top: Number of the input sources in the mock image (blue filled histogram), compared to the number of recovered sources (black dashed histogram), and spurious sources with no real counterpart (red filled histogram). Bottom: Completeness (squares) and fraction of spurious sources (circles) as a function of magnitude for the final mock catalogue.

flux with the functional form $\sigma(n_{\text{pix}}) = \sigma_1 \alpha n_{\text{pix}}^{\beta}$, where σ_1 is the flux standard deviation per pixel across the entire image, and α and β are the best-fit parameters (cf. Gawiser et al. 2006). For each image, at fixed n_{pix} , $\sigma(n_{\text{pix}})$ is very well approximated by a Gaussian, and typical parameters are $\sigma_1 \sim 0.001$, $\alpha \sim 1$, and $\beta \sim 0.6$, which imply a modest but non-zero correlation in the noise. Using the measured noise properties of individual images, we compute limiting magnitudes at the 2σ confidence level (C.L.) within a circular aperture of $1''$ in diameter, as listed in Table 2. These values can be used to quantify the depth of our images.

3.1.3 Galaxy Catalogues and Completeness

Having characterized the noise, we update the error on the fluxes computed within Kron apertures, and we include in the final cata-

logues only sources that have been detected with a $S/N \geq 3$. While seemingly low, the inclusion of correlated noise translates this limit into an effectively higher S/N cut, once compared to the values returned by SExtractor. Furthermore, the extraction parameters are chosen to minimize the inclusion of spurious sources (see below), and the resulting S/N distribution peaks at $\sim 4 - 5$ (Figure 4). In the final catalogues, we further attempt to minimize the problem of excessive deblending of extended objects by removing sources that have more than 90% of their area enclosed in another aperture. The fluxes of the larger apertures are also recomputed to account for the pixels that SExtractor originally assigned to a different source. Figure 3 shows an example of the sources included in the final catalogues for one of our quasar fields.

We assess the completeness and purity of these catalogues by means of simulated images, which we generate for each HST pointing. First, we produce a noise model by filtering high frequencies from an otherwise Gaussian noise background so to introduce a small-scale correlation with $\beta \sim 0.6$. The final noise map is then normalized to the measured σ_1 in each HST image. A consistency check reveals that the noise properties of the mock images are in excellent agreement with the measured $\sigma(n_{\text{pix}})$. Next, we insert in these images 700 point sources uniformly drawn from the magnitude interval $m = 25 - 29$ mag.

After running the same procedures used to generate the final catalogues for the science images, we compare the input lists to the recovered mock catalogues in bins of 0.1 mag, and we determine the magnitude at which the completeness falls below 90% as listed in Table 2. We also search for spurious detections, defined as extracted sources with no input counterparts within a $0.4''$ search radius. This exercise reveals that the purity of the final catalogues is $> 90\%$, with $\geq 95\%$ as typical value. And while our mock images are idealized cases (with Gaussian point sources and theoretical noise models), this test lets us conclude that the adopted extraction parameters ensure a good compromise between depth and completeness. Using these mocks, we also confirm that our photometry is free from systematic errors unaccounted for in the magnitude uncertainties, given that the input fluxes are recovered to within 2σ . The results of this test for one of our HST fields are shown in Figure 5.

We also offer a more empirical determination of the completeness limit, which also captures the presence of resolved (lower surface brightness) objects. These empirical limits are computed by modeling the number of detected sources S in bins of 0.15 mag with a function $\log S \propto m^\chi$, where χ is a free parameter chosen to reproduce the linear portion of the observed number counts ($m < 26.5$ in Figure 4). The magnitudes at which the number of extracted sources fall below 90% of the extrapolated number counts are listed in Table 2. These empirical limits are clearly sensitive to the magnitude interval adopted to constrain χ , especially because of the variance due to the small field of view of each HST image. For this reason, the quoted numbers are useful to gauge the location at which the number counts reach a maximum, but bear non-negligible uncertainties (~ 0.2 mag).

As a final step in the production of photometric catalogues, we correct all the fluxes to account for Galactic extinction, using the Fitzpatrick (1999) extinction law and the Schlegel et al. (1998) dust map, which we re-calibrate as described in Schlafly & Finkbeiner (2011). Extinctions in each filter A_X are computed by convolving the wavelength-dependent extinction curve at each quasar position with the total instrument throughput (see Section 3.2.3) and a source spectral energy distribution (SED) of the form $f_\lambda \propto \lambda^{-2}$, as appropriate for high-redshift star-forming galaxies (cf. Appendix B

in Schlegel et al. 1998). Values are listed in Table 2. In the following, we do not include the uncertainty on the Galactic extinction correction (at the level of 4 – 5%), which corresponds to a systematic error in each field.

3.2 Ground-based Imaging

3.2.1 Observations

Imaging observations for the ground-based sample were obtained in most part using the dual-arm Low Resolution Imaging Spectrometer (LRIS; Oke et al. 1995) at the Keck I telescope. In the blue camera, we consistently adopted either the u' or B filters, which were chosen to match the DLA redshifts, while we used the V , R , and I filters in the red camera. On the blue arm, the two $2k \times 4k$ Marconi (E2V) CCDs have been available throughout the entire duration of our imaging program, but the Tektronix/SITe $2k \times 2k$ CCD on the red arm of LRIS was replaced with two $2k \times 4k$ LBNL CCD detectors in 2009 (Rockosi et al. 2010), after the observations of the first three fields (1:G1, 2:G2, and 3:G3). Additionally, two quasar fields (5:G5 and 6:G6) were observed with the Large Binocular Cameras (LBC; Pedichini et al. 2003) at the prime focus of the Large Binocular Telescope (LBT). Finally, in support of the HST imaging observations described in the previous section, we acquired from the ground imaging in the V and R filters, using either LRIS, or the Echelle Spectrograph and Imager (ESI; Sheinis et al. 2002), or the Inamori-Magellan Areal Camera and Spectrograph (IMACS; Dressler et al. 2006). A log book of the imaging observations is provided in Table 2. Observations were conducted under a variety of weather conditions, mostly in clear and/or photometric skies, but sometimes in the presence of cirrus and patchy clouds.

3.2.2 Data Reduction

All ground based images have been processed following standard reduction techniques, using a combination of in-house codes and the SCAMP, SWARP, and SExtractor software packages (Bertin & Arnouts 1996; Bertin et al. 2002; Bertin 2006). First, a bias level is subtracted from each frame according to the counts recorded in the overscan region. Next, we correct the pixel response across the image using twilight flats, or dome flats, or a combination of both. After applying the gain, we construct an inverse variance image which we also use to mask hot pixels and bad columns. Cosmic rays are identified and masked using the algorithm presented in van Dokkum (2001). Given the thickness of the upgraded CCDs on the red side of LRIS, a much higher incidence of cosmic rays is present in these images. Further, because of the higher number of grazing events, trails of several arcseconds up to one arcminute are common in these images. In this case, we reject cosmic rays more aggressively by comparing pixels across multiple exposures of the same field to identify rare fluctuations in the number counts that are caused by transient events.

Next, we fit an astrometric solution to each set of exposures of individual quasar fields using the SCAMP software. In all but one case (the southern field 14:H2), we use the SDSS-DR7 source catalogue as our reference coordinate system. For the 14:H2 field instead, we use the USNO star catalogue. Comparing all detected sources with a corresponding match in the reference catalogue, we find negligible systematic offsets for both the right ascension ($\alpha_{\text{sys}} = 0.006''$) and the declination ($\delta_{\text{sys}} = 0.002''$). Given that the native pixel sizes range from $0.111''$ for IMACS to $0.224''$ for

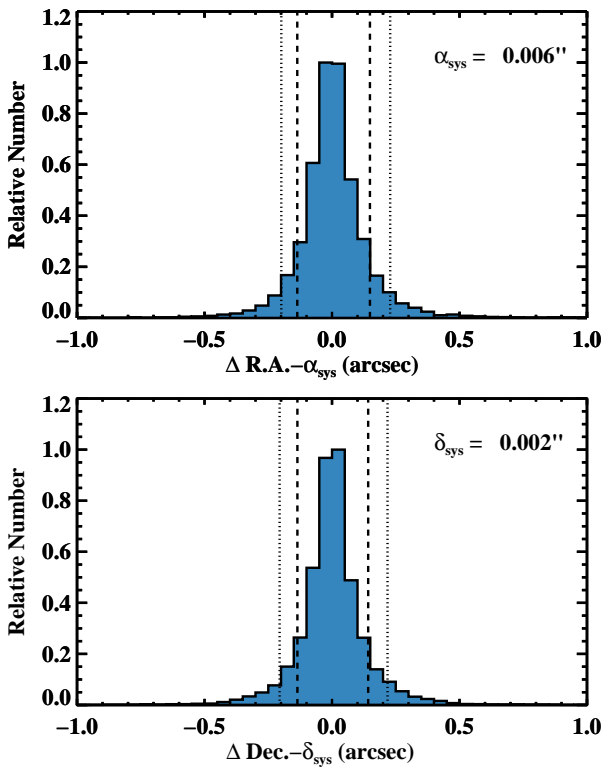


Figure 6. Quality of the astrometric solutions for all imaged quasar fields. Each panel shows the histogram of residual right ascensions (top) and declinations (bottom) for all the detected sources with a match in SDSS-DR9 after a small systematic correction has been applied as indicated inside each panel. The 5%, 10%, 90%, and 95% of the distributions are also shown, indicating that we achieve a precision in the astrometry across the imaged fields of $\lesssim 1$ pixel and an accuracy of $\ll 1$ pixel.

LBC, our solutions thus achieve an accuracy of $\ll 1$ pixel. Figure 6 shows the residuals of these astrometric solutions relative to all the detected sources once the small systematic offsets have been subtracted. The 5%, 10%, 90%, and 95% of the distributions are also shown, indicating that we achieve a precision in the astrometry across the imaged fields of $\lesssim 1$ pixel.

Finally, using the SWARP software, we reproject the background-subtracted images in e/s to a common grid of fixed pixel size. During this step, we employ a Lanczos resampling technique and, with the exception of the old CCD on the red side of LRIS, we preserve the native pixel size of each instrument ($0.156''$ for ESI, $0.224''$ for LBT, $0.135''$ for LRIS, and $0.111''$ for IMACS). As a last step, the reprojected images in the same filter are optimally combined, weighting by their inverse variance. A gallery of the processed images for each quasar field in the adopted blue filter and in the R -band is presented in Figure 2.

To assess the quality of the processed data, we generate a model for the PSF by combining multiple sharp stars that are relatively isolated, i.e. without bright sources within a $2''$ radius. We then fit a Gaussian to the resultant light profiles in each filter. The inferred FWHMs are listed in Table 2.

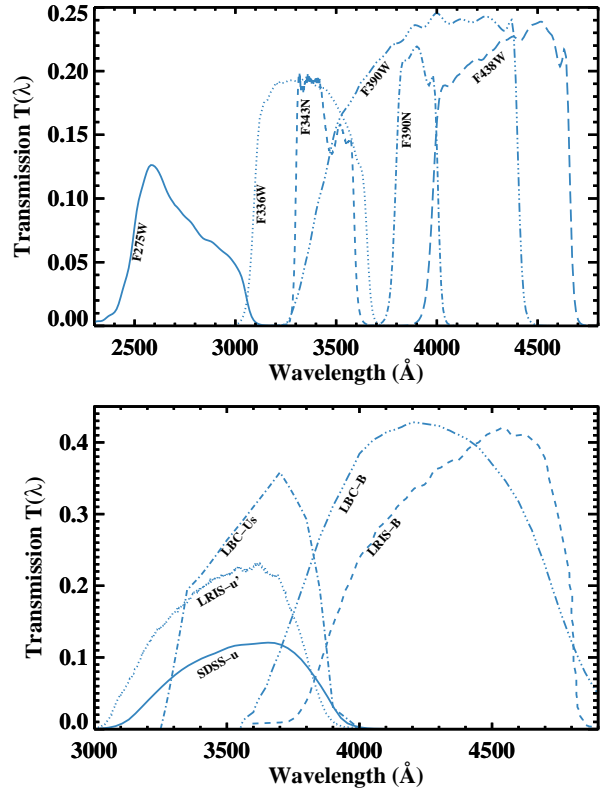


Figure 7. Comparison of the effective filter transmission curves that have been used for this imaging survey blueward of $\sim 4500\text{\AA}$. The effects of the wavelength dependent quantum efficiency and, for ground-based instruments, of the atmospheric extinction per unit airmass have been included. The SDSS u filter is also shown for comparison.

3.2.3 Photometric Calibrations

During the ground-based part of this imaging program, we made use of multiple instruments and filters sets: U s and B for the blue channel of LBC; V , R , and I for the red channel of LBC; V and R for ESI; u' and B for the blue arm of LRIS; V , R , and I for the red arm of LRIS before and after the CCD upgrade²; R and V for IMACS at Magellan. For each filter, we compute the effective transmission curve $T(\lambda)$, including the measured detector response $S(\lambda)$ and the best estimate of atmospheric extinction $\exp(-\alpha(\lambda)X)$ at airmass $X = 1$ for each site. LRIS filter transmission curves are further corrected for the D460 dichroic, in use during the observations. These filter transmission curves are shown in Figures 7 and 8, together with the adopted HST/WFC3 filters and, for comparison, the SDSS u , g , r , i filters.

To homogenize photometry across many different filters, instruments, and observing nights, we use stars within the SDSS footprint as calibrators, after applying color transformations and conversions to Pogson magnitudes in the AB system (Fukugita et al. 1996; Lupton et al. 1999; Smith et al. 2002). To this purpose, we first need to compute transformations from the SDSS filter set to the filters available at each instrument. Both empirical and theoretical transformations from the Gunn to Johnson filters exist in the literature (Kent 1985; Windhorst et al. 1991; Fukugita et al. 1996;

² Filter transmission curves for the old LRIS detector are marked as V' , R' , and I'

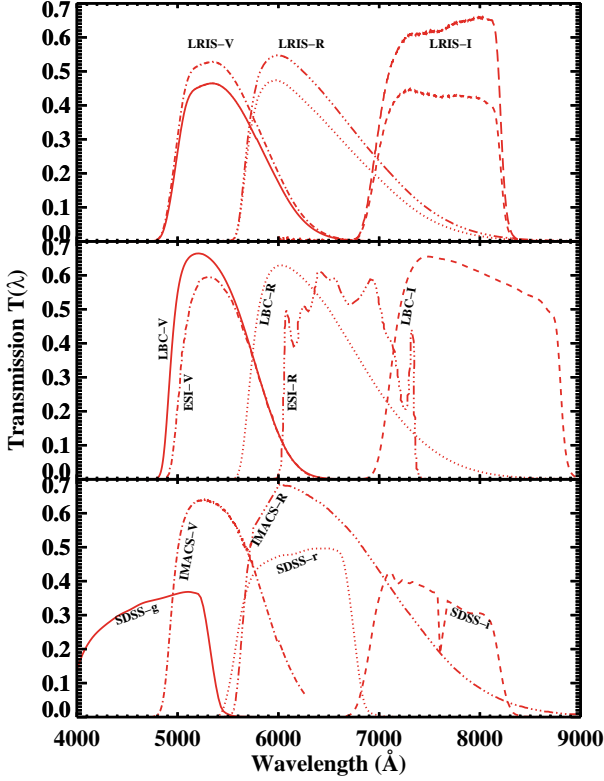


Figure 8. Comparison of the effective filter transmission curves that have been used for this imaging survey redward of $\sim 4500\text{\AA}$. The effects of the wavelength dependent quantum efficiency and of the atmospheric extinction per unit airmass have been included. The SDSS g , r , and i filters are also plotted for comparison. In the top panel, we display two transmission curves for each LRIS filter, one for the old Tektronix/SITe CCD and the other for the new higher-throughput LBNL CCD.

Smith et al. 2002, e.g.). However, because our filter set includes non-standard filters (e.g. U_{lbc} and R_{esi}), we recompute these transformations following common procedures (e.g. Smith et al. 2002). In this calculation, we employ stellar SEDs from the ‘‘CALSPEC’’ library of spectrophotometric stars available through the Hubble Space Telescope Calibration Database System, which also includes spectrophotometric stars from Oke (1990). Although this library is of high quality, it does not encompass all spectral types, which we recover by adding the stellar atlas by Gunn & Stryker (1983).

We test our procedures by convolving the BD+17 4708 spectrum with the SDSS filter transmission curves shown in Figure 7 and 8, recovering the magnitudes $u_{\text{sdss}} = 10.54$, $g_{\text{sdss}} = 9.65$, $r_{\text{sdss}} = 9.35$, $i_{\text{sdss}} = 9.25$. These values are in excellent agreement with those reported by Fukugita et al. (1996) and Smith et al. (2002). Further, for the V_{iris} filter which is similar to a standard Johnson V filter, we recover the transformation $V_{\text{iris}} = g_{\text{sdss}} - 0.025 - 0.60(g_{\text{sdss}} - r_{\text{sdss}})$, again in good agreement with Fukugita et al. (1996) and Smith et al. (2002). Coefficients for filter transformations in the form $Y_1 = Y_2 + a_1 + a_2(Y_3 - Y_4)$ are listed in Table 3, together with the color intervals within which these transformations hold. Typical uncertainties on the resulting magnitudes are $\sim 0.02 - 0.03$ (Fukugita et al. 1996).

Once the SDSS photometry has been transferred to the new system defined by the adopted filter set, we compute zero-points

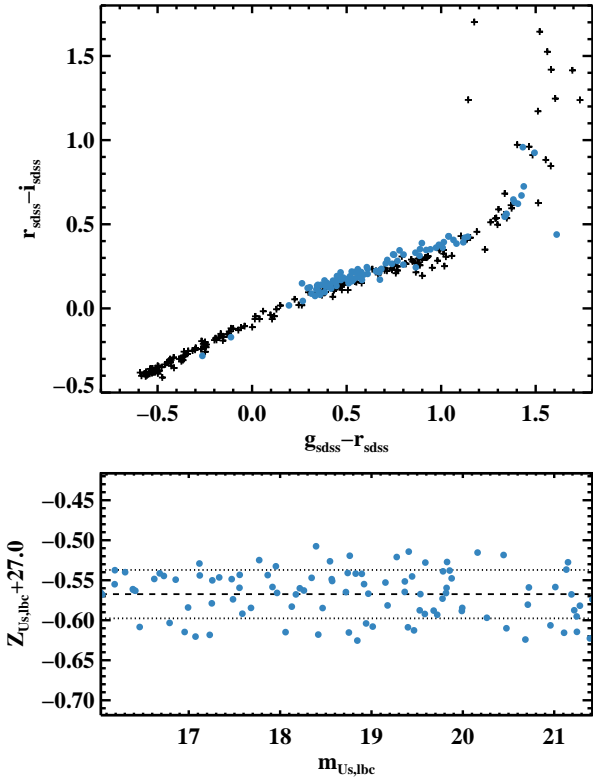


Figure 9. Results of the photometric calibration for the 5-G5 field imaged with the U_s filter at LBC. In the top panel, the SDSS $g - r$ vs. $r - i$ colors are shown for the stellar templates (black crosses) and calibration stars (blue circles). The bottom panel shows the zero point derived for each calibrator (blue circles), together with the mean (dashed line) and the associated standard deviation (dotted line).

Table 3. Coefficients for the filter transformations used for photometric calibrations. Symbols are defined in the text.

Y_1	Y_2	$(Y_3 - Y_4)$	a_1	a_2	Interval
u'_{iris}	u_{sdss}	$u_{\text{sdss}} - g_{\text{sdss}}$	+0.007	+0.08	(-0.6, +0.8)
			-0.008	+0.04	(+1.3, +3.8)
U_{lbc}	u_{sdss}	$u_{\text{sdss}} - g_{\text{sdss}}$	+0.007	-0.06	(-0.6, +1.3)
			-0.014	-0.03	(+1.3, +3.8)
B_{iris}	g_{sdss}	$g_{\text{sdss}} - r_{\text{sdss}}$	+0.052	+0.35	(-0.4, +1.4)
B_{lbc}	g_{sdss}	$g_{\text{sdss}} - r_{\text{sdss}}$	+0.116	+0.50	(-0.4, +1.4)
V_{iris}	g_{sdss}	$g_{\text{sdss}} - r_{\text{sdss}}$	-0.025	-0.60	(-0.4, +1.9)
V'_{iris}	g_{sdss}	$g_{\text{sdss}} - r_{\text{sdss}}$	-0.025	-0.60	(-0.4, +1.9)
V_{lbc}	g_{sdss}	$g_{\text{sdss}} - r_{\text{sdss}}$	-0.026	-0.54	(-0.4, +1.9)
V_{esi}	g_{sdss}	$g_{\text{sdss}} - r_{\text{sdss}}$	-0.025	-0.58	(-0.4, +1.9)
V_{imacs}	g_{sdss}	$g_{\text{sdss}} - r_{\text{sdss}}$	-0.026	-0.57	(-0.4, +1.9)
R_{iris}	r_{sdss}	$g_{\text{sdss}} - r_{\text{sdss}}$	+0.014	-0.09	(-0.4, +1.3)
R'_{iris}	r_{sdss}	$g_{\text{sdss}} - r_{\text{sdss}}$	+0.012	-0.08	(-0.4, +1.3)
R_{lbc}	r_{sdss}	$g_{\text{sdss}} - r_{\text{sdss}}$	+0.015	-0.10	(-0.4, +1.3)
R_{esi}	r_{sdss}	$g_{\text{sdss}} - r_{\text{sdss}}$	+0.035	-0.20	(-0.4, +1.3)
R_{imacs}	r_{sdss}	$g_{\text{sdss}} - r_{\text{sdss}}$	+0.023	-0.14	(-0.4, +1.3)
I_{iris}	i_{sdss}	$r_{\text{sdss}} - i_{\text{sdss}}$	+0.004	-0.07	(-0.4, +2.8)
I'_{iris}	i_{sdss}	$r_{\text{sdss}} - i_{\text{sdss}}$	+0.003	-0.05	(-0.4, +2.8)
I_{lbc}	i_{sdss}	$r_{\text{sdss}} - i_{\text{sdss}}$	+0.011	-0.22	(-0.4, +2.8)

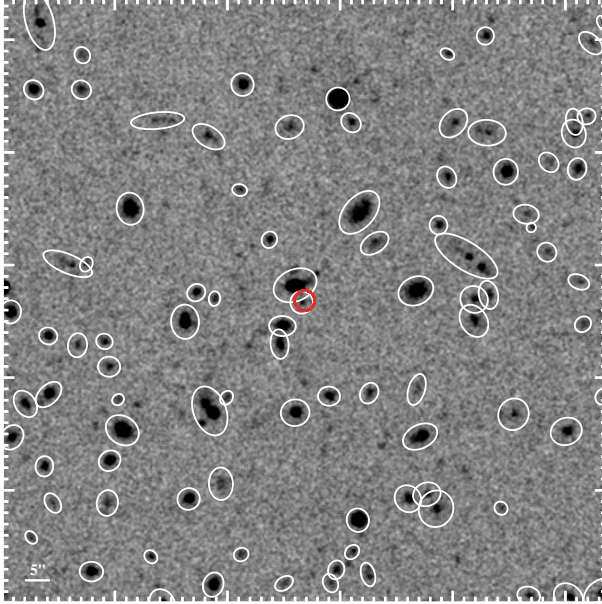


Figure 10. A region of $1' \times 1'$, imaged in the U_s -band, is shown around the quasar position in the field 5:G5. The red circle marks the quasar location, while the detected galaxies are identified by the Kron apertures used for photometry.

Z_Y by comparing the observed instrumental magnitudes Y_{inst} to the intrinsic extra-atmospheric magnitudes Y_0 , allowing for an additional offset due to atmospheric extinction k_Y as a function of airmass X : $Y_{\text{inst}} = Y_0 + Z_Y + k_Y X$. Since we do not aim to a precision of better than 0.02 mag, we neglect second-order color terms (cf. Fukugita et al. 1996). Lacking observations across a wide range of airmasses in each filter, we avoid substantial degeneracy between Z_Y and k_Y by fixing the extinction coefficients to the following values: $k_{U_s} = 0.47$, $k_B = 0.22$, $k_V = 0.16$, $k_R = 0.13$, $k_I = 0.04$ for LBC as reported on the instrument manual³; $k_{u'} = 0.41$, $k_B = 0.19$, $k_V = 0.12$, $k_R = 0.11$, $k_I = 0.07$ for LRIS (Cooke et al. 2005), $k_V = 0.12$, $k_R = 0.09$ for ESI as inferred by scaling the LRIS coefficients to the ESI effective wavelengths; and $k_V = 0.15$, $k_R = 0.11$ for IMACS (Winn et al. 2000; Krisciunas et al. 2013).

For all the fields imaged with LRIS and LBC, we compute zero-points in each image (e.g. Figure 9). Conversely, only a handful of calibrators are found within the small field of view imaged by ESI, preventing us from computing individual zero-point reliably. However, this imaging has been acquired in three clear nights during which the SkyProbe at CFHT recorded an attenuation of $\lesssim 0.05$ mag. We therefore combine calibrators from each field and fit for a single zero-point in the R_{esi} and V_{esi} filters. Uncertainties on the zero-points are computed combining the standard errors on the mean Z_Y with an error of 0.05 mag, which accounts for residuals in the filter transformations and errors in the aperture photometry for the calibrator stars.

For the southern field 14:H2, instead, zero-points are computed with photometric standard stars in the Landolt (1992) SA95 field, which we observed during the same night in which science data were taken, under photometric conditions.

³ http://abell.as.arizona.edu/~lbtsclnstruments/LBC/lbc_description.html

3.2.4 Source Extraction, Noise Properties and Completeness

For the ground-based imaging, we generate source catalogues and we characterize the image noise and completeness following similar procedures to those described in the previous section for the HST imaging. First, we generate source catalogues by running SExtractor after convolving images with a Gaussian filter of $\sim 4 - 6$ pixels in size, and by selecting sources with a minimum area of $\sim 20 - 30$ pixels, using a detection threshold of $\sim 0.6 - 0.8$, and an analysis threshold of ~ 3.0 (e.g. Figure 10). These parameters are adjusted for specific combinations of filters and instruments for optimization. The background is computed locally in regions of 64 pixels and annuli of 28 pixels. Inverse variance maps are again used as weight maps, through which we also mask bright artifacts, such as diffraction spikes from bright stars and, occasionally, poorly-masked cosmic rays. Differently from the HST imaging, we enable deblending of overlapping sources.

Following the above procedures, we model the noise in each image as $\sigma(n_{\text{pix}}) = \sigma_1 \alpha n_{\text{pix}}^{\beta}$. We find a range of coefficient across different instruments and filters, in the interval $\beta \sim 0.55 - 0.70$. The noise estimates are used to measure limiting magnitudes at the 2σ C.L. within a circular aperture of $1''$ in diameter (listed in Table 2), and to recompute the errors on the fluxes within Kron apertures. For the catalogues in the blue filters (U, B), which are the most relevant for our following analysis, we also compute completeness limits (e.g. Figure 11) with the same procedures used for the HST imaging (i.e. both from measured number counts and from mocks with artificial point sources matched to the seeing). Magnitudes at which completeness falls below 90% are listed in Table 2. With mock images we also test the quality of the photometry, concluding that input values are recovered for all sources within 2σ errors. The number of spurious detections is found to be $\lesssim 5 - 10\%$ above and at the completeness limits, and increasing between 10 – 20% at the faintest magnitudes, where only a handful of sources are typically detected. Finally, we correct all fluxes to account for Galactic extinction as described in Section 3.1.3.

4 SPECTROSCOPIC OBSERVATIONS

To characterize the absorption properties of both the DLAs and the higher redshift LLSS, we collect and analyze spectroscopic data for the targeted quasars in each field, as detailed in Table 4. For 21 quasars, we acquired new observations using ESI in echelle mode or, for two sightlines, the Magellan Echellette Spectrograph (MagE; Marshall et al. 2008). For the remaining 11 quasars, we rely on spectra published in the literature (Jorgenson et al. 2013; Prochaska et al. 2003b; Wolfe et al. 2008) or on SDSS spectroscopy, and, for 32:H20, on archival X-shooter (Vernet et al. 2011) data from programme ID 087.A-0022 (PI R. Cooke).

4.1 New Observations and Data Reduction

New spectroscopic observations for 20 quasars have been obtained with ESI under good to moderate weather and seeing conditions. ESI spectra were acquired with two different choices of slit width, $0.5''$ or $0.75''$, matched to the seeing conditions. The corresponding velocity resolution of ESI is $\sim 37 \text{ km s}^{-1}$ for the $0.5''$ slit and $\sim 56 \text{ km s}^{-1}$ for the $0.75''$ slit. Observations for two additional quasars were instead obtained with MagE using a $0.7''$ slit, under good weather conditions. In this configuration, MagE yields spectra at a resolution of $\sim 70 \text{ km s}^{-1}$. A log book of the spectroscopic

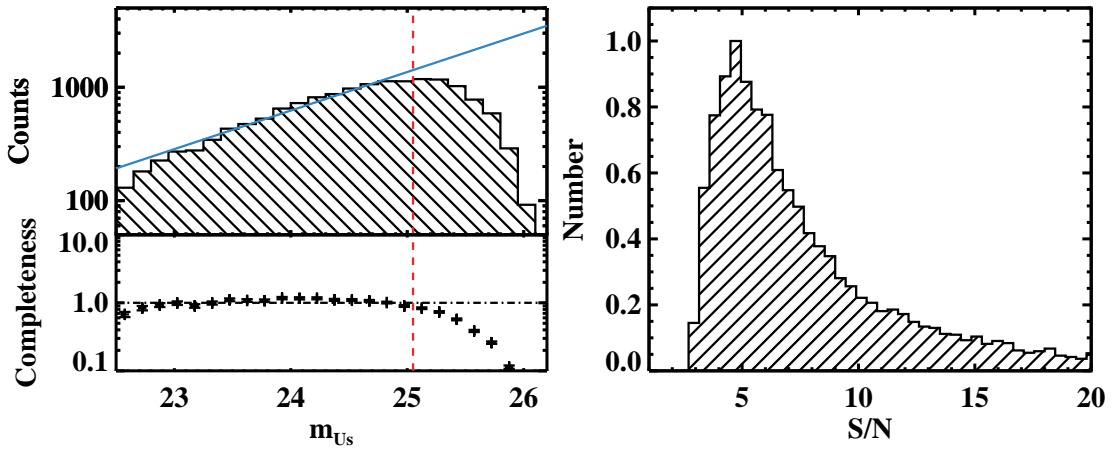


Figure 11. (Left:) Estimate of the empirical completeness for the field 5:G5 imaged in the U_s -band with LBC. The dashed histogram in the top panel represents the observed number counts from the final source catalogue, while the blue solid line indicates a model fit to the observed distribution for $m < 25$ mag. The comparison between the observed and the modeled number counts is shown in the bottom panel. The magnitude at which the number counts deviate from the extrapolated model by $> 10\%$ (shown by a red dashed line) is used as empirical estimator for the 90% completeness limit. (Right:) Histogram of the S/N of the extracted sources which enter the final catalogue.

Table 4. Log book of the quasar spectroscopic observations.

Field ^a	UT Date ^b	Instr. ^c	Slit ^d ('')	Exp. Time ^e (s)
1:G1	2010 Jan, 5 th	ESI	0.5	1800
2:G2	2010 Jan, 5 th	ESI	0.5	1800
3:G3	2010 Jan, 5 th	ESI	0.5	2400
4:G4	2010 Jan, 5 th	ESI	0.5	3600
5:G5	2012 Jan, 25 th	ESI	0.75	3600
6:G6	2010 Jan, 5 th	ESI	0.5	3600
7:G7	2010 Jan, 5 th	ESI	0.5	1800
8:G9	2012 Jan, 25 th	ESI	0.75	2400
9:G10	2010 Jan, 5 th	ESI	0.5	1800
10:G11	2010 Jan, 5 th	ESI	0.5	3600
11:G12	2010 Jan, 5 th	ESI	0.5	1800
12:G13	2010 Jan, 5 th	ESI	0.5	2400
13:H1	2010 Jan, 5 th	ESI	0.5	1800
14:H2	2009 Dec, 22 th	MagE	0.7	1800
15:H3	2010 Jan, 5 th	ESI	0.5	2400
16:H4	2010 Jan, 5 th	ESI	0.5	2400
17:H5	-	SDSS	-	-
18:H6	2013 Mar, 2 nd	MagE	0.7	3600
19:H7	-	[1]	-	-
20:H8	-	SDSS	-	-
21:H9	2013 Jan, 4 th	ESI	0.75	960
22:H10	2010 Jan, 5 th	ESI	0.5	2400
23:H11	2012 Jan, 25 th	ESI	0.75	3600
24:H12	2013 Jan, 4 th	ESI	0.75	3600
25:H13	2012 Jan, 25 th	ESI	0.75	3600
26:H14	-	SDSS	-	-
27:H15	-	SDSS	-	-
28:H16	-	[2]	-	-
29:H17	-	SDSS	-	-
30:H18	-	[3]	-	-
31:H19	-	SDSS	-	-
32:H20	-	[4]	-	-

^a ID of the quasar field. ^b UT date during which observations were conducted. ^c Instrument/survey, or reference to the source of archival data. ^d Slit width. ^e Exposure time. [1] MagE data from Jorgenson et al. (2013); [2] ESI data from Prochaska et al. (2003b); [3] ESI data from Wolfe et al. (2008); [4] X-shooter data from Cooke et al. (private communication).

observations with the corresponding exposure times is provided in Table 4.

ESI data were reduced using the ESIREDUX software package⁴. The pipeline processes the 2D frames by performing bias subtraction and flat fielding. Next, it creates a wavelength solution using arc lines, and it extracts and coadds the spectra in each order, producing wavelength- and flux-calibrated 1D spectra, together with associated errors. Flux calibration is achieved with repeated observations of spectrophotometric standard stars that were observed throughout the night. MagE spectra are processed following similar procedures, but using the MASE pipeline (Bochanski et al. 2009).

4.2 Redshifts and H I Column Densities

In each spectrum, we search for metal lines that are associated with the targeted DLAs. These transitions, and preferentially those at low ionization states (e.g. O I, Si II, C II, or Al II), are used to pinpoint the redshifts of the absorbers. Similarly, we use both metal lines and high-order transitions in the Lyman series to measure the redshift of the LLSs that act as blocking filters. Typical errors on the redshifts are $\delta_z \sim 0.0001$ for ESI and MagE spectra, and $\delta_z \sim 0.0005$ for SDSS spectra. Values are listed in Table 1 and shown in the bottom panel of Figure 12. The majority of the targeted DLAs lie in the redshift window $z \sim 2.5 - 3.0$, with a handful of outliers at higher and lower redshifts. The majority of the high-redshift blocking systems lie instead around redshifts $z \sim 3.5$, by construction of our experiment.

For the DLAs, we also measure the H I column densities by fitting Voigt profiles to the Ly α lines in the flux-calibrated spectra, as shown in Figure 13. The amplitude of the errors is set according to the results of the simulations described in Rafelski et al. (2014). In this previous work, after inserting $z \gtrsim 4$ DLAs into actual sightlines and into mock spectra at the resolution of ESI, we recovered column densities with mean offsets of $0.02 - 0.06$ dex compared to the input values, and with standard deviations of

⁴ <https://www2.keck.hawaii.edu/realpublic/realpublic/inst/esi/ESIRedux>

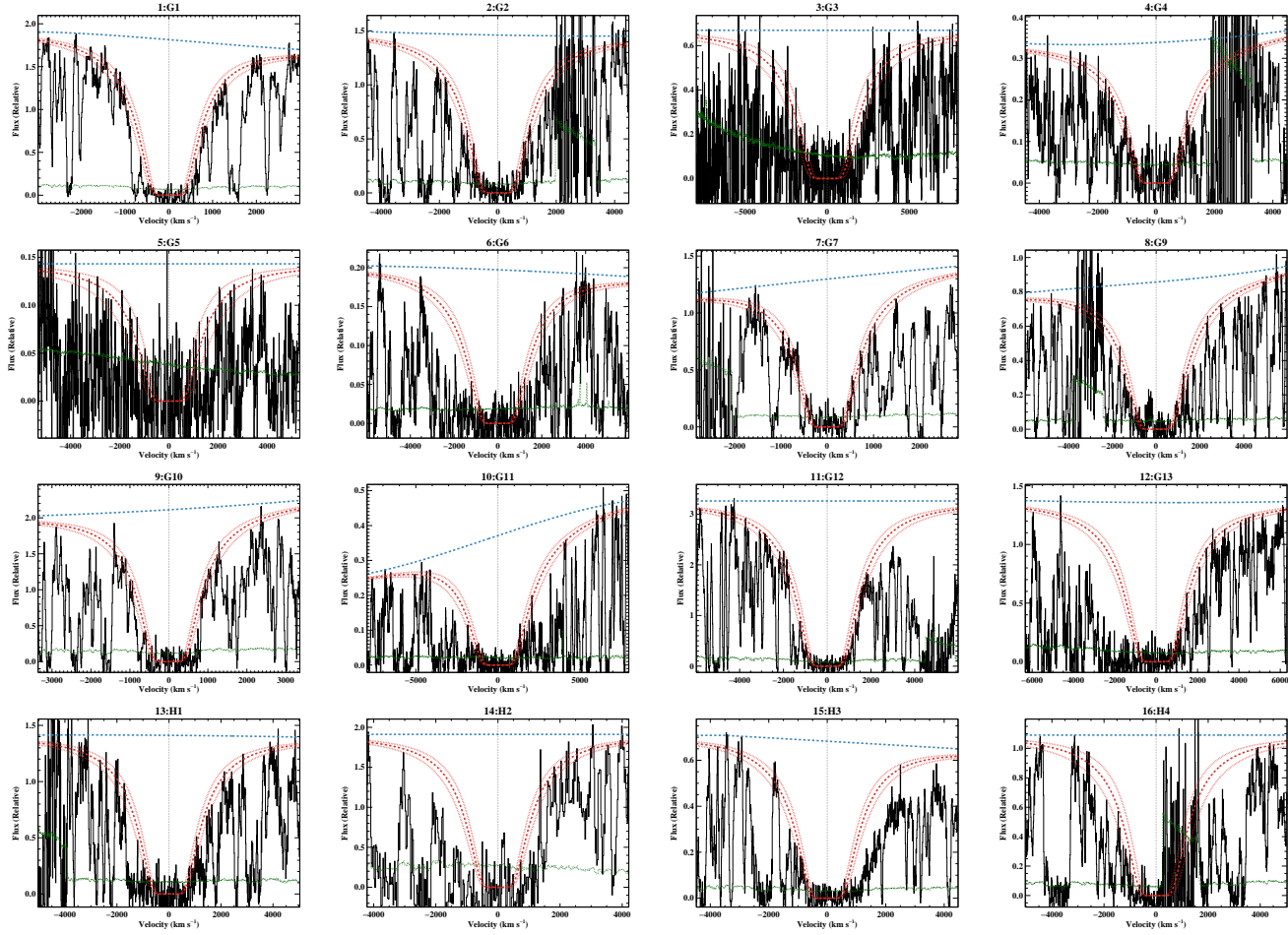


Figure 13. Voigt profiles of the Ly α absorption line of the targeted DLAs. In each panel, we superimpose on the data (black histograms) the quasar continuum level (blue dashed line), the absorption line models (red long-dashed line), and the corresponding 1σ errors (red dotted lines) for the main hydrogen component only. Uncertainties on the flux are shown by a green dotted line, while the systemic redshift of each DLA is marked by vertical gray dotted line.

0.07 – 0.12 dex. Following this analysis, for the quasars with ESI and MagE spectra, errors on the column densities are estimated to be ~ 0.10 dex and ~ 0.15 dex at lower S/N . At the lower redshift of our DLAs ($z \sim 3$), contamination from the Ly α forest is less important and the simulations in Rafelski et al. (2014) suggest that systematic errors are smaller than the quoted errors. Column densities are more uncertain at the lower resolutions and lower S/N of the SDSS spectra, with estimated errors between ~ 0.15 – 0.20 dex. These errors are also consistent with the dispersion found by Jorgenson et al. (2013) when comparing the H I column densities measured in MagE and SDSS spectra. Given that our ESI spectrum does not cover the Ly α transition for the DLA at $z_{\text{dla}} = 1.8639$ in the field 21:H9, we take the column density value from Ledoux et al. (2006). The top panel of Figure 12 shows the column density distribution of the targeted DLAs. Our selection is dictated purely by redshift separations between the intervening DLAs and LLSs, and thus our sample includes a wide range of column densities, which can be considered typical of the general DLA populations. We note, however, that this sample is not a strict statistical selection from the observed column density distribution function.

In Table 1, we also list the H I column densities of the higher redshift blocking systems. For DLAs or sub-DLAs which exhibit a clear Voigt profile, column densities are measured as done for

the lower redshift DLAs. Some complications arise from systems which are proximate to the quasar (flagged by an asterisk in Table 1), as accurate modeling of the quasar continuum near the Ly α emission line is required for a reliable estimate of N_{HI} . For the most difficult cases, we therefore quote only a conservative lower limit. For systems with $N_{\text{HI}} \lesssim 10^{19} \text{ cm}^{-2}$ instead, we quote lower limits on the column density as inferred from the transmitted flux at the Lyman limit and the properties of the Lyman series, following Fumagalli et al. (2013).

4.3 Metallicities

We compute the gas-phase metallicity for the targeted DLAs for which we have new echelle data, following the procedures discussed in Prochaska et al. (2003b) and Rafelski et al. (2012). The basics are only briefly summarized here. We continuum normalize each quasar either with a polynomial function, which we fit to the data redward to the quasar Ly α emission line, or with a spline function constrained by pixels without evident IGM absorption (see e.g. Fumagalli et al. 2013). Metallicities are then computed using the apparent optical depth method (Savage & Sembach 1991) that we apply, when possible, to multiple transitions of the same ions. Ionization corrections are not included, being negligible at the high H I column densities of DLAs. The derived metallicities $[\text{X}/\text{H}]_{\text{dla}}$,

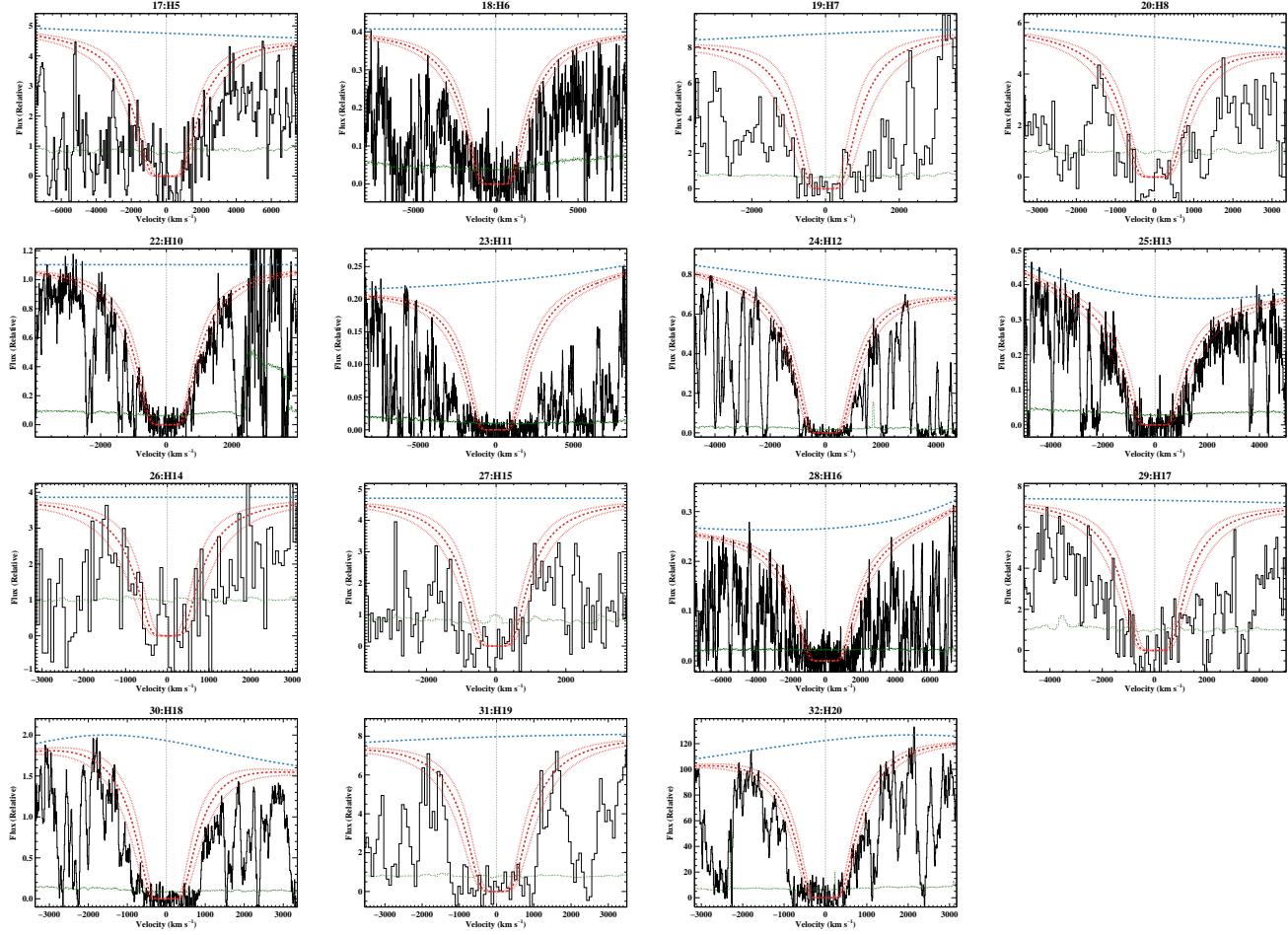


Figure 13 – continued Voigt profiles of the Ly α absorption line of the targeted DLAs. In each panel, we superimpose on the data (black histograms) the quasar continuum level (blue dashed line), the absorption line models (red long-dashed line), and the corresponding 1σ errors (red dotted lines) for the main hydrogen component only. Uncertainties on the flux are shown by a green dotted line, while the systemic redshift of each DLA is marked by vertical gray dotted line.

together with the ions used as tracers, are summarized in Table 1. Measurements of individual metal transitions in each system are further listed in the Appendix. We do not attempt to derive metallicities from the low resolution SDSS spectroscopy, as hidden saturation and noise would prevent a reliable determination of [X/H]_{dla} (e.g. Jorgenson et al. 2013). Finally, for the few systems with archival data, we adopt published values, as detailed in Table 4. The resultant distribution of metallicities is shown in Figure 14, which we compare against a model for the observed distribution in a large sample of $z > 1.5$ DLAs from Rafelski et al. (2012). Our selection does not bias our sample towards a particular class of DLAs, also because metallicities for most of the selected systems were unknown at the beginning of our survey. Similarly to the hydrogen column densities, the metal content of the selected DLAs is therefore consistent with that of the general DLA population at comparable redshifts, although our sample is not a strict statistical selection from the parent sample.

5 SUMMARY

In this second paper of a series, we have presented new imaging and spectroscopic data which we collected as part of a survey that aims to characterize the *in-situ* star formation rates of DLAs and the

connection between the DLA gas seen in absorption and galaxies seen in emission.

We have collected optical and near-UV multiwavelength imaging of 32 quasar fields, using HST, Keck, LBT, and the Magellan telescopes. These sightlines have been selected because of the presence of both high redshift ($z \sim 3.5$) optically-thick absorption systems and lower redshift ($z \sim 2.7$) DLAs. Given this fortuitous alignment, the high-redshift absorber acts as a natural blocking filter for the quasar light, which is completely absorbed below $\sim 4000 - 4500\text{\AA}$. In turn, this ‘Lyman limit technique’ allows us to image, blueward of the above blocking wavelengths, candidate DLA host galaxies at all impact parameters, including small separations ($\lesssim 1''$) from the quasars.

In this manuscript, we discussed the observations and data reduction for the HST and ground-based imaging, including details on the procedures adopted for photometric calibration and the preparation of the galaxy catalogues. We also discussed and analyzed new spectroscopic observations for 22 quasars, presenting new measurements of the hydrogen column densities and gas-phase metallicities of the intervening DLAs. Further, we compared the properties of the targeted DLAs to the properties of a larger sample of DLAs at comparable redshifts, concluding that our sample represents an unbiased selection with respect to metallicity and column density, although it is not a strict statistical selection

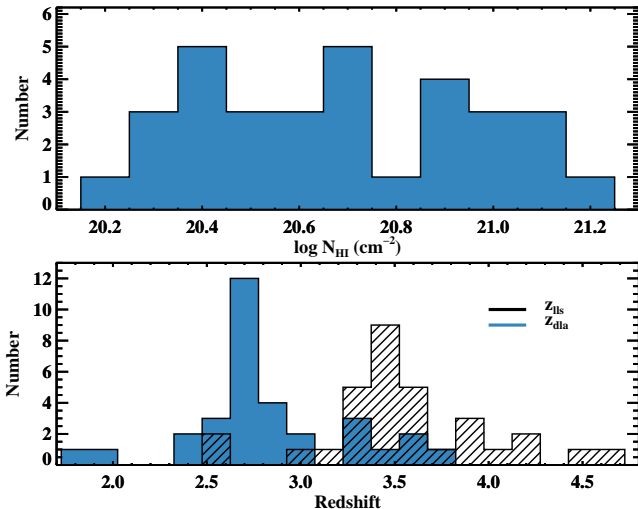


Figure 12. Top: The H I column density distribution of the targeted DLAs. Bottom: The redshift distributions of the targeted DLAs and of the higher redshift LLSSs that act as blocking filters. Our sample includes absorbers that are representative of the general DLA populations at $z \sim 2.5 - 3$, although they are not a statistical selection from the column density distribution function.

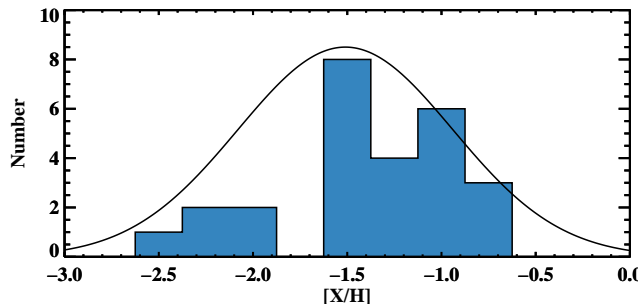


Figure 14. Metallicity distribution for the sub-sample of DLAs with echelle spectroscopy (blue histogram). Superimposed, a Gaussian with mean -1.51 and dispersion 0.57 that represents the observed distribution in a large sample of DLAs from Rafelski et al. (2012). Our sample includes DLAs over a large range of metallicities and it is representative of the general DLA population.

from the general population of $z \gtrsim 2$ DLAs. Therefore, this sample is useful to characterize the connection between neutral gas and galaxies and the rate with which stars are formed in DLAs, simply defined as systems with hydrogen column densities above $N_{\text{HI}} \geq 10^{20.3} \text{ cm}^{-2}$ without any prior information on the associated metal content or the presence of candidate host galaxies. This analysis will be the subject of the third paper in the series.

ACKNOWLEDGMENTS

This work is dedicated to the memory of our co-author and long-time collaborator, Arthur M. Wolfe. His passion for DLAs has accompanied us for many years, and it will continue to inspire our work. We thank Marc Rafelski, Marcel Neeleman, and Joseph Hennawi for their help during observations and for useful discussions. We thank Ryan Cooke for sharing the reduced spectrum of 32:H20. This paper has benefited from a careful review of an anonymous

referee. This work has been partially supported by NASA grants HST-GO-10878.05-A. MF acknowledges support by the Science and Technology Facilities Council [grant numbers ST/I001573/1, ST/F001166/1]. JMO thanks the office of the VPAA at St. Michaels College for travel support. JXP acknowledges support from NSF grant AST-1109447. NK acknowledges the Department of Science and Technology for support via a Ramanujan Fellowship. This work is based on observations made with the NASA/ESA Hubble Space Telescope (PID 11595), and obtained from the Hubble Legacy Archive, which is a collaboration between the Space Telescope Science Institute (STScI/NASA), the Space Telescope European Coordinating Facility (ST-ECF/ESA) and the Canadian Astronomy Data Centre (CADC/NRC/CSA). Some of the data presented herein were obtained at the W.M. Keck Observatory, which is operated as a scientific partnership among the California Institute of Technology, the University of California and the National Aeronautics and Space Administration. The Observatory was made possible by the generous financial support of the W.M. Keck Foundation. Part of the data presented in this manuscript have been collected through time awarded by NOAO (Proposal ID #2009A-0184). This paper includes data gathered with the 6.5 meter Magellan Telescopes located at Las Campanas Observatory, Chile, and data gathered at the Large Binocular Telescope (LBT). The LBT is an international collaboration among institutions in the United States, Italy and Germany. LBT Corporation partners are: The University of Arizona on behalf of the Arizona university system; Istituto Nazionale di Astrofisica, Italy LBT Beteiligungsgesellschaft, Germany, representing the Max-Planck Society, the Astrophysical Institute Potsdam, and Heidelberg University; The Ohio State University, and The Research Corporation, on behalf of The University of Notre Dame, University of Minnesota and University of Virginia. Imaging and spectroscopy data from the Sloan Digital Sky Survey have been a key element for the design and completion of this survey. This manuscript includes observations made with ESO Telescopes at the La Silla Paranal Observatory under programme ID 087.A-0022. For access to the data used in this paper, please contact the authors.

REFERENCES

- Asplund, M., Grevesse, N., Sauval, A. J., & Scott, P. 2009, *ARA&A*, 47, 481
- Bertin, E. 2006, Astronomical Data Analysis Software and Systems XV, 351, 112
- Bertin, E., & Arnouts, S. 1996, *A&AS*, 117, 393
- Bertin, E., Mellier, Y., Radovich, M., et al. 2002, Astronomical Data Analysis Software and Systems XI, 281, 228
- Bochanski, J. J., Hennawi, J. F., Simcoe, R. A., et al. 2009, *PASP*, 121, 1409
- Cen, R. 2012, *ApJ*, 748, 121
- Cooke, J., Wolfe, A. M., Prochaska, J. X., & Gawiser, E. 2005, *ApJ*, 621, 596
- Christensen, L., Noterdaeme, P., Petitjean, P., Ledoux, C., & Fynbo, J. P. U. 2009, *A&A*, 505, 1007
- Dressler, A., Hare, T., Bigelow, B. C., & Osip, D. J. 2006, *Proc. SPIE*, 6269
- Fitzpatrick, E. L. 1999, *PASP*, 111, 63
- Fumagalli, M., O'Meara, J. M., Prochaska, J. X., & Kanekar, N. 2010, *MNRAS*, 408, 362
- Fumagalli, M., O'Meara, J. M., Prochaska, J. X., & Worseck, G. 2013, *ApJ*, 775, 78

- Fukugita, M., Ichikawa, T., Gunn, J. E., et al. 1996, AJ, 111, 1748
- Fynbo J. U., Møller P., Warren S. J., 1999, MNRAS, 305, 849
- Fynbo, J. P. U., Laursen, P., Ledoux, C., et al. 2010, MNRAS, 408, 2128
- Galametz, A., Grazian, A., Fontana, A., et al. 2013, ApJS, 206, 10
- Gawiser, E., van Dokkum, P. G., Herrera, D., et al. 2006, ApJS, 162, 1
- Gunn, J. E., & Stryker, L. L. 1983, ApJS, 52, 121
- Guo, Y., Ferguson, H. C., Giavalisco, M., et al. 2013, ApJS, 207, 24
- Jorgenson, R. A., Murphy, M. T., & Thompson, R. 2013, MNRAS, 435, 482
- Jorgenson, R. A., & Wolfe, A. M. 2014, ApJ, 785, 16
- Kent, S. M. 1985, PASP, 97, 165
- Krisciunas, K., Bastola, D., Espinoza, J., et al. 2013, AJ, 145, 11
- Krogager, J.-K., Fynbo, J. P. U., Møller, P., et al. 2012, MNRAS, 424, L1
- Komatsu, E., Smith, K. M., Dunkley, J., et al. 2011, ApJS, 192, 18
- Landolt, A. U. 1992, AJ, 104, 340
- Le Brun, V., Bergeron, J., Boisse, P., & Deharveng, J. M. 1997, A&A, 321, 733
- Ledoux, C., Petitjean, P., Fynbo, J. P. U., Møller, P., & Srianand, R. 2006, A&A, 457, 71
- Lupton, R. H., Gunn, J. E., & Szalay, A. S. 1999, AJ, 118, 1406
- Marshall, J. L., Burles, S., Thompson, I. B., et al. 2008, Proc. SPIE, 7014,
- Møller, P., Fynbo, J. P. U., Ledoux, C., & Nilsson, K. K. 2013, MNRAS, 430, 2680
- Moller, P., & Warren, S. J. 1998, MNRAS, 299, 661
- Morton, D. C. 2003, ApJS, 149, 205
- Nagamine, K., Wolfe, A. M., Hernquist, L., & Springel, V. 2007, ApJ, 660, 945
- Neeleman, M., Wolfe, A. M., Prochaska, J. X., & Rafelski, M. 2013, ApJ, 769, 54
- Noterdaeme, P., Petitjean, P., Ledoux, C., & Srianand, R. 2009, A&A, 505, 1087
- Noterdaeme, P., Petitjean, P., Carithers, W. C., et al. 2012, A&A, 547, L1
- Noterdaeme, P., Laursen, P., Petitjean, P., et al. 2012, A&A, 540, A63
- O'Meara, J. M., Chen, H.-W., & Kaplan, D. L. 2006, ApJ, 642, L9
- Oke, J. B., Cohen, J. G., Carr, M., et al. 1995, PASP, 107, 375
- Oke, J. B. 1990, AJ, 99, 1621
- Pedichini, F., Giallongo, E., Ragazzoni, R., et al. 2003, Proc. SPIE, 4841, 815
- Péroux, C., Bouché, N., Kulkarni, V. P., York, D. G., & Vladilo, G. 2011, MNRAS, 410, 2237
- Prochaska, J. X., & Wolfe, A. M. 2009, ApJ, 696, 1543
- Prochaska, J. X., Wolfe, A. M., Howk, J. C., et al. 2007, ApJS, 171, 29
- Prochaska, J. X., Gawiser, E., Wolfe, A. M., Castro, S., & Djorgovski, S. G. 2003, ApJ, 595, L9
- Prochaska, J. X., Gawiser, E., Wolfe, A. M., Cooke, J., & Gelino, D. 2003, ApJS, 147, 227
- Rafelski, M., Wolfe, A. M., Prochaska, J. X., Neeleman, M., & Mendez, A. J. 2012, ApJ, 755, 89
- Rafelski, M., Neeleman, M., Fumagalli, M., Wolfe, A. M., & Prochaska, J. X. 2014, ApJ, 782, L29
- Rauch, M., Haehnelt, M., Bunker, A., et al. 2008, ApJ, 681, 856
- Rockosi, C., Stover, R., Kibrick, R., et al. 2010, Proc. SPIE, 7735,
- Savage, B. D., & Sembach, K. R. 1991, ApJ, 379, 245
- Schlafly, E. F., & Finkbeiner, D. P. 2011, ApJ, 737, 103
- Schlegel, D. J., Finkbeiner, D. P., & Davis, M. 1998, ApJ, 500, 525
- Schneider, D. P., Hall, P. B., Richards, G. T., et al. 2007, AJ, 134, 102
- Schulze, S., Fynbo, J. P. U., Milvang-Jensen, B., et al. 2012, A&A, 546, A20
- Sheinis, A. I., Bolte, M., Epps, H. W., et al. 2002, PASP, 114, 851
- Smith, J. A., Tucker, D. L., Kent, S., et al. 2002, AJ, 123, 2121
- Steidel, C. C., & Hamilton, D. 1992, AJ, 104, 941
- van Dokkum, P. G. 2001, PASP, 113, 1420
- Vernet, J., Dekker, H., D'Odorico, S., et al. 2011, A&A, 536, A105
- Warren, S. J., Møller, P., Fall, S. M., & Jakobsen, P. 2001, MNRAS, 326, 759
- Windhorst, R. A., Burstein, D., Mathis, D. F., et al. 1991, ApJ, 380, 362
- Winn, J. N., Hewitt, J. N., Schechter, P. L., et al. 2000, AJ, 120, 2868
- Wolfe, A. M., Turnshek, D. A., Smith, H. E., & Cohen, R. D. 1986, ApJS, 61, 249
- Wolfe, A. M., Gawiser, E., & Prochaska, J. X. 2005, ARA&A, 43, 861
- Wolfe, A. M., Prochaska, J. X., Jorgenson, R. A., & Rafelski, M. 2008, ApJ, 681, 881
- Zafar, T., Péroux, C., Popping, A., et al. 2013, A&A, 556, A141

APPENDIX A: NEW METALLICITY MEASUREMENTS

In this Appendix, we present details of the metallicity measurements for the intervening DLAs with new echelle spectra. A summary of the metallicities together with the α - element, zinc, and iron abundances is provided in Table A1. The best estimate for the DLA metallicity $[X/H]_{\text{dla}}$, which we infer assuming solar abundance pattern (Asplund et al. 2009), is also reported in Table 1. In Tables A2-A24, we list instead all the metal transitions measured in each DLA. For each ionic transition, we provide information on the adopted wavelength λ , the oscillator strength f from Morton (2003), and the velocity window v_{int} over which we measure equivalent widths W_λ and column densities N . The adopted column density for each ion N_{adopt} is also indicated. Velocity plots of all analyzed transitions are shown in Figures A1-A34. Additional information on the methodology here adopted can be found in Prochaska et al. (2003b) and Rafelski et al. (2012).

Table A1. Summary of all metallicity measurements for the DLAs with new echellette data.

Name ^a	f ^b _M	[M/H] ^c	$\sigma(M)$ ^c	f ^d _{α}	[α /H] ^e	$\sigma(\alpha)$ ^e	f ^f _{Zn}	[Zn/H] ^g	$\sigma(Zn)$ ^g	f ^h _{Fe}	[Fe/H] ⁱ	$\sigma(Fe)$ ⁱ
J211443.94-005532 (1:G1)	4	-0.63	0.11	4	-0.63	0.04	3	-0.78		4	-1.11	0.06
J073149.50+285448 (2:G2)	1	-1.45	0.17	1	-1.45	0.14	3	-1.16		1	-1.46	0.11
J095604.43+344415 (3:G3)	2	-1.00	0.17	2	-1.48		1	-1.00	0.09	1	-1.46	0.11
J234349.41-104742 (4:G4)	13	-1.27	0.20	13	-1.27	0.20	3	-0.63		1	-1.77	0.03
J034300.88-062229 (5:G5)	14	-2.02	0.26	3	-1.24		3	-0.72		1	-2.32	0.05
J235152.80+160048 (6:G6)	14	-2.03	0.20	2	-2.26		0			1	-2.33	0.06
J004219.74-102009 (7:G7)	14	-0.96	0.16	3	-0.19		0			1	-1.26	0.01
J094927.88+111518 (8:G9)	1	-0.95	0.10	1	-0.95	0.02	0			1	-1.20	0.05
J101806.28+310627 (9:G10)	13	-1.19	0.28	2	-1.48		3	-0.91		1	-1.50	0.03
J085143.72+233208 (10:G11)	2	-1.05	0.15	2	-1.04		1	-1.05	0.11	4	-1.51	0.05
J095605.09+144854 (11:G12)	1	-1.46	0.12	1	-1.46	0.07	1	-1.17	0.11	1	-1.63	0.08
J115130.48+353625 (12:G13)	1	-1.28	0.11	1	-1.28	0.05	0			1	-1.74	0.01
J212357.56-005350 (13:H1)	13	-1.59	0.15	13	-1.59	0.15	0			1	-1.88	0.02
J040718.06-441014 (14:H2)	1	-0.77	0.11	1	-0.77	0.05	1	-0.41	0.09	1	-0.59	0.03
J025518.58+004847 (15:H3)	1	-0.80	0.11	1	-0.80	0.05	3	-0.68		1	-1.28	0.02
J081618.99+482328 (16:H4)	1	-2.36	0.15	1	-2.36	0.02	3	-1.17		1	-2.41	0.03
J090810.36+023818 (18:H6)	1	-0.93	0.12	1	-0.93	0.07	3	-0.41		25	-1.31	0.29
J084424.24+124546 (21:H9)	1	-1.54	0.12	1	-1.54	0.06	1	-1.37	0.12	1	-1.66	0.06
J075155.10+451619 (22:H10)	1	-1.16	0.13	1	-1.16	0.09	3	-0.81		1	-1.80	0.03
J081813.14+072054 (23:H11)	13	-1.41	0.25	2	-1.67		3	-1.16		4	-1.36	0.07
J081813.05+263136 (24:H12)	13	-0.93	0.24	2	-1.17		3	-0.68		4	-1.10	0.05
J081114.32+393633 (25:H13)	13	-1.44	0.15	13	-1.44	0.15	3	-0.67		1	-1.70	0.03
J132005.97+131015 (32:H20)	1	-2.30	0.10	1	-2.30	0.02	3	-0.46		1	-2.81	0.09

^a Quasar name. ^b Flag indicating how the metallicity is computed: 1=[Si/H]; 2=[Zn/H]; 4=[S/H] ; 13=Bracketed by Si,Zn limits; 14=[Fe/H]+0.3 dex. ^c

Adopted metallicity with associated error. ^d Flag indicating how the abundance of α -elements is computed: 0=No measurement; 1=Si measurement; 2=Si lower limit; 3=Si upper limit; 4=[S/H] ; 5=[O/H] ; 13=S+Si limits. ^e Abundance of α -elements with associated error. ^f Flag indicating how the abundance of zinc is computed: 0=No measurement; 1=Zn measurement; 2=Zn lower limit; 3=Zn upper limit. ^g Abundance of zinc with associated error. ^h Flag indicating how the abundance of iron is computed: 0=No measurement; 1=Fe measurement; 2=Fe lower limit; 3=Fe upper limit; 4=[Ni/H]-0.1dex; 5=[Cr/H] -0.2dex; 6=[Al/H]; 11-16=Fe, Ni, Cr, Al limits; 25=Mean of Fe limits. ⁱ Abundance of iron with associated error. Note that none of the limits reported take into account the uncertainty in the N_{HI} value.

Table A2. Ionic column densities for J2114-0055 (1:G1) at $z_{\text{dla}} = 2.9181$

Ion	λ (Å)	$\log f$	Instr.	v_{int}^a (km s $^{-1}$)	W_{λ}^b (mÅ)	$\log N$	$\log N_{\text{adopt}}$
C I	1560.3092	-0.8808	ESI	[−100, 100]	< 18.0	< 12.98	< 12.98
	1656.9283	-0.8273	ESI	[−100, 100]	< 25.5	< 13.02	
C II	1334.5323	-0.8935	ESI	[−50, 50]	476.6 ± 3.3	> 14.85	> 14.85
	1548.1950	-0.7194	ESI	[−120, 120]	482.5 ± 9.0	14.23 ± 0.01	14.23 ± 0.01
C IV	1550.7700	-1.0213	ESI	[−120, 100]	290.3 ± 9.1	14.24 ± 0.02	
	1302.1685	-1.3110	ESI	[−70, 90]	380.8 ± 8.7	> 15.07	> 15.07
Al II	1670.7874	0.2742	ESI	[−100, 100]	504.7 ± 10.5	> 13.33	> 13.33
	1854.7164	-0.2684	ESI	[−150, 80]	272.6 ± 11.0	13.34 ± 0.02	13.33 ± 0.02
Al III	1862.7895	-0.5719	ESI	[−100, 100]	124.2 ± 14.4	13.27 ± 0.05	
	1190.4158	-0.6017	ESI	[−120, 120]	487.1 ± 14.4	> 14.51	15.00 ± 0.06
Si II	1260.4221	0.0030	ESI	[−100, 100]	626.0 ± 10.5	> 14.03	
	1304.3702	-1.0269	ESI	[−100, 100]	336.2 ± 9.9	> 14.66	
Si IV	1526.7066	-0.8962	ESI	[−120, 90]	426.0 ± 10.3	> 14.55	
	1808.0130	-2.6603	ESI	[−60, 60]	58.1 ± 7.8	15.00 ± 0.06	
S II	1393.7550	-0.2774	ESI	[−140, 100]	351.6 ± 5.5	> 13.71	13.85 ± 0.01
	1402.7700	-0.5817	ESI	[−120, 90]	260.8 ± 5.6	13.85 ± 0.01	
Cr II	1250.5840	-2.2634	ESI	[−50, 50]	< 20.3	< 14.63	14.77 ± 0.04
	1253.8110	-1.9634	ESI	[−50, 110]	72.8 ± 12.2	14.70 ± 0.08	
Fe II	1259.5190	-1.7894	ESI	[−60, 60]	115.2 ± 9.8	14.80 ± 0.04	
	2056.2539	-0.9788	ESI	[−70, 70]	32.0 ± 10.3	12.93 ± 0.14	12.93 ± 0.14
Ni II	2066.1610	-1.2882	ESI	[−70, 70]	< 22.7	< 13.25	
	2249.8768	-2.7397	ESI	[−60, 60]	< 18.9	< 14.55	> 14.44
Zn II	2260.7805	-2.6126	ESI	[−60, 60]	< 19.4	< 14.43	
	2344.2140	-0.9431	ESI	[−100, 100]	488.0 ± 15.1	> 14.19	
Fe II	2374.4612	-1.5045	ESI	[−80, 80]	319.4 ± 19.1	> 14.44	
	2382.7650	-0.4949	ESI	[−100, 100]	659.0 ± 27.1	> 13.94	
Ni II	1454.8420	-1.4908	ESI	[−50, 50]	< 13.8	< 13.53	13.44 ± 0.06
	1709.6042	-1.4895	ESI	[−50, 50]	30.9 ± 6.8	13.60 ± 0.09	
Zn II	1741.5531	-1.3696	ESI	[−50, 50]	28.3 ± 4.4	13.40 ± 0.07	
	1751.9157	-1.5575	ESI	[−50, 50]	< 10.2	< 13.31	
	2026.1360	-0.3107	ESI	[−40, 40]	< 14.5	< 12.10	< 12.10

^a Velocity interval over which the equivalent width and column density are measured. ^b Rest equivalent width.

Table A3. Ionic column densities for J0731+2854 (2:G2) at $z_{\text{dla}} = 2.6878$

Ion	λ (Å)	$\log f$	Instr.	v_{int}^a (km s $^{-1}$)	W_{λ}^b (mA)	$\log N$	$\log N_{\text{adopt}}$
C I	1560.3092	-0.8808	ESI	[−100, 100]	< 13.1	< 12.84	< 12.84
C II	1334.5323	-0.8935	ESI	[−70, 70]	304.9 ± 10.1	> 14.49	> 14.49
C IV	1548.1950 1550.7700	-0.7194 -1.0213	ESI ESI	[−100, 100] [−100, 50]	116.9 ± 5.6 111.8 ± 4.9	13.50 ± 0.02 < 13.80	13.50 ± 0.02
Al II	1670.7874	0.2742	ESI	[−70, 70]	210.7 ± 7.8	> 12.87	> 12.87
Al III	1854.7164	-0.2684	ESI	[−70, 70]	< 18.4	< 12.23	< 12.23
Si II	1193.2897 1808.0130	-0.3018 -2.6603	ESI ESI	[−70, 70] [−50, 50]	337.6 ± 11.7 26.9 ± 8.6	> 14.08 14.66 ± 0.14	14.66 ± 0.14
Si IV	1402.7700	-0.5817	ESI	[−100, 200]	257.3 ± 13.0	< 13.82	< 13.82
Mn II	2594.4990 2606.4620	-0.5670 -0.7151	ESI ESI	[−50, 50] [−50, 50]	< 57.2 < 61.2	< 12.72 < 12.91	< 12.72
Fe II	1608.4511 1611.2005 2249.8768 2260.7805 2344.2140 2374.4612 2382.7650 2586.6500 2600.1729	-1.2366 -2.8665 -2.7397 -2.6126 -0.9431 -1.5045 -0.4949 -1.1605 -0.6216	ESI ESI ESI ESI ESI ESI ESI ESI ESI	[−50, 50] [−50, 50] [−40, 40] [−40, 40] [−70, 60] [−50, 50] [−60, 60] [−50, 50] [−60, 60]	155.1 ± 7.1 < 15.8 < 22.7 40.6 ± 10.5 350.7 ± 9.1 198.1 ± 7.9 396.3 ± 7.9 309.6 ± 25.7 417.3 ± 23.5	> 14.23 < 14.89 < 14.64 14.59 ± 0.11 > 14.06 > 14.23 > 13.71 > 14.04 > 13.73	14.59 ± 0.11
Ni II	1709.6042 1741.5531 1751.9157	-1.4895 -1.3696 -1.5575	ESI ESI ESI	[−40, 40] [−30, 80] [−50, 50]	< 14.7 89.3 ± 8.7 29.4 ± 8.4	< 13.43 13.98 ± 0.04 13.64 ± 0.12	13.88 ± 0.04
Zn II	2026.1360	-0.3107	ESI	[−30, 30]	< 13.8	< 12.07	< 12.07

^a Velocity interval over which the equivalent width and column density are measured. ^b Rest equivalent width.

Table A4. Ionic column densities for J0956+3444 (3:G3) at $z_{\text{dla}} = 2.3887$

Ion	λ (Å)	$\log f$	Instr.	v_{int}^a (km s $^{-1}$)	W_{λ}^b (mÅ)	$\log N$	$\log N_{\text{adopt}}$
C I	1656.9283	-0.8273	ESI	[-50, 50]	< 20.3	< 12.91	< 12.91
C IV	1550.7700	-1.0213	ESI	[-140, 150]	765.3 ± 13.8	> 14.78	> 14.78
O I	1302.1685	-1.3110	ESI	[-150, 150]	886.4 ± 23.6	> 15.45	> 15.45
Al II	1670.7874	0.2742	ESI	[-130, 130]	778.6 ± 15.1	> 13.62	> 13.62
Al III	1854.7164	-0.2684	ESI	[-80, 80]	240.7 ± 14.1	13.25 ± 0.03	13.25 ± 0.03
Si II	1304.3702	-1.0269	ESI	[-120, 120]	780.9 ± 20.4	> 15.13	> 15.13
	1526.7066	-0.8962	ESI	[-180, 180]	877.5 ± 15.9	> 14.89	
Cr II	2056.2539	-0.9788	ESI	[-120, 120]	129.5 ± 17.7	13.56 ± 0.06	13.57 ± 0.05
	2062.2340	-1.1079	ESI	[-120, 120]	130.6 ± 18.0	< 13.69	
	2066.1610	-1.2882	ESI	[-120, 120]	72.7 ± 18.4	13.62 ± 0.10	
Mn II	2594.4990	-0.5670	ESI	[-60, 60]	116.5 ± 18.6	12.91 ± 0.07	12.91 ± 0.07
Fe II	1608.4511	-1.2366	ESI	[-150, 150]	625.6 ± 11.3	> 15.03	15.09 ± 0.11
	1611.2005	-2.8665	ESI	[-100, 60]	35.9 ± 9.6	15.09 ± 0.11	
	2344.2140	-0.9431	ESI	[-150, 150]	1043.0 ± 20.5	> 14.67	
	2374.4612	-1.5045	ESI	[-150, 150]	756.2 ± 23.5	> 15.07	
	2382.7650	-0.4949	ESI	[-150, 150]	1234.8 ± 22.6	> 14.30	
	2586.6500	-1.1605	ESI	[-150, 150]	1116.5 ± 34.9	> 14.84	
	2600.1729	-0.6216	ESI	[-150, 150]	1334.0 ± 21.8	> 14.38	
Ni II	1709.6042	-1.4895	ESI	[-100, 100]	86.9 ± 18.1	14.06 ± 0.09	14.02 ± 0.05
	1741.5531	-1.3696	ESI	[-100, 100]	97.5 ± 18.9	13.99 ± 0.08	
	1751.9157	-1.5575	ESI	[-100, 100]	66.6 ± 18.7	14.00 ± 0.11	
Zn II	2026.1360	-0.3107	ESI	[-100, 100]	69.7 ± 15.6	12.73 ± 0.09	12.73 ± 0.09

^a Velocity interval over which the equivalent width and column density are measured. ^b Rest equivalent width.

Table A5. Ionic column densities for J2343-1047 (4:G4) at $z_{\text{dla}} = 2.6880$

Ion	λ (Å)	$\log f$	Instr.	v_{int}^a (km s $^{-1}$)	W_{λ}^b (mÅ)	$\log N$	$\log N_{\text{adopt}}$
C I	1560.3092	-0.8808	ESI	[−80, 80]	< 19.8	< 13.03	< 13.03
	1656.9283	-0.8273	ESI	[−80, 80]	< 35.1	< 13.16	
C II	1334.5323	-0.8935	ESI	[−80, 50]	527.4 ± 17.2	> 14.82	> 14.82
C IV	1548.1950	-0.7194	ESI	[−150, 150]	490.6 ± 10.1	< 14.19	< 14.19
O I	1302.1685	-1.3110	ESI	[−80, 60]	504.8 ± 11.6	> 15.24	> 15.24
Al II	1670.7874	0.2742	ESI	[−120, 90]	328.9 ± 16.6	> 13.03	> 13.03
Si II	1260.4221	0.0030	ESI	[−130, 80]	534.2 ± 31.6	> 13.90	> 14.64
	1304.3702	-1.0269	ESI	[−50, 80]	329.9 ± 13.3	> 14.64	
	1526.7066	-0.8962	ESI	[−100, 130]	425.5 ± 5.5	> 14.47	
	1808.0130	-2.6603	ESI	[−100, 100]	< 45.5	< 15.04	
Fe II	1608.4511	-1.2366	ESI	[−100, 100]	198.4 ± 23.4	14.29 ± 0.05	14.27 ± 0.03
	1611.2005	-2.8665	ESI	[−80, 80]	< 40.5	< 15.30	
	2260.7805	-2.6126	ESI	[−100, 100]	< 63.9	< 14.94	
	2344.2140	-0.9431	ESI	[−130, 130]	480.6 ± 27.3	> 14.13	
	2374.4612	-1.5045	ESI	[−100, 80]	238.1 ± 15.7	14.27 ± 0.03	
	2382.7650	-0.4949	ESI	[−150, 150]	711.2 ± 18.4	> 13.99	
	2600.1729	-0.6216	ESI	[−150, 150]	814.2 ± 77.7	> 14.07	
Ni II	1741.5531	-1.3696	ESI	[−100, 100]	< 39.4	< 13.71	< 13.71
	1751.9157	-1.5575	ESI	[−100, 100]	< 36.3	< 13.88	
Zn II	2026.1360	-0.3107	ESI	[−100, 100]	< 47.5	< 12.60	< 12.60

^a Velocity interval over which the equivalent width and column density are measured. ^b Rest equivalent width.

Table A6. Ionic column densities for J0343-0622 (5:G5) at $z_{\text{dla}} = 2.5713$

Ion	λ (Å)	$\log f$	Instr.	v_{int}^a (km s $^{-1}$)	W_{λ}^b (mA)	$\log N$	$\log N_{\text{adopt}}$
C I							
	1656.9283	-0.8273	ESI	[-60, 60]	< 65.6	< 13.40	< 13.40
Al II	1670.7874	0.2742	ESI	[-80, 60]	154.4 ± 28.3	12.62 ± 0.08	12.62 ± 0.08
Al III	1854.7164	-0.2684	ESI	[-80, 80]	< 65.2	< 12.77	< 12.77
Si II	1808.0130	-2.6603	ESI	[-80, 80]	< 43.9	< 15.02	< 15.02
Cr II	2056.2539	-0.9788	ESI	[-80, 80]	< 137.9	< 13.74	< 13.56
	2062.2340	-1.1079	ESI	[-80, 80]	< 69.2	< 13.56	
	2066.1610	-1.2882	ESI	[-80, 80]	< 63.8	< 13.70	
Mn II	2594.4990	-0.5670	ESI	[-80, 80]	< 112.3	< 13.04	< 13.04
Fe II	1608.4511	-1.2366	ESI	[-50, 70]	96.3 ± 13.0	13.93 ± 0.06	13.88 ± 0.05
	1611.2005	-2.8665	ESI	[-80, 80]	< 33.6	< 15.22	
	2260.7805	-2.6126	ESI	[-80, 80]	< 61.3	< 14.93	
	2344.2140	-0.9431	ESI	[-60, 60]	242.9 ± 28.6	> 13.75	
	2374.4612	-1.5045	ESI	[-40, 40]	74.9 ± 22.3	13.75 ± 0.13	
	2382.7650	-0.4949	ESI	[-50, 50]	260.5 ± 22.4	> 13.35	
	2586.6500	-1.1605	ESI	[-50, 40]	203.2 ± 37.8	> 13.81	
Ni II	1741.5531	-1.3696	ESI	[-80, 80]	< 49.9	< 13.83	< 13.83
Zn II	2026.1360	-0.3107	ESI	[-80, 80]	< 52.8	< 12.66	< 12.66

^a Velocity interval over which the equivalent width and column density are measured. ^b Rest equivalent width.

Table A7. Ionic column densities for J2351+1600 (6:G6) at $z_{\text{dla}} = 3.7861$

Ion	λ (Å)	$\log f$	Instr.	v_{int}^a (km s $^{-1}$)	W_{λ}^b (mÅ)	$\log N$	$\log N_{\text{adopt}}$
C I	1656.9283	-0.8273	ESI	[−100, 100]	< 47.3	< 13.32	< 13.32
C IV	1548.1950	-0.7194	ESI	[−100, 130]	105.9 ± 20.4	13.47 ± 0.08	13.47 ± 0.08
O I	1302.1685	-1.3110	ESI	[−100, 60]	363.7 ± 14.2	> 14.96	> 14.96
Al II	1670.7874	0.2742	ESI	[−40, 40]	108.8 ± 12.6	12.49 ± 0.05	12.49 ± 0.05
Al III	1862.7895	-0.5719	ESI	[−80, 80]	< 40.6	< 12.88	< 12.88
Si II	1526.7066	-0.8962	ESI	[−60, 70]	190.5 ± 22.6	> 14.10	> 14.10
	1808.0130	-2.6603	ESI	[−100, 70]	< 50.7	< 15.10	
Fe II	1608.4511	-1.2366	ESI	[−60, 60]	100.4 ± 13.8	13.97 ± 0.06	13.97 ± 0.06
Ni II	1454.8420	-1.4908	ESI	[−80, 80]	< 16.4	< 13.61	< 13.61

^a Velocity interval over which the equivalent width and column density are measured. ^b Rest equivalent width.

Table A8. Ionic column densities for J0042-1020 (7:G7) at $z_{\text{dla}} = 2.7544$

Ion	λ (Å)	$\log f$	Instr.	v_{int}^a (km s $^{-1}$)	W_{λ}^b (mÅ)	$\log N$	$\log N_{\text{adopt}}$
C I	1656.9283	-0.8273	ESI	[−80, 80]	< 20.2	< 12.93	< 12.93
C II	1334.5323	-0.8935	ESI	[−100, 220]	981.0 ± 11.0	> 15.07	> 15.07
O I	1302.1685	-1.3110	ESI	[−80, 160]	729.9 ± 12.5	> 15.32	> 15.31
Al II	1670.7874	0.2742	ESI	[−180, 200]	732.2 ± 14.4	> 13.42	> 13.42
Al III	1854.7164 1862.7895	-0.2684 -0.5719	ESI ESI	[−100, 100] [−100, 100]	< 23.9 < 24.8	< 12.35 < 12.65	< 12.35
Si II	1808.0130	-2.6603	ESI	[−120, 180]	186.8 ± 11.7	< 15.52	< 15.52
Cr II	2056.2539 2066.1610	-0.9788 -1.2882	ESI ESI	[−100, 100] [−100, 100]	< 34.5 < 24.7	< 13.15 < 13.29	< 13.15
Fe II	1608.4511 1611.2005 2249.8768 2260.7805 2344.2140 2374.4612 2600.1729	-1.2366 -2.8665 -2.7397 -2.6126 -0.9431 -1.5045 -0.6216	ESI ESI ESI ESI ESI ESI ESI	[−100, 190] [−100, 190] [−100, 190] [−100, 190] [−100, 190] [−100, 190] [−100, 190]	309.9 ± 9.2 < 20.3 < 39.0 < 37.1 627.1 ± 16.2 236.4 ± 19.7 925.4 ± 43.9	14.44 ± 0.01 < 14.99 < 14.85 < 14.70 > 14.17 14.23 ± 0.04 > 13.99	14.39 ± 0.01
Ni II	1709.6042 1741.5531 1751.9157	-1.4895 -1.3696 -1.5575	ESI ESI ESI	[−100, 100] [−100, 100] [−100, 100]	< 27.4 < 27.6 < 34.4	< 13.69 < 13.57 < 13.83	< 13.56

^a Velocity interval over which the equivalent width and column density are measured. ^b Rest equivalent width.

Table A9. Ionic column densities for J0949+1115 (8:G9) at $z_{\text{dla}} = 2.7584$

Ion	λ (Å)	$\log f$	Instr.	v_{int}^a (km s $^{-1}$)	W_{λ}^b (mÅ)	$\log N$	$\log N_{\text{adopt}}$
C I							
	1656.9283	-0.8273	ESI	[−100, 100]	< 15.8	< 12.82	< 12.82
Al II	1670.7874	0.2742	ESI	[−130, 130]	777.7 ± 7.4	> 13.60	> 13.60
Al III	1854.7164	-0.2684	ESI	[−100, 100]	178.4 ± 8.7	13.09 ± 0.02	13.05 ± 0.02
	1862.7895	-0.5719	ESI	[−100, 100]	61.4 ± 9.0	12.90 ± 0.06	
Si II	1304.3702	-1.0269	ESI	[−100, 100]	533.5 ± 9.0	> 14.95	15.41 ± 0.02
	1808.0130	-2.6603	ESI	[−100, 100]	145.4 ± 7.7	15.41 ± 0.02	
Cr II	2056.2539	-0.9788	ESI	[−100, 100]	80.2 ± 9.7	13.34 ± 0.05	13.31 ± 0.05
	2062.2340	-1.1079	ESI	[−100, 70]	57.8 ± 10.1	< 13.32	
	2066.1610	-1.2882	ESI	[−100, 100]	28.4 ± 9.0	13.19 ± 0.13	
Fe II	1608.4511	-1.2366	ESI	[−120, 120]	522.3 ± 6.4	> 14.88	15.10 ± 0.05
	2260.7805	-2.6126	ESI	[−100, 100]	128.4 ± 13.2	15.10 ± 0.05	
	2344.2140	-0.9431	ESI	[−100, 100]	981.7 ± 8.2	> 14.62	
	2374.4612	-1.5045	ESI	[−100, 100]	916.8 ± 20.5	> 15.06	
	2382.7650	-0.4949	ESI	[−100, 100]	1185.8 ± 7.5	> 14.26	
	2586.6500	-1.1605	ESI	[−100, 100]	804.1 ± 35.8	> 14.58	
	2600.1729	-0.6216	ESI	[−180, 180]	1420.0 ± 26.2	> 14.35	
Ni II	1709.6042	-1.4895	ESI	[−100, 100]	50.5 ± 9.3	13.80 ± 0.08	13.72 ± 0.06
	1741.5531	-1.3696	ESI	[−100, 100]	45.0 ± 10.4	13.63 ± 0.10	
	1751.9157	-1.5575	ESI	[−100, 100]	40.3 ± 11.3	13.75 ± 0.12	

^a Velocity interval over which the equivalent width and column density are measured. ^b Rest equivalent width.

Table A10. Ionic column densities for J1018+3106 (9:G10) at $z_{\text{dla}} = 2.4592$

Ion	λ (Å)	$\log f$	Instr.	v_{int}^a (km s $^{-1}$)	W_{λ}^b (mA)	$\log N$	$\log N_{\text{adopt}}$
C II							
	1334.5323	-0.8935	ESI	[-170, 60]	455.3 ± 10.8	> 14.70	> 14.70
O I	1302.1685	-1.3110	ESI	[-120, 80]	480.0 ± 8.8	> 15.18	> 15.18
Al II							
	1670.7874	0.2742	ESI	[-80, 80]	296.4 ± 5.7	> 13.10	> 13.10
Al III							
	1854.7164	-0.2684	ESI	[-70, 70]	102.3 ± 8.0	12.86 ± 0.03	12.86 ± 0.03
	1862.7895	-0.5719	ESI	[-70, 70]	53.1 ± 7.9	12.85 ± 0.06	
Si II							
	1526.7066	-0.8962	ESI	[-70, 70]	304.6 ± 7.0	> 14.38	> 14.38
	1808.0130	-2.6603	ESI	[-70, 70]	109.6 ± 7.3	< 15.30	
Si IV							
	1393.7550	-0.2774	ESI	[-70, 70]	302.6 ± 6.2	> 13.83	> 13.83
S II							
	1250.5840	-2.2634	ESI	[-50, 50]	< 22.7	< 14.66	< 14.65
Cr II							
	2062.2340	-1.1079	ESI	[-50, 50]	< 12.0	< 12.80	< 12.80
	2066.1610	-1.2882	ESI	[-50, 50]	< 12.1	< 12.96	
Mn II							
	2594.4990	-0.5670	ESI	[-50, 50]	33.8 ± 9.9	12.34 ± 0.13	12.34 ± 0.13
	2606.4620	-0.7151	ESI	[-50, 50]	< 21.0	< 12.44	
Fe II							
	2249.8768	-2.7397	ESI	[-50, 50]	< 16.2	< 14.48	14.30 ± 0.03
	2260.7805	-2.6126	ESI	[-50, 50]	< 15.4	< 14.33	
	2344.2140	-0.9431	ESI	[-50, 50]	361.4 ± 7.8	> 14.09	
	2374.4612	-1.5045	ESI	[-70, 50]	240.6 ± 13.2	14.30 ± 0.03	
	2382.7650	-0.4949	ESI	[-80, 60]	500.6 ± 12.0	> 13.80	
	2586.6500	-1.1605	ESI	[-50, 50]	367.1 ± 10.3	> 14.19	
	2600.1729	-0.6216	ESI	[-50, 50]	510.8 ± 7.8	> 13.89	
Ni II							
	1709.6042	-1.4895	ESI	[-50, 50]	< 13.8	< 13.40	< 13.26
	1741.5531	-1.3696	ESI	[-50, 50]	< 13.8	< 13.26	
	1751.9157	-1.5575	ESI	[-50, 50]	< 13.3	< 13.42	
Zn II							
	2026.1360	-0.3107	ESI	[-50, 50]	< 13.7	< 12.07	< 12.07

^a Velocity interval over which the equivalent width and column density are measured. ^b Rest equivalent width.

Table A11. Ionic column densities for J0851+2332 (10:G11) at $z_{\text{dla}} = 3.5297$

Ion	λ (Å)	$\log f$	Instr.	v_{int}^a (km s $^{-1}$)	W_{λ}^b (mÅ)	$\log N$	$\log N_{\text{adopt}}$
C I	1560.3092	-0.8808	ESI	[−100, 100]	< 24.9	< 13.12	< 13.04
	1656.9283	-0.8273	ESI	[−100, 100]	< 25.6	< 13.04	
C II	1334.5323	-0.8935	ESI	[−200, 210]	1826.6 ± 12.5	> 15.42	> 15.42
	1548.1950	-0.7194	ESI	[−270, 250]	1144.3 ± 16.2	> 14.72	> 14.76
C IV	1550.7700	-1.0213	ESI	[−250, 250]	811.7 ± 16.5	> 14.76	
	1302.1685	-1.3110	ESI	[−190, 260]	1768.4 ± 19.0	> 15.82	> 15.82
O I	1670.7874	0.2742	ESI	[−200, 250]	1864.2 ± 13.5	> 14.00	> 14.00
	1260.4221	0.0030	ESI	[−190, 220]	1670.7 ± 10.9	> 14.52	> 15.57
Al II	1304.3702	-1.0269	ESI	[−230, 260]	1958.1 ± 17.1	> 15.57	
	1526.7066	-0.8962	ESI	[−220, 250]	1765.4 ± 11.0	> 15.22	
Fe II	1608.4511	-1.2366	ESI	[−200, 250]	1149.1 ± 18.4	> 15.16	> 15.16
	1611.2005	-2.8665	ESI	[−80, 80]	< 33.2	< 15.23	
Ni II	1709.6042	-1.4895	ESI	[−100, 100]	58.2 ± 11.5	13.86 ± 0.09	13.89 ± 0.05
	1741.5531	-1.3696	ESI	[−100, 100]	87.8 ± 13.3	13.91 ± 0.07	
Zn II	1751.9157	-1.5575	ESI	[−100, 100]	< 33.5	< 13.84	
	2026.1360	-0.3107	ESI	[−80, 100]	77.2 ± 19.5	12.68 ± 0.11	12.68 ± 0.11

^a Velocity interval over which the equivalent width and column density are measured. ^b Rest equivalent width.

Table A12. Ionic column densities for J0956+1448 (11:G12) at $z_{\text{dla}} = 2.6606$

Ion	λ (Å)	$\log f$	Instr.	v_{int}^a (km s $^{-1}$)	W_{λ}^b (mÅ)	$\log N$	$\log N_{\text{adopt}}$
C I	1560.3092	-0.8808	ESI	[−100, 100]	< 15.7	< 12.92	< 12.85
	1656.9283	-0.8273	ESI	[−100, 100]	< 16.9	< 12.85	
C IV	1548.1950	-0.7194	ESI	[−150, 60]	181.5 ± 6.8	13.74 ± 0.02	13.72 ± 0.01
	1550.7700	-1.0213	ESI	[−150, 50]	78.6 ± 7.0	13.64 ± 0.04	
N I	1200.2233	-1.0645	ESI	[−50, 50]	191.1 ± 6.4	< 14.41	14.36 ± 0.03
	1200.7098	-1.3665	ESI	[−50, 50]	101.1 ± 7.1	14.36 ± 0.03	
Al II	1670.7874	0.2742	ESI	[−120, 50]	325.1 ± 6.4	> 13.09	> 13.09
	1854.7164	-0.2684	ESI	[−50, 60]	46.1 ± 5.5	12.48 ± 0.05	12.46 ± 0.05
Al III	1862.7895	-0.5719	ESI	[−50, 60]	20.8 ± 5.4	12.41 ± 0.11	
	1526.7066	-0.8962	ESI	[−100, 100]	324.0 ± 5.5	> 14.40	14.90 ± 0.07
Si II	1808.0130	-2.6603	ESI	[−60, 50]	46.8 ± 7.4	14.90 ± 0.07	
	1393.7550	-0.2774	ESI	[−150, 50]	319.6 ± 7.4	13.67 ± 0.01	13.67 ± 0.01
Cr II	2056.2539	-0.9788	ESI	[−70, 80]	28.9 ± 9.0	12.89 ± 0.13	12.95 ± 0.10
	2062.2340	-1.1079	ESI	[−80, 80]	< 16.5	< 12.94	
Fe II	2066.1610	-1.2882	ESI	[−80, 80]	< 16.4	13.11 ± 0.14	
	1608.4511	-1.2366	ESI	[−70, 60]	209.9 ± 6.5	> 14.38	14.67 ± 0.08
Ni II	2249.8768	-2.7397	ESI	[−60, 20]	< 19.9	< 14.57	
	2260.7805	-2.6126	ESI	[−50, 20]	48.4 ± 8.3	14.67 ± 0.08	
Zn II	2344.2140	-0.9431	ESI	[−80, 50]	418.4 ± 6.5	> 14.13	
	2382.7650	-0.4949	ESI	[−100, 70]	743.8 ± 7.3	> 14.03	
Zn II	2586.6500	-1.1605	ESI	[−80, 50]	422.0 ± 22.2	> 14.24	
	2600.1729	-0.6216	ESI	[−80, 50]	584.4 ± 19.9	> 13.93	
Ni II	1751.9157	-1.5575	ESI	[−40, 70]	31.1 ± 7.1	13.64 ± 0.10	13.64 ± 0.10
	2026.1360	-0.3107	ESI	[−80, 80]	35.2 ± 9.1	12.31 ± 0.11	12.31 ± 0.11

^a Velocity interval over which the equivalent width and column density are measured. ^b Rest equivalent width.

Table A13. Ionic column densities for J1151+3536 (12:G13) at $z_{\text{dla}} = 2.5978$

Ion	λ (Å)	$\log f$	Instr.	v_{int}^a (km s $^{-1}$)	W_{λ}^b (mÅ)	$\log N$	$\log N_{\text{adopt}}$
C I							
	1656.9283	-0.8273	ESI	[−100, 100]	< 19.5	< 12.92	< 12.92
Al II	1670.7874	0.2742	ESI	[−110, 110]	619.9 ± 8.4	> 13.38	> 13.38
Al III	1854.7164	-0.2684	ESI	[−100, 100]	< 22.1	< 12.31	< 12.31
	1862.7895	-0.5719	ESI	[−100, 100]	< 21.1	< 12.59	
Si II	1808.0130	-2.6603	ESI	[−70, 80]	80.3 ± 9.3	15.13 ± 0.05	15.13 ± 0.05
Cr II	2066.1610	-1.2882	ESI	[−80, 80]	< 20.4	< 13.20	< 13.20
Fe II	1608.4511	-1.2366	ESI	[−180, 180]	401.1 ± 10.9	14.62 ± 0.01	14.61 ± 0.01
	1611.2005	-2.8665	ESI	[−100, 100]	< 18.1	< 14.95	
	2260.7805	-2.6126	ESI	[−180, 200]	< 34.8	< 14.68	
	2344.2140	-0.9431	ESI	[−180, 200]	954.3 ± 18.3	> 14.54	
	2374.4612	-1.5045	ESI	[−110, 120]	492.3 ± 11.3	14.61 ± 0.01	
	2382.7650	-0.4949	ESI	[−180, 180]	1252.3 ± 11.3	> 14.27	
	2600.1729	-0.6216	ESI	[−120, 130]	1297.0 ± 20.2	> 14.35	

^a Velocity interval over which the equivalent width and column density are measured. ^b Rest equivalent width.

Table A14. Ionic column densities for J2123-0053 (13:H1) at $z_{\text{dla}} = 2.7803$

Ion	λ (Å)	$\log f$	Instr.	v_{int}^a (km s $^{-1}$)	W_{λ}^b (mÅ)	$\log N$	$\log N_{\text{adopt}}$
C I	1560.3092	-0.8808	ESI	[−100, 100]	< 33.4	< 13.26	< 13.00
	1656.9283	-0.8273	ESI	[−100, 100]	< 23.6	< 13.00	
Al II	1670.7874	0.2742	ESI	[−150, 150]	543.3 ± 13.1	> 13.29	> 13.29
	1854.7164	-0.2684	ESI	[−50, 50]	66.5 ± 7.7	12.64 ± 0.05	12.65 ± 0.05
Al III	1862.7895	-0.5719	ESI	[−50, 50]	35.4 ± 7.5	12.66 ± 0.09	
	1526.7066	-0.8962	ESI	[−100, 160]	509.4 ± 11.2	> 14.54	> 14.54
Si II	1808.0130	-2.6603	ESI	[−60, 60]	< 20.9	< 14.71	
	2056.2539	-0.9788	ESI	[−50, 50]	< 18.9	< 12.87	< 12.87
	2062.2340	-1.1079	ESI	[−50, 50]	< 28.7	< 13.16	
Cr II	2066.1610	-1.2882	ESI	[−50, 50]	< 22.8	< 13.27	
	1608.4511	-1.2366	ESI	[−100, 120]	200.5 ± 11.9	14.28 ± 0.03	14.27 ± 0.02
	2260.7805	-2.6126	ESI	[−80, 120]	< 29.0	< 14.60	
Fe II	2344.2140	-0.9431	ESI	[−90, 140]	492.3 ± 13.5	> 14.13	
	2374.4612	-1.5045	ESI	[−80, 100]	223.7 ± 14.7	14.26 ± 0.03	
	2382.7650	-0.4949	ESI	[−100, 120]	763.2 ± 15.0	> 13.97	
	2586.6500	-1.1605	ESI	[−100, 100]	319.0 ± 39.2	> 14.08	
	2600.1729	-0.6216	ESI	[−100, 120]	808.0 ± 43.3	> 13.97	
Ni II	1709.6042	-1.4895	ESI	[−100, 100]	< 26.1	< 13.66	< 13.61
	1741.5531	-1.3696	ESI	[−100, 100]	< 31.6	< 13.61	
	1751.9157	-1.5575	ESI	[−100, 100]	< 28.7	< 13.76	

^a Velocity interval over which the equivalent width and column density are measured. ^b Rest equivalent width.

Table A15. Ionic column densities for J0407-4410 (14:H2) at $z_{\text{dla}} = 1.9127$

Ion	λ (Å)	$\log f$	Instr.	v_{int}^a (km s $^{-1}$)	W_{λ}^b (mÅ)	$\log N$	$\log N_{\text{adopt}}$
Mg II	2796.3520	-0.2130	MagE	[−200, 200]	1710.3 ± 31.2	> 14.01	> 14.27
	2803.5310	-0.5151	MagE	[−200, 200]	1569.2 ± 32.7	> 14.26	
Al III	1854.7164	-0.2684	MagE	[−300, 150]	240.8 ± 21.8	13.22 ± 0.04	13.22 ± 0.04
Si II	1808.0130	-2.6603	MagE	[−150, 150]	112.3 ± 14.0	15.29 ± 0.05	15.29 ± 0.05
Cr II	2056.2539	-0.9788	MagE	[−150, 150]	133.8 ± 14.9	13.56 ± 0.05	13.60 ± 0.04
	2066.1610	-1.2882	MagE	[−150, 150]	95.3 ± 13.3	13.70 ± 0.06	
Mn II	2576.8770	-0.4549	MagE	[−150, 150]	118.8 ± 15.0	12.79 ± 0.05	12.85 ± 0.04
	2594.4990	-0.5670	MagE	[−150, 150]	125.8 ± 14.9	12.92 ± 0.05	
Fe II	2249.8768	-2.7397	MagE	[−150, 150]	134.0 ± 19.7	15.24 ± 0.06	15.41 ± 0.03
	2260.7805	-2.6126	MagE	[−150, 150]	288.5 ± 17.4	15.47 ± 0.03	
	2344.2140	-0.9431	MagE	[−150, 150]	1039.6 ± 11.9	> 14.66	
	2374.4612	-1.5045	MagE	[−150, 150]	846.7 ± 12.4	> 14.99	
	2382.7650	-0.4949	MagE	[−150, 150]	1273.6 ± 11.2	> 14.27	
	2586.6500	-1.1605	MagE	[−150, 150]	1131.6 ± 12.7	> 14.82	
	2600.1729	-0.6216	MagE	[−150, 150]	1272.4 ± 12.3	> 14.34	
Ni II	1741.5531	-1.3696	MagE	[−150, 150]	111.8 ± 10.8	14.01 ± 0.04	14.02 ± 0.04
Zn II	2026.1360	-0.3107	MagE	[−150, 150]	99.9 ± 20.4	12.77 ± 0.09	12.77 ± 0.09

^a Velocity interval over which the equivalent width and column density are measured. ^b Rest equivalent width.

Table A16. Ionic column densities for J0255+0048 (15:H3) at $z_{\text{dla}} = 3.2530$

Ion	λ (Å)	$\log f$	Instr.	v_{int}^a (km s $^{-1}$)	W_{λ}^b (mÅ)	$\log N$	$\log N_{\text{adopt}}$
C I	1560.3092	-0.8808	ESI	[−100, 100]	< 34.6	< 13.26	< 13.09
	1656.9283	-0.8273	ESI	[−100, 100]	< 29.0	< 13.09	
C IV	1548.1950	-0.7194	ESI	[−150, 300]	683.9 ± 26.8	14.39 ± 0.02	14.41 ± 0.02
	1550.7700	-1.0213	ESI	[−150, 300]	480.9 ± 27.0	14.46 ± 0.03	
Al II	1670.7874	0.2742	ESI	[−200, 300]	1212.7 ± 22.7	> 13.77	> 13.77
Al III	1854.7164	-0.2684	ESI	[−100, 100]	104.1 ± 16.8	12.86 ± 0.07	12.86 ± 0.07
	1862.7895	-0.5719	ESI	[−100, 100]	75.2 ± 24.9	< 13.01	
Si II	1526.7066	-0.8962	ESI	[−280, 300]	1056.9 ± 27.2	> 14.94	15.31 ± 0.05
	1808.0130	-2.6603	ESI	[−100, 200]	122.4 ± 12.5	15.31 ± 0.04	
Cr II	2056.2539	-0.9788	ESI	[−100, 100]	< 37.5	< 13.14	< 13.14
	2066.1610	-1.2882	ESI	[−100, 100]	< 37.1	< 13.46	
Fe II	1608.4511	-1.2366	ESI	[−280, 300]	561.2 ± 24.2	14.77 ± 0.02	14.77 ± 0.02
Ni II	1741.5531	-1.3696	ESI	[−100, 230]	69.9 ± 23.1	13.82 ± 0.14	13.82 ± 0.14
Zn II	2026.1360	-0.3107	ESI	[−100, 100]	< 41.3	< 12.55	< 12.55

^a Velocity interval over which the equivalent width and column density are measured. ^b Rest equivalent width.

Table A17. Ionic column densities for J0816+4823 (16:H4) at $z_{\text{dla}} = 2.7067$

Ion	λ (Å)	$\log f$	Instr.	v_{int}^a (km s $^{-1}$)	W_{λ}^b (mA)	$\log N$	$\log N_{\text{adopt}}$
C I	1656.9283	-0.8273	ESI	[−100, 100]	< 20.3	< 12.93	< 12.93
O I	1302.1685	-1.3110	ESI	[−60, 60]	236.0 ± 8.5	> 14.70	> 14.70
Al II	1670.7874	0.2742	ESI	[−60, 60]	103.6 ± 7.7	12.44 ± 0.03	12.44 ± 0.03
Si II	1526.7066	-0.8962	ESI	[−60, 60]	133.7 ± 5.0	13.85 ± 0.02	13.85 ± 0.02
	1808.0130	-2.6603	ESI	[−60, 50]	< 17.4	< 14.62	
Mn II	2594.4990	-0.5670	ESI	[−60, 60]	< 53.3	< 12.68	< 12.68
	2606.4620	-0.7151	ESI	[−60, 60]	< 54.0	< 12.82	
Fe II	1611.2005	-2.8665	ESI	[−50, 50]	< 16.3	< 14.88	13.74 ± 0.03
	2249.8768	-2.7397	ESI	[−50, 50]	< 23.1	< 14.64	
	2260.7805	-2.6126	ESI	[−50, 50]	< 21.9	< 14.48	
	2344.2140	-0.9431	ESI	[−60, 50]	178.2 ± 7.9	> 13.63	
	2374.4612	-1.5045	ESI	[−40, 40]	84.5 ± 7.3	13.78 ± 0.04	
	2382.7650	-0.4949	ESI	[−40, 60]	221.3 ± 8.7	> 13.31	
	2586.6500	-1.1605	ESI	[−60, 60]	155.3 ± 25.0	13.65 ± 0.07	
	2600.1729	-0.6216	ESI	[−50, 50]	233.2 ± 22.0	> 13.33	
Ni II	1709.6042	-1.4895	ESI	[−60, 60]	< 16.9	< 13.49	< 13.49
	1751.9157	-1.5575	ESI	[−60, 60]	< 20.4	< 13.62	
Zn II	2026.1360	-0.3107	ESI	[−60, 60]	< 17.3	< 12.16	< 12.16

^a Velocity interval over which the equivalent width and column density are measured. ^b Rest equivalent width.

Table A18. Ionic column densities for J0908+0238 (18:H6) at $z_{\text{dla}} = 2.9586$

Ion	λ (Å)	$\log f$	Instr.	v_{int}^a (km s $^{-1}$)	W_{λ}^b (mÅ)	$\log N$	$\log N_{\text{adopt}}$
C IV							
	1550.7700	-1.0213	MagE	[-70, 70]	< 52.2	< 13.58	< 13.58
Al II	1670.7874	0.2742	MagE	[-100, 100]	637.4 ± 31.3	> 13.46	> 13.47
Al III	1854.7164	-0.2684	MagE	[-100, 100]	< 154.6	< 13.16	< 13.16
	1862.7895	-0.5719	MagE	[-100, 100]	< 90.4	< 13.25	
Si II	1526.7066	-0.8962	MagE	[-100, 100]	533.4 ± 27.6	> 14.65	15.68 ± 0.07
	1808.0130	-2.6603	MagE	[-100, 100]	234.1 ± 37.1	15.68 ± 0.07	
Cr II	2056.2539	-0.9788	MagE	[-100, 100]	< 167.5	< 13.92	< 13.92
Fe II	1608.4511	-1.2366	MagE	[-100, 100]	601.1 ± 96.3	> 14.95	> 14.95
	1611.2005	-2.8665	MagE	[-100, 100]	< 83.1	< 15.62	
Zn II	2026.1360	-0.3107	MagE	[-100, 100]	298.6 ± 65.7	< 13.32	< 13.32

^a Velocity interval over which the equivalent width and column density are measured. ^b Rest equivalent width.

Table A19. Ionic column densities for J0844+1245 (21:H9) at $z_{\text{dla}} = 1.8639$

Ion	λ (Å)	$\log f$	Instr.	v_{int}^a (km s $^{-1}$)	W_{λ}^b (mA)	$\log N$	$\log N_{\text{adopt}}$
C IV	1548.1950	-0.7194	ESI	[−200, 100]	262.8 ± 14.3	13.90 ± 0.02	13.91 ± 0.02
	1550.7700	-1.0213	ESI	[−200, 100]	161.3 ± 14.7	13.96 ± 0.04	
Mg II	2796.3520	-0.2130	ESI	[−100, 100]	484.0 ± 13.5	> 13.33	> 13.58
	2803.5310	-0.5151	ESI	[−100, 100]	452.0 ± 16.0	> 13.58	
Al III	1854.7164	-0.2684	ESI	[−100, 100]	96.2 ± 11.2	12.82 ± 0.05	12.83 ± 0.04
	1862.7895	-0.5719	ESI	[−100, 100]	54.4 ± 11.3	12.85 ± 0.09	
Si II	1526.7066	-0.8962	ESI	[−100, 100]	202.7 ± 12.4	> 14.05	14.97 ± 0.06
	1808.0130	-2.6603	ESI	[−50, 50]	54.1 ± 7.7	14.97 ± 0.06	
Cr II	2066.1610	-1.2882	ESI	[−100, 100]	< 24.9	< 13.29	< 13.29
	2576.8770	-0.4549	ESI	[−50, 50]	46.8 ± 10.5	12.38 ± 0.10	12.38 ± 0.10
Mn II	2594.4990	-0.5670	ESI	[−100, 100]	85.7 ± 14.0	< 12.75	
	1608.4511	-1.2366	ESI	[−100, 100]	174.0 ± 13.9	> 14.24	14.79 ± 0.06
Fe II	1611.2005	-2.8665	ESI	[−100, 100]	< 28.6	< 15.15	
	2249.8768	-2.7397	ESI	[−50, 50]	41.6 ± 8.7	14.74 ± 0.09	
Ni II	2260.7805	-2.6126	ESI	[−100, 100]	71.0 ± 12.3	14.84 ± 0.07	
	2344.2140	-0.9431	ESI	[−100, 100]	295.8 ± 11.0	> 13.90	
Zn II	2374.4612	-1.5045	ESI	[−100, 100]	223.0 ± 11.1	> 14.29	
	2382.7650	-0.4949	ESI	[−100, 100]	332.8 ± 10.8	> 13.54	
Zn II	2586.6500	-1.1605	ESI	[−100, 100]	388.2 ± 13.0	> 14.14	
	2600.1729	-0.6216	ESI	[−100, 100]	356.8 ± 12.6	> 13.60	
Ni II	1741.5531	-1.3696	ESI	[−100, 100]	< 26.0	13.55 ± 0.14	13.55 ± 0.14
	2026.1360	-0.3107	ESI	[−50, 50]	31.0 ± 8.4	12.26 ± 0.12	12.26 ± 0.12

^a Velocity interval over which the equivalent width and column density are measured. ^b Rest equivalent width.

Table A20. Ionic column densities for J0751+4516 (22:H10) at $z_{\text{dla}} = 2.6826$

Ion	λ (Å)	$\log f$	Instr.	v_{int}^a (km s $^{-1}$)	W_{λ}^b (mÅ)	$\log N$	$\log N_{\text{adopt}}$
C I	1560.3092	-0.8808	ESI	[−100, 100]	< 32.4	< 13.23	< 12.99
	1656.9283	-0.8273	ESI	[−100, 100]	< 23.3	< 12.99	
C IV	1548.1950	-0.7194	ESI	[−50, 70]	99.7 ± 10.5	13.45 ± 0.05	13.44 ± 0.04
	1550.7700	-1.0213	ESI	[−50, 70]	44.0 ± 11.0	13.37 ± 0.11	
O I	1302.1685	-1.3110	ESI	[−40, 30]	236.2 ± 8.2	> 14.81	> 14.81
Al II	1670.7874	0.2742	ESI	[−70, 60]	169.9 ± 10.3	> 12.72	> 12.72
Al III	1854.7164	-0.2684	ESI	[−50, 40]	36.9 ± 10.2	12.38 ± 0.12	12.38 ± 0.12
	1862.7895	-0.5719	ESI	[−50, 40]	< 18.4	< 12.53	
Si II	1304.3702	-1.0269	ESI	[−60, 50]	246.8 ± 11.5	> 14.42	14.85 ± 0.09
	1526.7066	-0.8962	ESI	[−60, 50]	152.9 ± 9.6	> 13.98	
Si IV	1808.0130	-2.6603	ESI	[−60, 50]	42.2 ± 8.6	14.85 ± 0.09	
	1393.7550	-0.2774	ESI	[−40, 40]	123.0 ± 7.8	13.23 ± 0.03	13.23 ± 0.03
Cr II	2056.2539	-0.9788	ESI	[−50, 50]	< 24.0	< 12.97	< 12.97
Fe II	1608.4511	-1.2366	ESI	[−50, 50]	135.2 ± 12.1	14.14 ± 0.04	14.15 ± 0.03
	1611.2005	-2.8665	ESI	[−50, 50]	< 25.2	< 15.06	
	2249.8768	-2.7397	ESI	[−50, 50]	< 39.5	< 14.91	
	2260.7805	-2.6126	ESI	[−50, 50]	< 27.2	< 14.58	
	2344.2140	-0.9431	ESI	[−60, 50]	261.8 ± 17.3	> 13.88	
	2374.4612	-1.5045	ESI	[−60, 50]	174.0 ± 14.0	14.15 ± 0.04	
	2382.7650	-0.4949	ESI	[−60, 50]	285.9 ± 13.6	> 13.47	
Ni II	2600.1729	-0.6216	ESI	[−60, 50]	244.8 ± 40.6	> 13.57	
	1454.8420	-1.4908	ESI	[−50, 50]	< 12.6	< 13.49	< 13.49
	1709.6042	-1.4895	ESI	[−50, 50]	< 22.5	< 13.63	
	1741.5531	-1.3696	ESI	[−50, 50]	< 25.9	< 13.55	
Zn II	1751.9157	-1.5575	ESI	[−50, 50]	< 26.3	< 13.73	
	2026.1360	-0.3107	ESI	[−50, 50]	< 24.8	< 12.33	< 12.32

^a Velocity interval over which the equivalent width and column density are measured. ^b Rest equivalent width.

Table A21. Ionic column densities for J0818+0720 (23:H11) at $z_{\text{dla}} = 3.2332$

Ion	λ (Å)	$\log f$	Instr.	v_{int}^a (km s $^{-1}$)	W_{λ}^b (mÅ)	$\log N$	$\log N_{\text{adopt}}$
C I	1560.3092	-0.8808	ESI	[−200, 300]	< 48.8	< 13.41	< 13.26
	1656.9283	-0.8273	ESI	[−200, 300]	< 43.8	< 13.26	
C II	1334.5323	-0.8935	ESI	[−250, 300]	2192.2 ± 14.6	> 15.47	> 15.47
	1548.1950	-0.7194	ESI	[−160, 320]	749.9 ± 19.1	> 14.57	> 14.82
C IV	1550.7700	-1.0213	ESI	[−160, 320]	657.9 ± 21.6	> 14.82	
	1670.7874	0.2742	ESI	[−200, 320]	1178.8 ± 19.7	> 13.69	> 13.69
Si II	1260.4221	0.0030	ESI	[−100, 320]	1423.2 ± 12.4	> 14.41	> 14.99
	1526.7066	-0.8962	ESI	[−200, 320]	1214.6 ± 14.4	> 14.99	
Cr II	2056.2539	-0.9788	ESI	[−200, 300]	< 55.0	< 13.33	< 13.33
	2062.2340	-1.1079	ESI	[−200, 300]	99.5 ± 26.0	< 13.59	
	2066.1610	-1.2882	ESI	[−200, 300]	< 53.4	< 13.62	
Fe II	1608.4511	-1.2366	ESI	[−200, 320]	598.1 ± 18.7	> 14.82	> 15.20
	1611.2005	-2.8665	ESI	[−100, 100]	< 25.1	< 15.09	
	2249.8768	-2.7397	ESI	[−200, 300]	< 315.7	< 15.61	
	2374.4612	-1.5045	ESI	[−150, 150]	1023.0 ± 116.1	> 15.20	
Ni II	1709.6042	-1.4895	ESI	[−150, 280]	96.6 ± 23.3	14.09 ± 0.10	14.09 ± 0.07
	1741.5531	-1.3696	ESI	[−150, 220]	123.6 ± 30.2	14.08 ± 0.10	
Zn II	2026.1360	-0.3107	ESI	[−180, 300]	< 49.3	< 12.62	< 12.62

^a Velocity interval over which the equivalent width and column density are measured. ^b Rest equivalent width.

Table A22. Ionic column densities for J0818+2631 (24:H12) at $z_{\text{dla}} = 3.5629$

Ion	λ (Å)	$\log f$	Instr.	v_{int}^a (km s $^{-1}$)	W_{λ}^b (mÅ)	$\log N$	$\log N_{\text{adopt}}$
C I	1560.3092	-0.8808	ESI	[−200, 300]	93.3 ± 11.8	13.55 ± 0.05	13.55 ± 0.05
	1656.9283	-0.8273	ESI	[−200, 300]	< 26.4	< 13.03	
C II	1334.5323	-0.8935	ESI	[−250, 300]	1759.4 ± 8.1	> 15.35	> 15.35
	1548.1950	-0.7194	ESI	[−160, 320]	529.7 ± 11.0	14.25 ± 0.01	14.26 ± 0.01
C IV	1550.7700	-1.0213	ESI	[−160, 320]	329.8 ± 11.4	14.28 ± 0.02	
	1670.7874	0.2742	ESI	[−200, 320]	1577.5 ± 10.7	> 13.88	> 13.88
Al II	1526.7066	-0.8962	ESI	[−200, 320]	1170.6 ± 9.9	> 14.99	> 14.99
	1393.7550	-0.2774	ESI	[−100, 230]	601.3 ± 6.8	> 14.02	> 14.02
Fe II	1608.4511	-1.2366	ESI	[−200, 320]	684.5 ± 16.2	> 14.97	> 14.97
	1611.2005	-2.8665	ESI	[−200, 300]	78.5 ± 14.9	< 15.42	
Ni II	1709.6042	-1.4895	ESI	[−150, 280]	55.3 ± 11.0	13.85 ± 0.08	13.85 ± 0.05
	1741.5531	-1.3696	ESI	[−150, 220]	77.6 ± 10.4	13.86 ± 0.06	
Zn II	2026.1360	-0.3107	ESI	[−180, 300]	< 47.5	< 12.60	< 12.60

^a Velocity interval over which the equivalent width and column density are measured. ^b Rest equivalent width.

Table A23. Ionic column densities for J0811+3936 (25:H13) at $z_{\text{dla}} = 2.6500$

Ion	λ (Å)	$\log f$	Instr.	v_{int}^a (km s $^{-1}$)	W_{λ}^b (mÅ)	$\log N$	$\log N_{\text{adopt}}$
C I	1560.3092	-0.8808	ESI	[−100, 200]	< 27.0	< 13.15	< 13.15
	1656.9283	-0.8273	ESI	[−100, 200]	< 36.4	< 13.18	
C II	1334.5323	-0.8935	ESI	[−100, 300]	1074.3 ± 25.2	> 15.11	> 15.11
	1548.1950	-0.7194	ESI	[−100, 250]	553.1 ± 13.7	> 14.43	> 14.51
C IV	1550.7700	-1.0213	ESI	[−100, 250]	428.6 ± 13.7	> 14.51	
	1302.1685	-1.3110	ESI	[−100, 300]	1118.4 ± 15.8	> 15.53	> 15.53
O I	1670.7874	0.2742	ESI	[−100, 300]	807.6 ± 17.2	> 13.41	> 13.41
	1854.7164	-0.2684	ESI	[−100, 300]	132.4 ± 19.7	12.95 ± 0.06	12.98 ± 0.05
Al II	1862.7895	-0.5719	ESI	[−100, 300]	98.0 ± 19.7	13.10 ± 0.09	
	1190.4158	-0.6017	ESI	[−200, 200]	728.5 ± 29.2	> 14.68	> 14.68
Al III	1260.4221	0.0030	ESI	[−100, 300]	1392.0 ± 24.3	> 14.39	
	1526.7066	-0.8962	ESI	[−100, 300]	803.6 ± 17.5	> 14.68	
Si II	1808.0130	-2.6603	ESI	[−40, 100]	< 29.6	< 14.86	
	1393.7550	-0.2774	ESI	[−120, 200]	434.4 ± 12.6	> 13.87	13.95 ± 0.02
Si IV	1402.7700	-0.5817	ESI	[−120, 200]	295.7 ± 14.3	13.95 ± 0.02	
	2056.2539	-0.9788	ESI	[−100, 200]	< 39.7	< 13.19	< 13.19
Cr II	2062.2340	-1.1079	ESI	[−100, 200]	< 54.5	< 13.45	
	2066.1610	-1.2882	ESI	[−100, 200]	< 39.1	< 13.48	
Fe II	1608.4511	-1.2366	ESI	[−120, 280]	304.1 ± 23.6	14.42 ± 0.03	14.45 ± 0.03
	1611.2005	-2.8665	ESI	[−100, 200]	< 42.0	< 15.31	
	2260.7805	-2.6126	ESI	[−100, 250]	< 73.5	< 15.01	
	2344.2140	-0.9431	ESI	[−100, 300]	865.2 ± 27.6	> 14.33	
	2374.4612	-1.5045	ESI	[−60, 250]	414.7 ± 39.6	14.50 ± 0.04	
	2382.7650	-0.4949	ESI	[−100, 300]	1268.8 ± 31.7	> 14.14	
Ni II	1709.6042	-1.4895	ESI	[−100, 200]	< 28.4	< 13.71	< 13.62
	1741.5531	-1.3696	ESI	[−100, 200]	< 31.8	< 13.62	
	1751.9157	-1.5575	ESI	[−100, 200]	< 35.1	< 13.85	
Zn II	2026.1360	-0.3107	ESI	[−100, 200]	< 52.7	< 12.66	< 12.66

^a Velocity interval over which the equivalent width and column density are measured. ^b Rest equivalent width.

Table A24. Ionic column densities for J1320+1310 (32:H20) at $z_{\text{dla}} = 2.6722$

Ion	λ (Å)	$\log f$	Instr.	v_{int}^a (km s $^{-1}$)	W_{λ}^b (mÅ)	$\log N$	$\log N_{\text{adopt}}$
C IV	1548.1950	-0.7194	X-shooter	[−100, 100]	< 56.6	< 13.33	< 13.32
	1550.7700	-1.0213	X-shooter	[−100, 100]	< 58.2	< 13.66	
Al II	1670.7874	0.2742	X-shooter	[−50, 50]	< 39.0	< 12.15	< 12.15
	1854.7164	-0.2684	X-shooter	[−50, 50]	< 26.4	< 12.36	< 12.36
Al III	1862.7895	-0.5719	X-shooter	[−50, 50]	< 29.9	< 12.77	
	1260.4221	0.0030	X-shooter	[−100, 100]	313.2 ± 11.2	13.51 ± 0.02	13.51 ± 0.02
Si II	1526.7066	-0.8962	X-shooter	[−100, 100]	125.9 ± 38.7	< 13.86	
	1808.0130	-2.6603	X-shooter	[−50, 50]	< 26.0	< 14.77	
	1259.5190	-1.7894	X-shooter	[−50, 50]	64.4 ± 8.5	< 14.49	< 14.49
Cr II	2056.2539	-0.9788	X-shooter	[−50, 50]	< 31.1	< 13.08	< 13.08
Fe II	1608.4511	-1.2366	X-shooter	[−100, 100]	< 76.2	< 14.03	12.94 ± 0.09
	2249.8768	-2.7397	X-shooter	[−50, 50]	< 26.5	< 14.68	
	2260.7805	-2.6126	X-shooter	[−50, 50]	< 36.7	< 14.70	
	2344.2140	-0.9431	X-shooter	[−70, 70]	< 37.7	< 13.04	
	2382.7650	-0.4949	X-shooter	[−70, 70]	116.1 ± 24.8	12.94 ± 0.09	
Ni II	1741.5531	-1.3696	X-shooter	[−50, 50]	< 40.1	< 13.72	< 13.72
Zn II	2026.1360	-0.3107	X-shooter	[−50, 50]	< 33.6	< 12.47	< 12.47

^a Velocity interval over which the equivalent width and column density are measured. ^b Rest equivalent width.

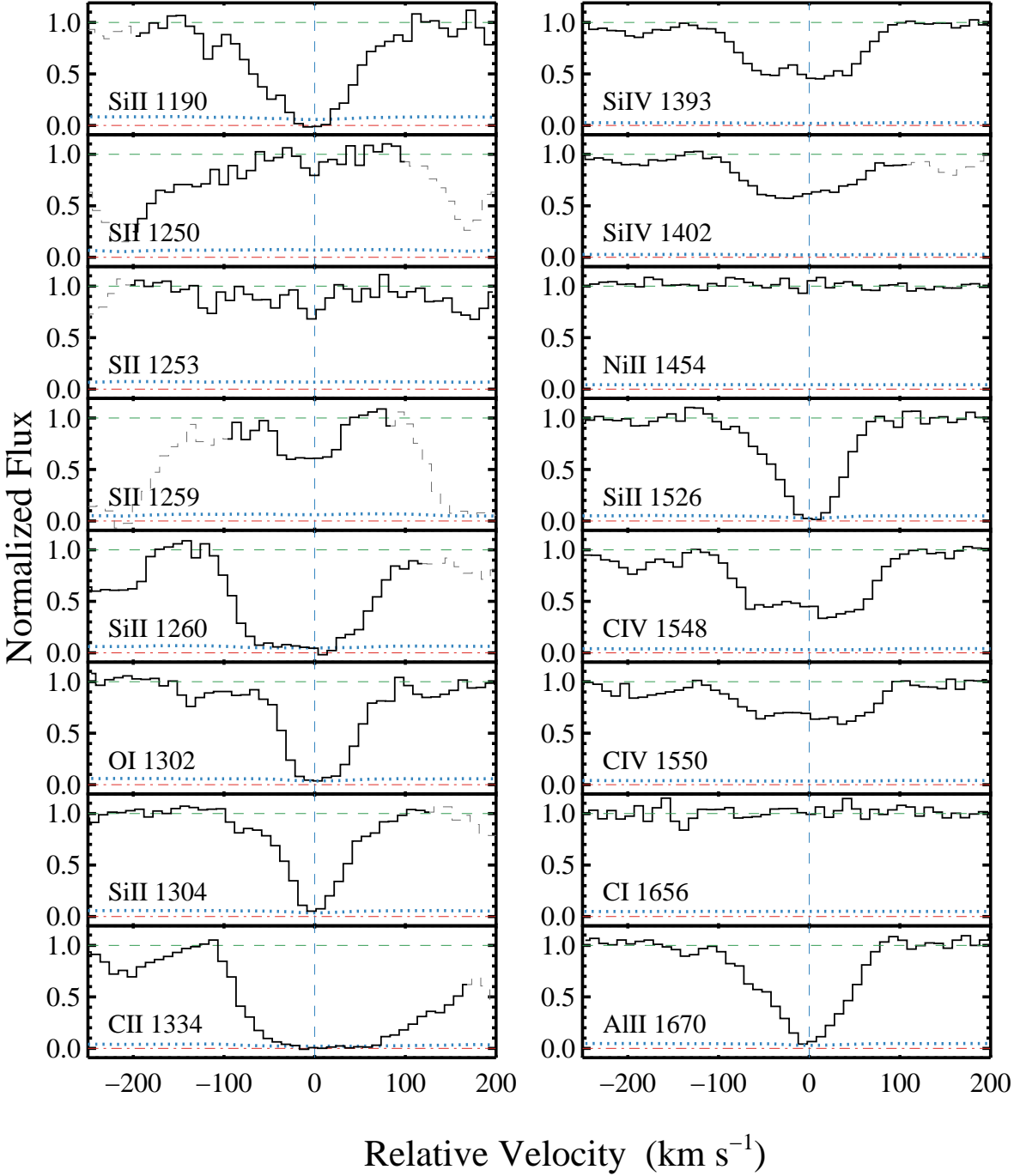


Figure A1. Velocity plot of the ion transitions associated to the DLA J2114-0055 (1:G1) at $z_{\text{dla}} = 2.9181$. Data are shown as black histograms, with grey dashed lines highlighting regions affected by unrelated absorption. The normalized continuum levels are marked by a green dashed line, while the red dash-dotted lines mark the zero level. The adopted systemic velocities are indicated by vertical blue dashed lines. Errors on the flux are shown with dotted blue lines.

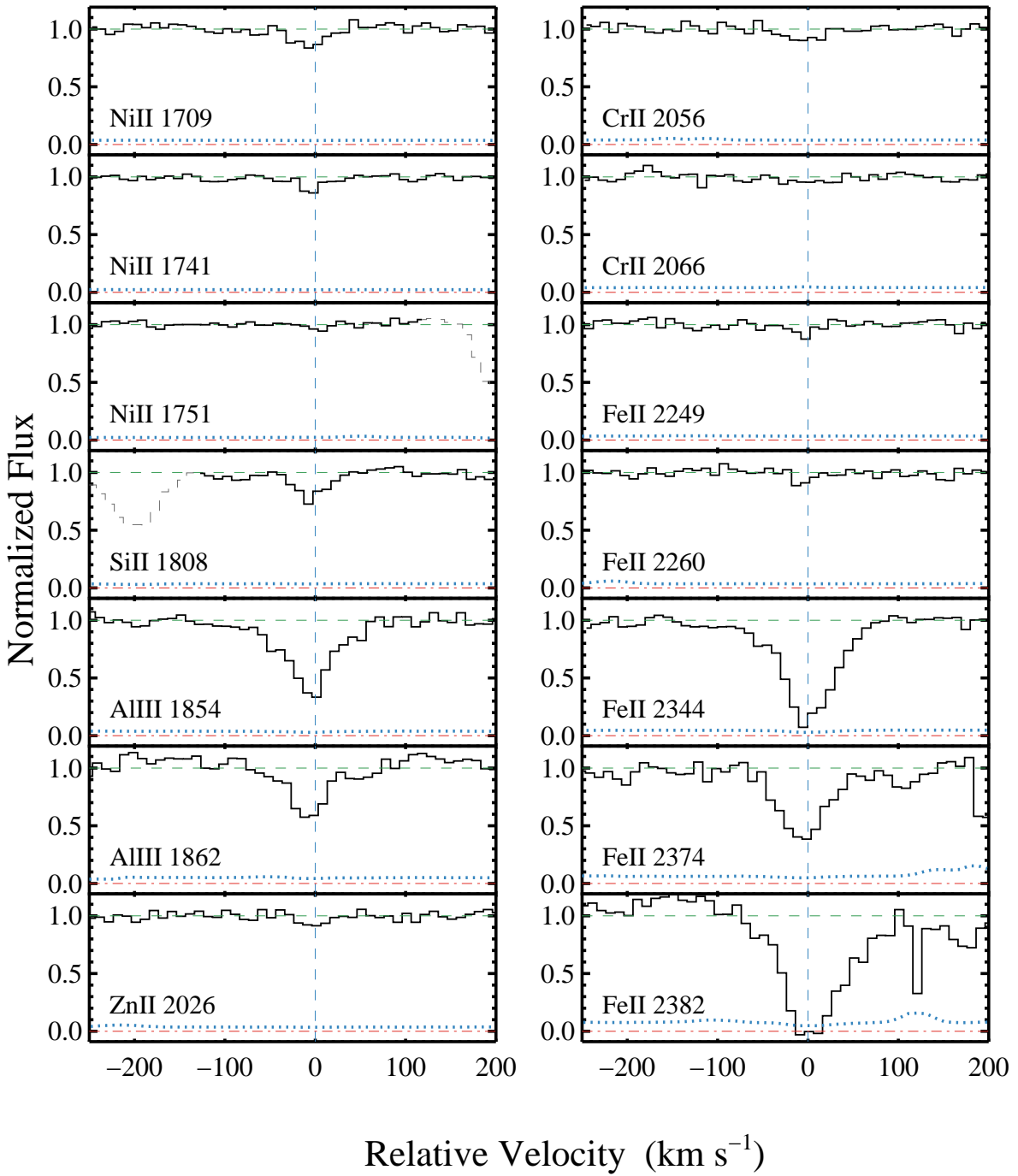


Figure A2. Velocity plot of the ion transitions associated to the DLA J2114-0055 (1:G1) at $z_{\text{dla}} = 2.9181$ (continued). See Figure A1 for an explanation of the different line colors.

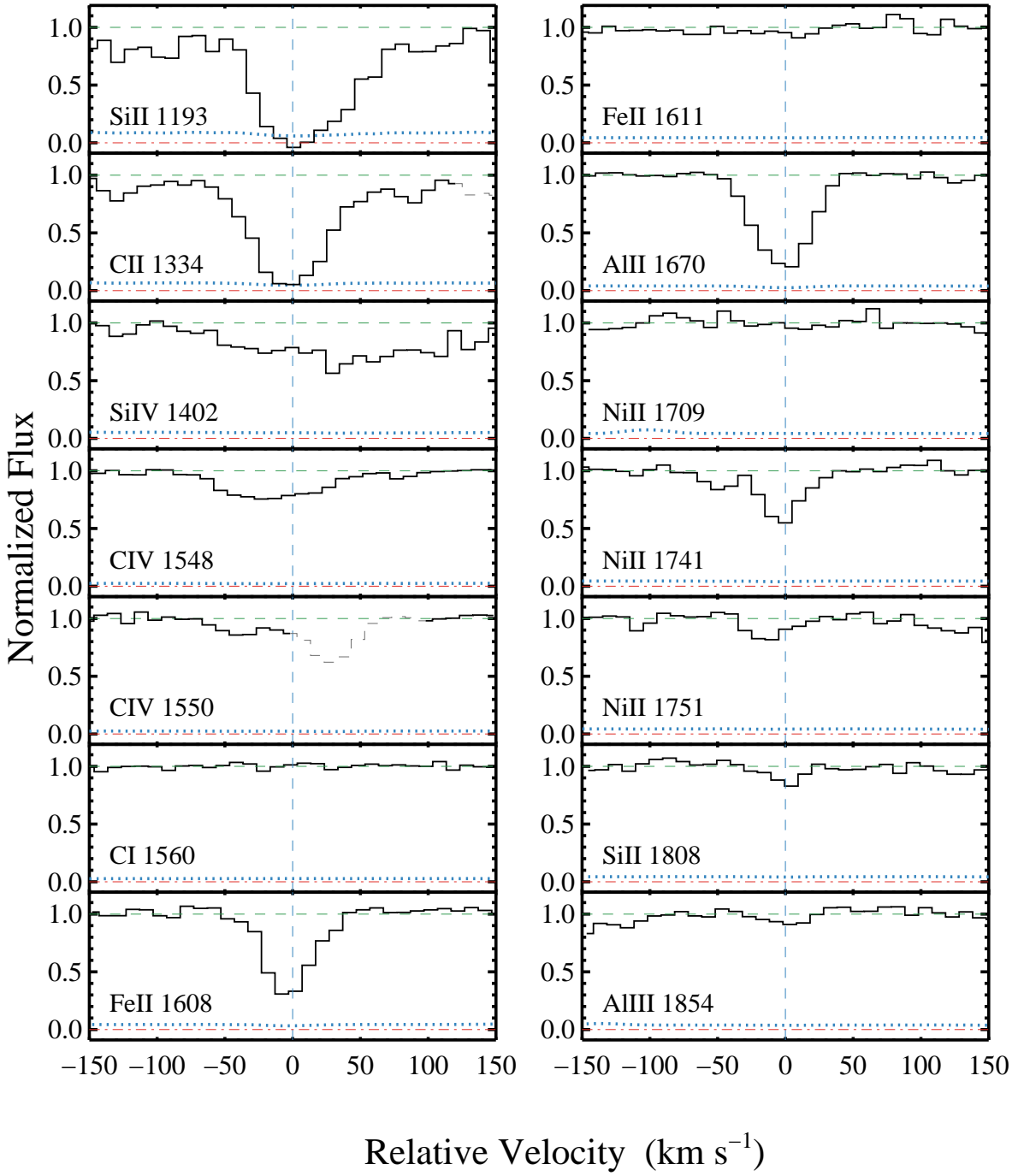


Figure A3. Velocity plot of the ion transitions associated to the DLA J0731+2854 (2:G2) at $z_{\text{dla}} = 2.6878$. See Figure A1 for an explanation of the different line colors.

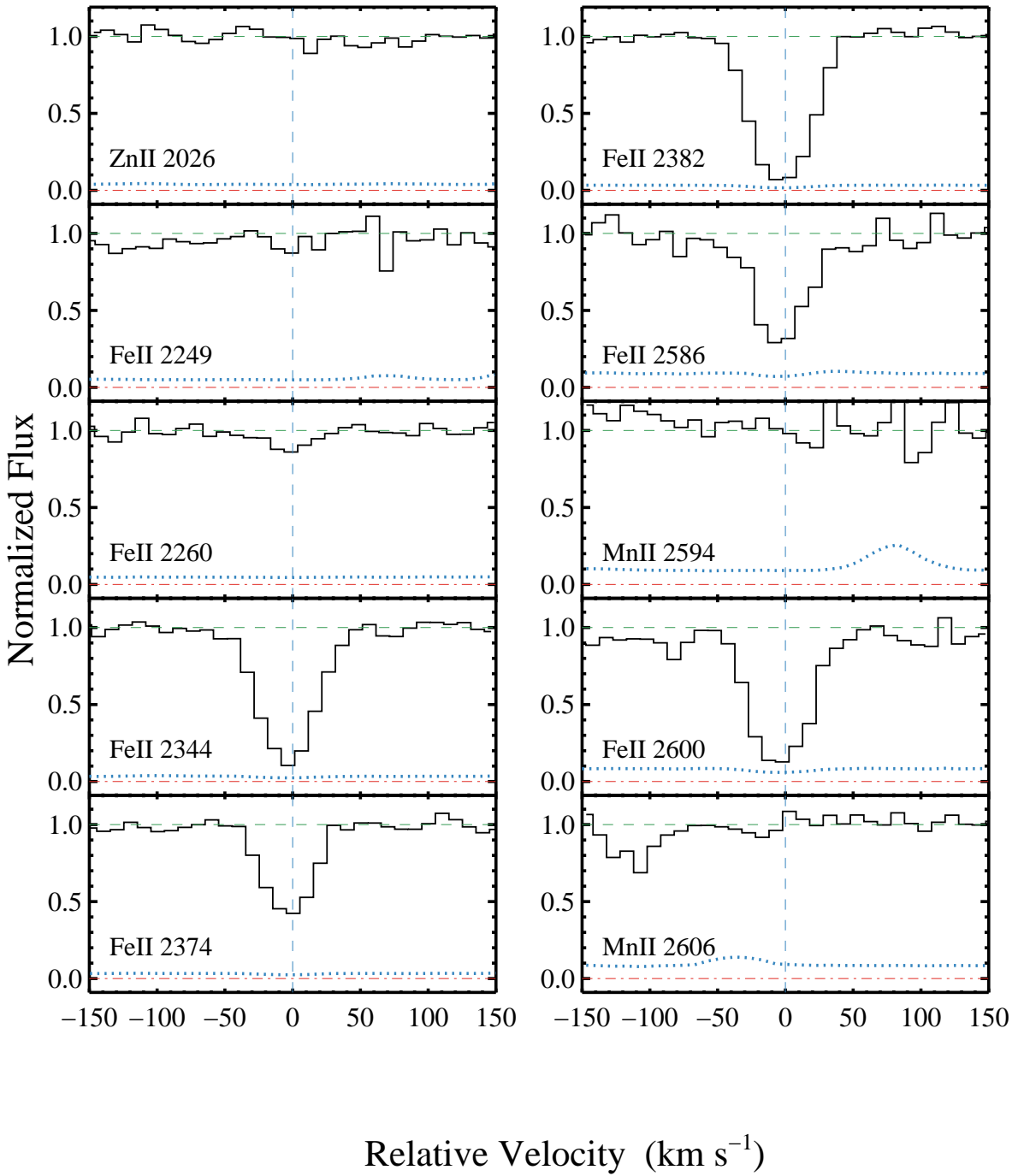


Figure A4. Velocity plot of the ion transitions associated to the DLA J0731+2854 (2:G2) at $z_{\text{dla}} = 2.6878$ (continued). See Figure A1 for an explanation of the different line colors.

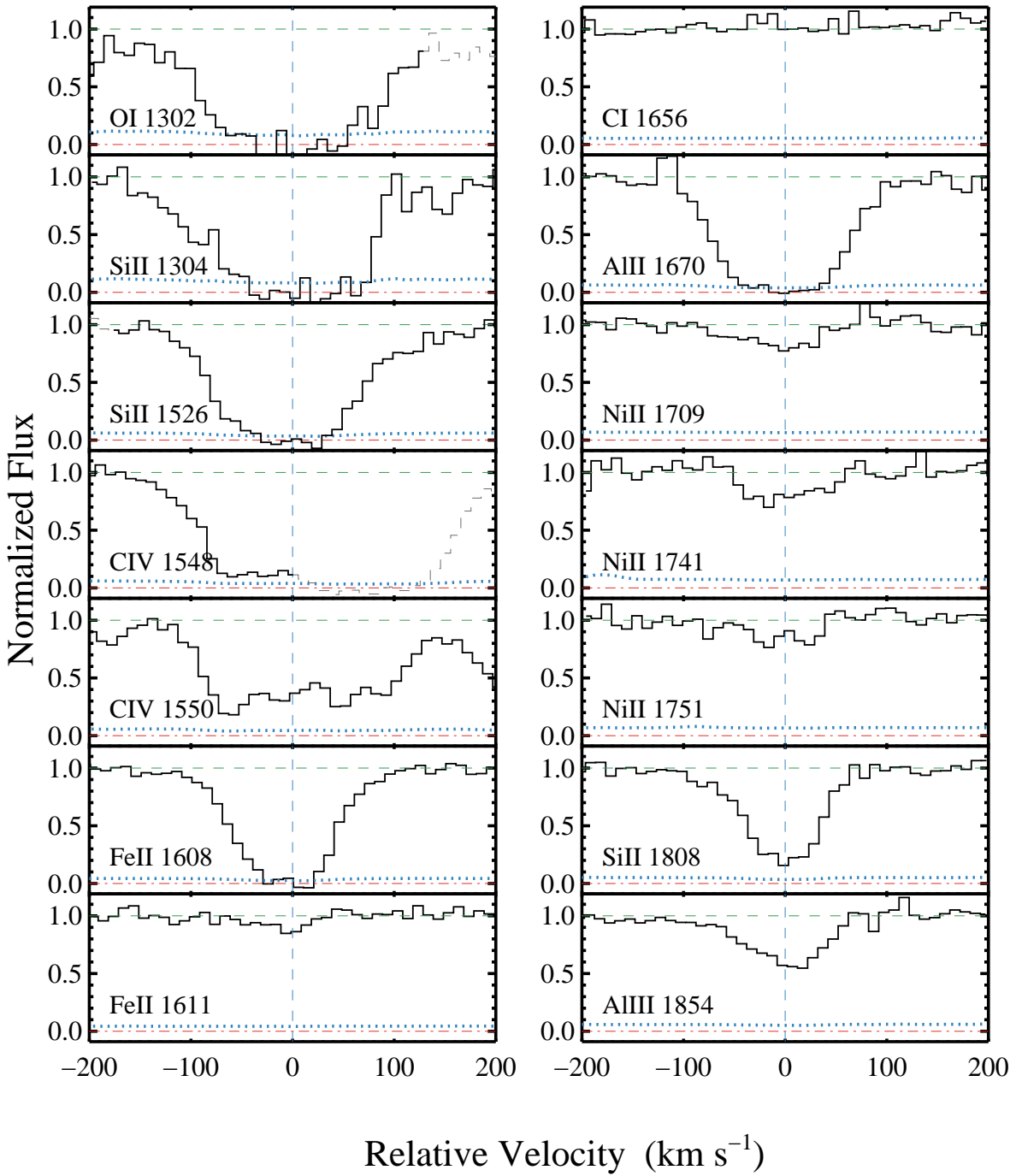


Figure A5. Velocity plot of the ion transitions associated to the DLA J0956+3444 (3:G3) at $z_{\text{dla}} = 2.3887$. See Figure A1 for an explanation of the different line colors. The Si II 1808 transition is blended with Si IV 1393 from the higher redshift LLS and it is excluded from the analysis.

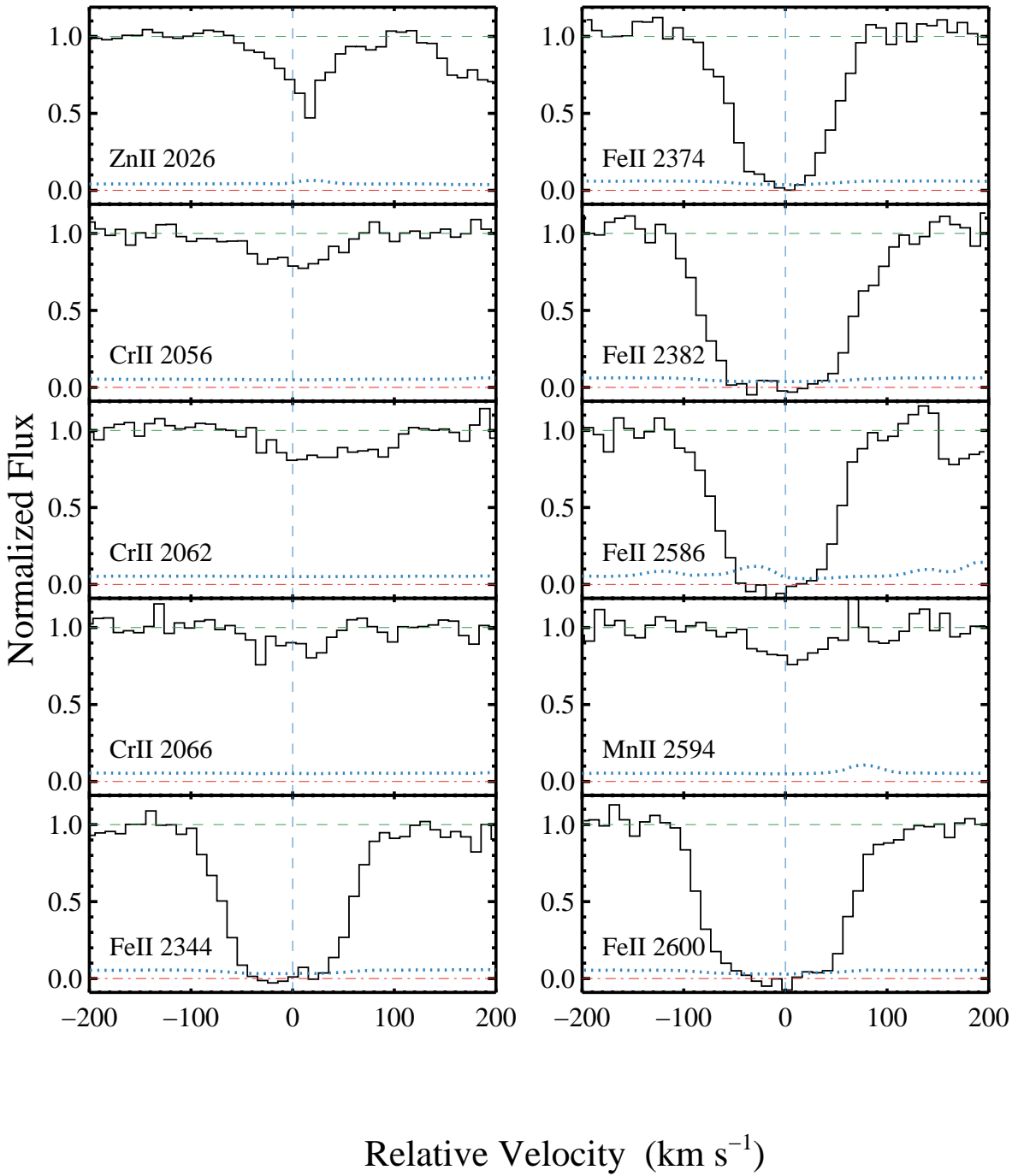


Figure A6. Velocity plot of the ion transitions associated to the DLA J0956+3444 (3:G3) at $z_{\text{dla}} = 2.3887$ (continued). See Figure A1 for an explanation of the different line colors.

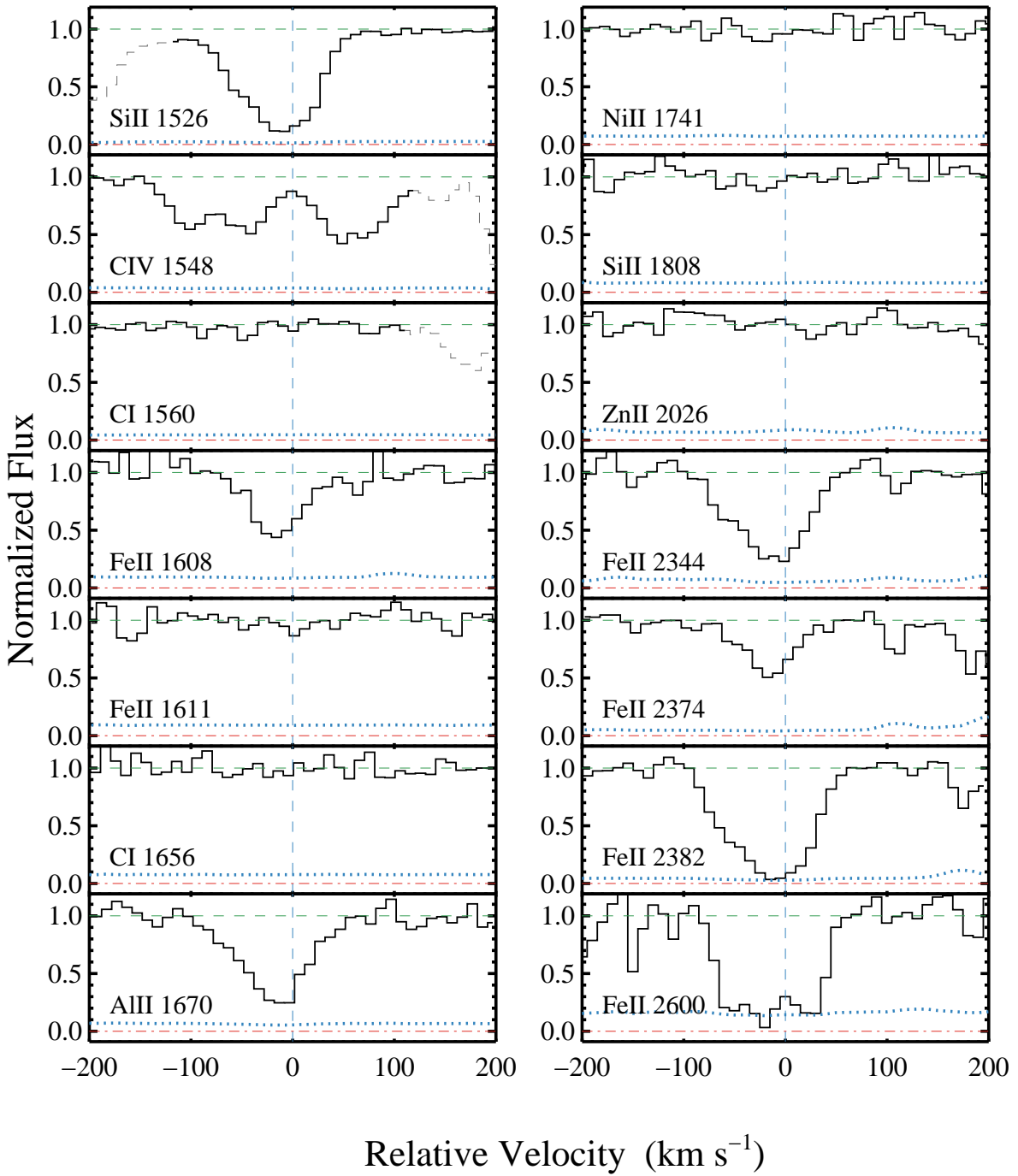


Figure A7. Velocity plot of the ion transitions associated to the DLA J2343-1047 (4:G4) at $z_{\text{dla}} = 2.6880$. See Figure A1 for an explanation of the different line colors.

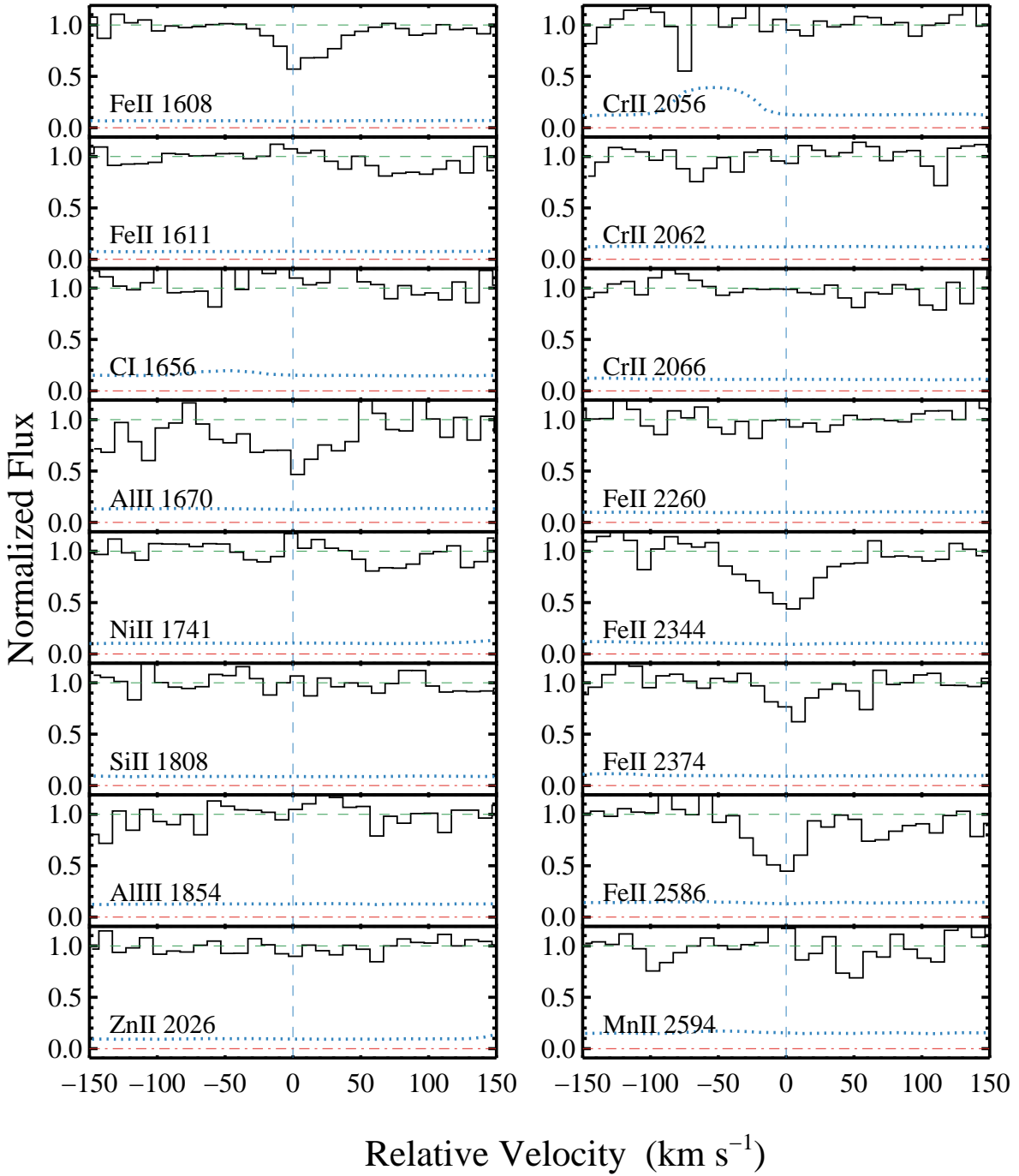


Figure A8. Velocity plot of the ion transitions associated to the DLA J0343-0622 (5:G5) at $z_{\text{dla}} = 2.5713$. See Figure A1 for an explanation of the different line colors.

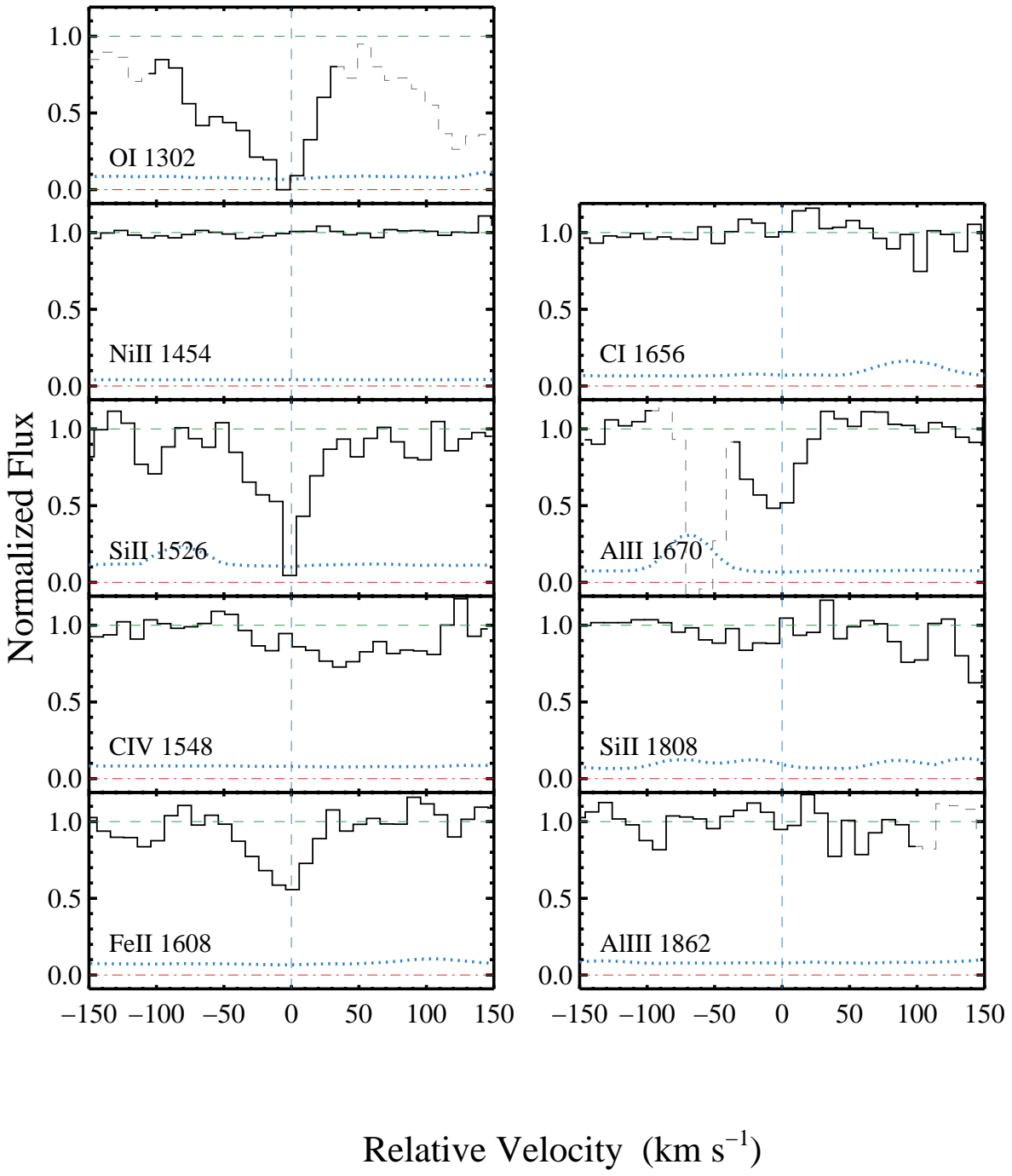


Figure A9. Velocity plot of the ion transitions associated to the DLA J2351+1600 (6:G6) at $z_{\text{dla}} = 3.7861$. See Figure A1 for an explanation of the different line colors.

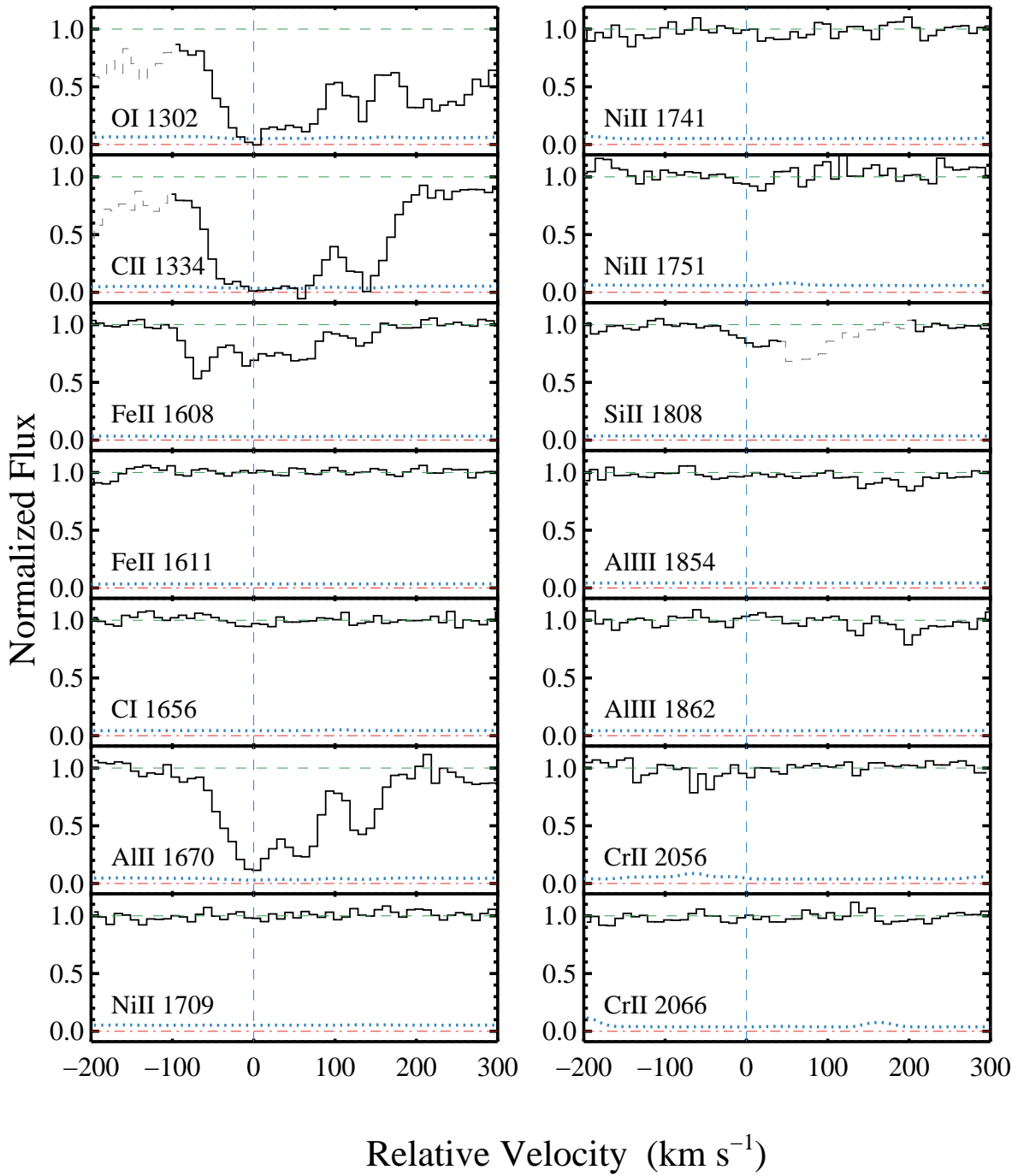


Figure A10. Velocity plot of the ion transitions associated to the DLA J0042-1020 (7:G7) at $z_{\text{dla}} = 2.7544$. See Figure A1 for an explanation of the different line colors.

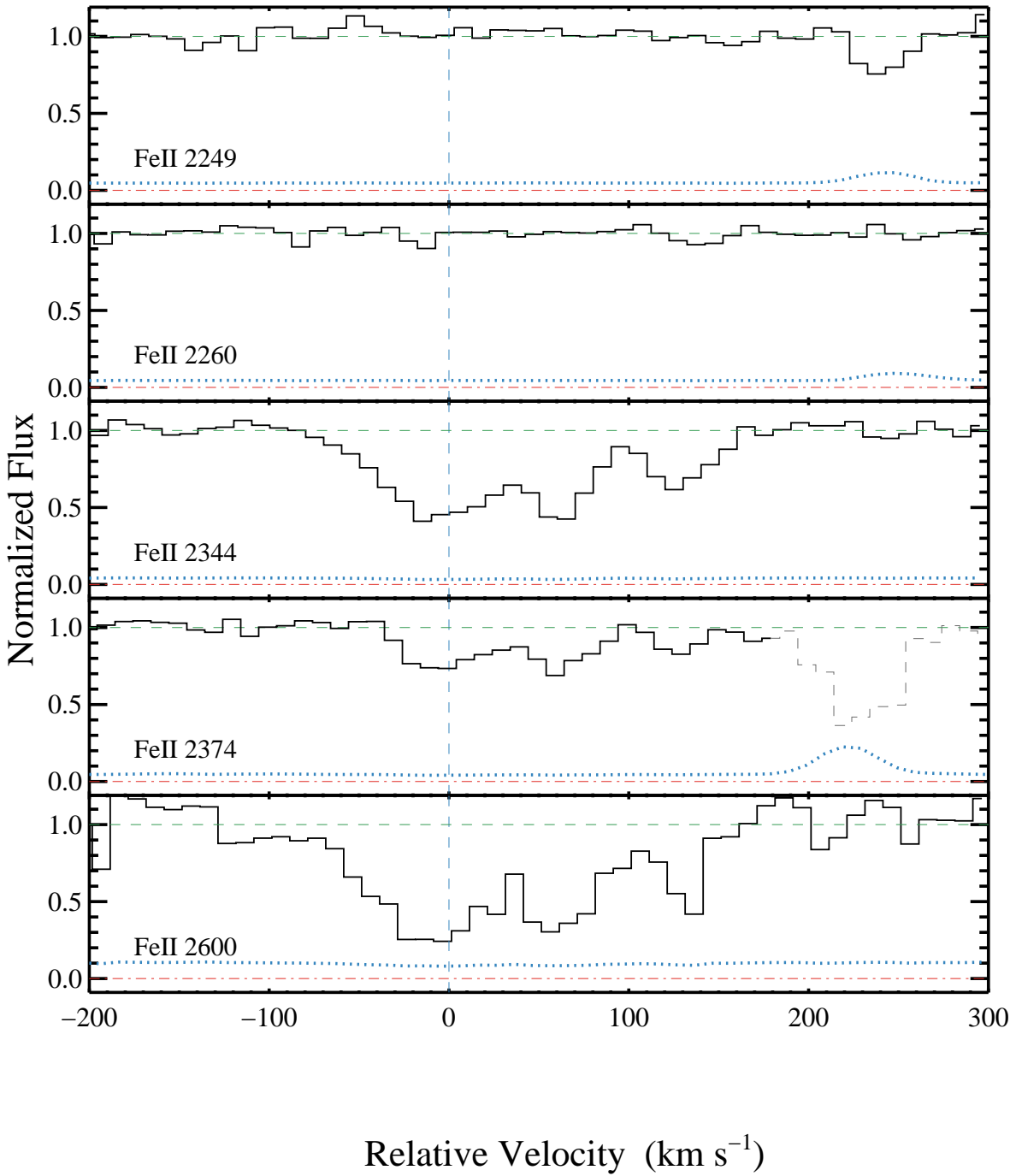


Figure A11. Velocity plot of the ion transitions associated to the DLA J0042-1020 (7:G7) at $z_{\text{dla}} = 2.7544$ (continued). See Figure A1 for an explanation of the different line colors.

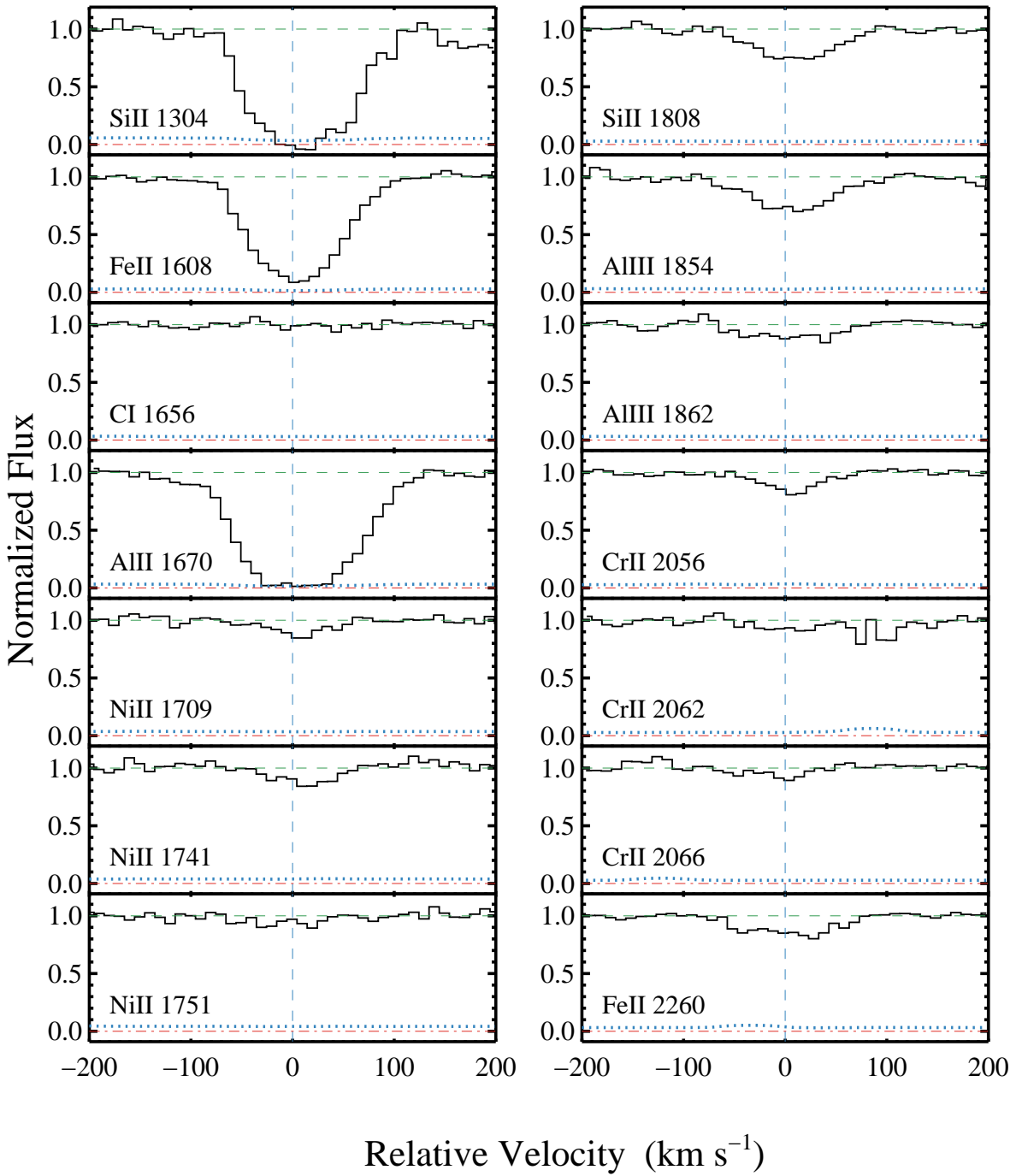


Figure A12. Velocity plot of the ion transitions associated to the DLA J0949+1115 (8:G9) at $z_{\text{dla}} = 2.7584$. See Figure A1 for an explanation of the different line colors.

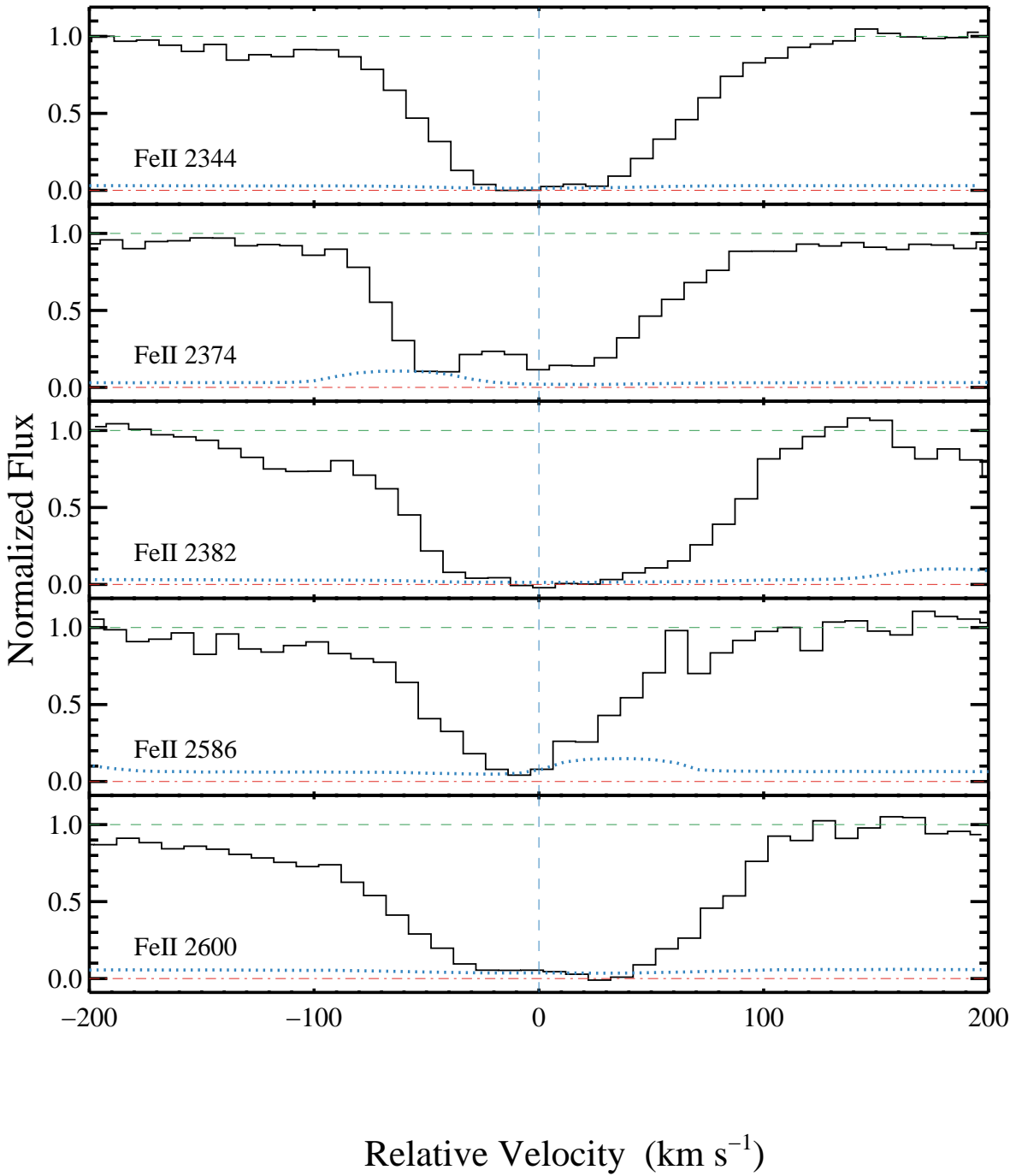


Figure A13. Velocity plot of the ion transitions associated to the DLA J0949+1115 (8:G9) at $z_{\text{dla}} = 2.7584$ (continued). See Figure A1 for an explanation of the different line colors.

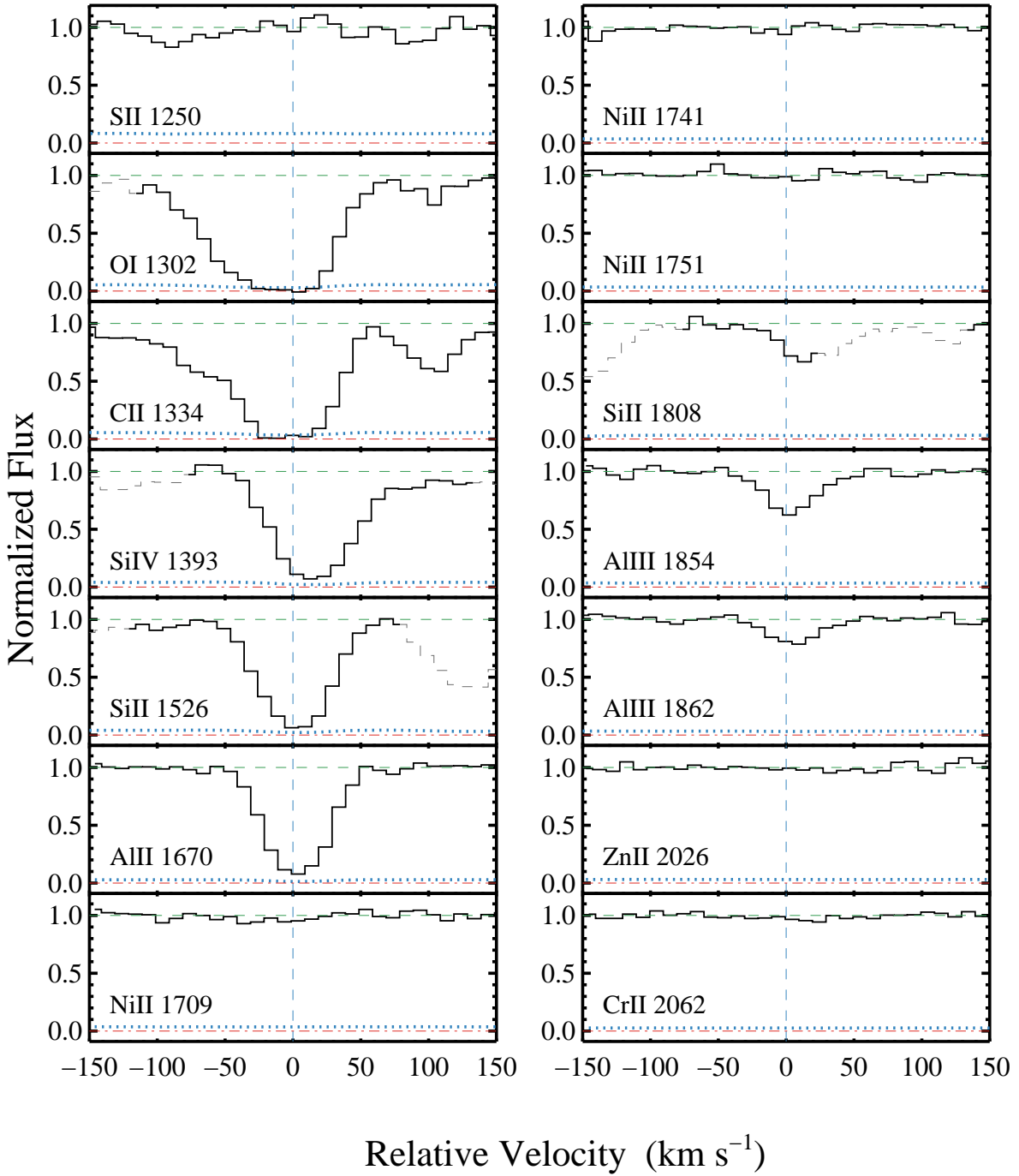


Figure A14. Velocity plot of the ion transitions associated to the DLA J1018+3106 (9:G10) at $z_{\text{dla}} = 2.4592$. See Figure A1 for an explanation of the different line colors.

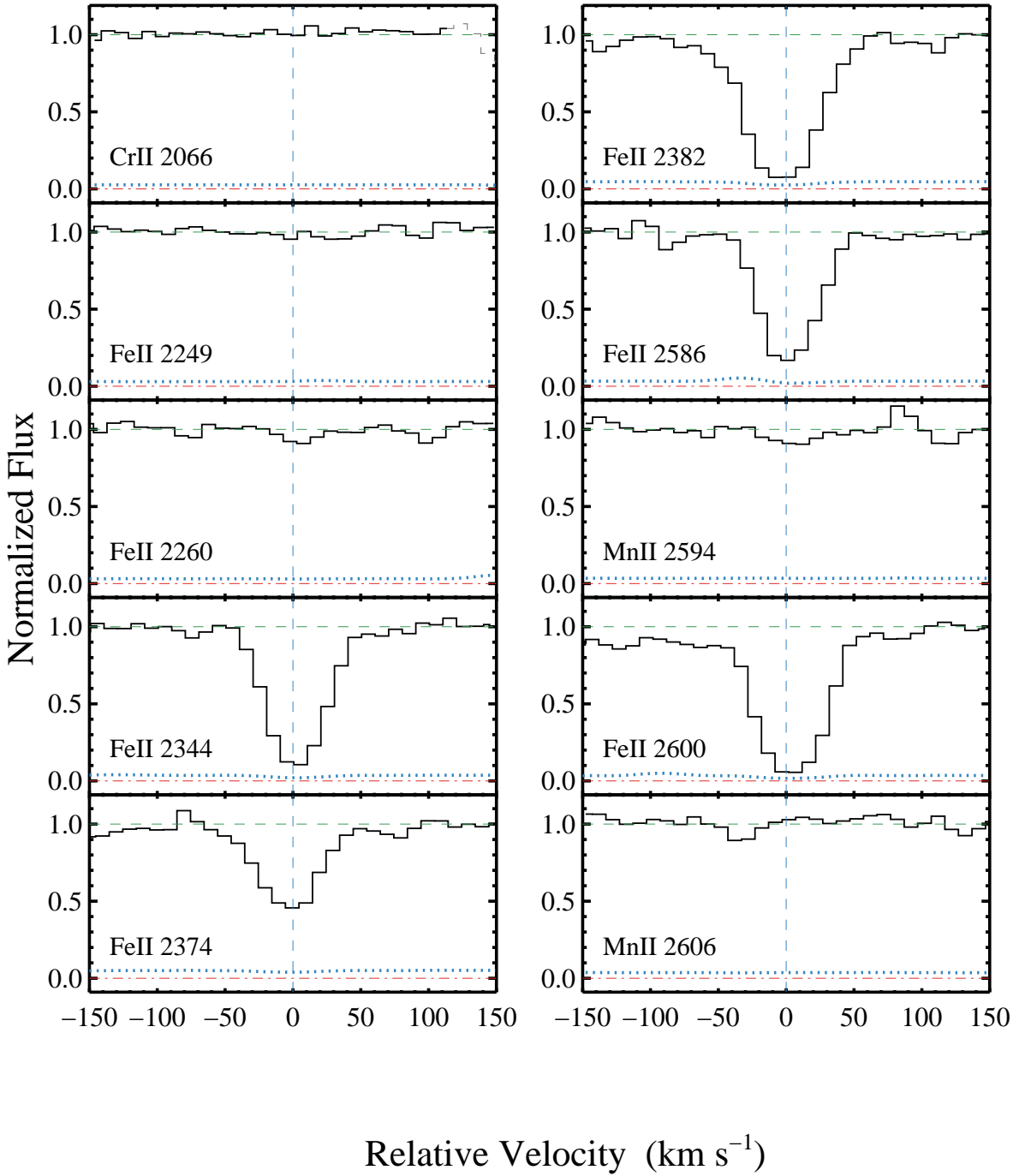


Figure A15. Velocity plot of the ion transitions associated to the DLA J1018+3106 (9:G10) at $z_{\text{dla}} = 2.4592$ (continued). See Figure A1 for an explanation of the different line colors.

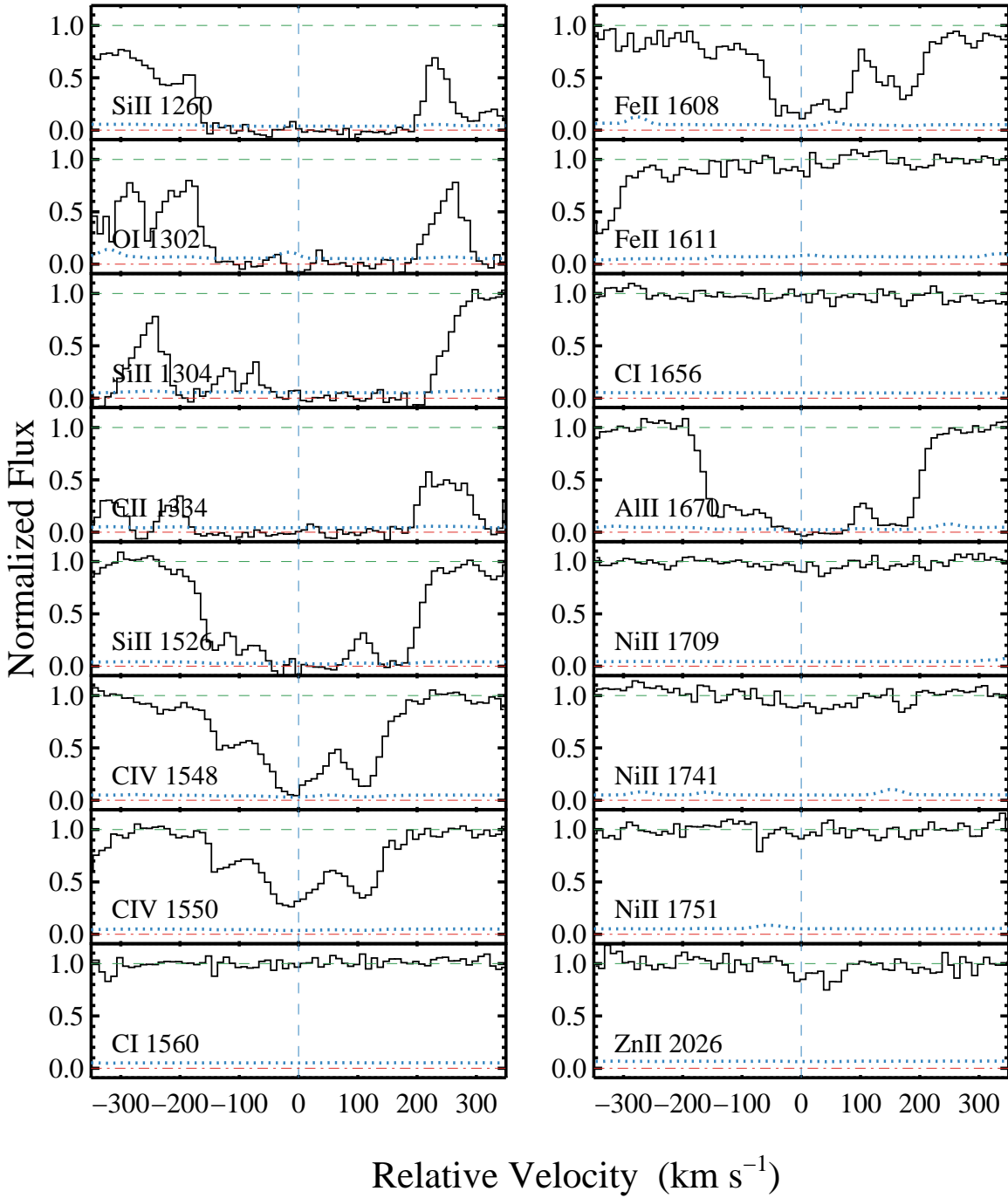


Figure A16. Velocity plot of the ion transitions associated to the DLA J0851+2332 (10:G11) at $z_{\text{dla}} = 3.5297$. See Figure A1 for an explanation of the different line colors.

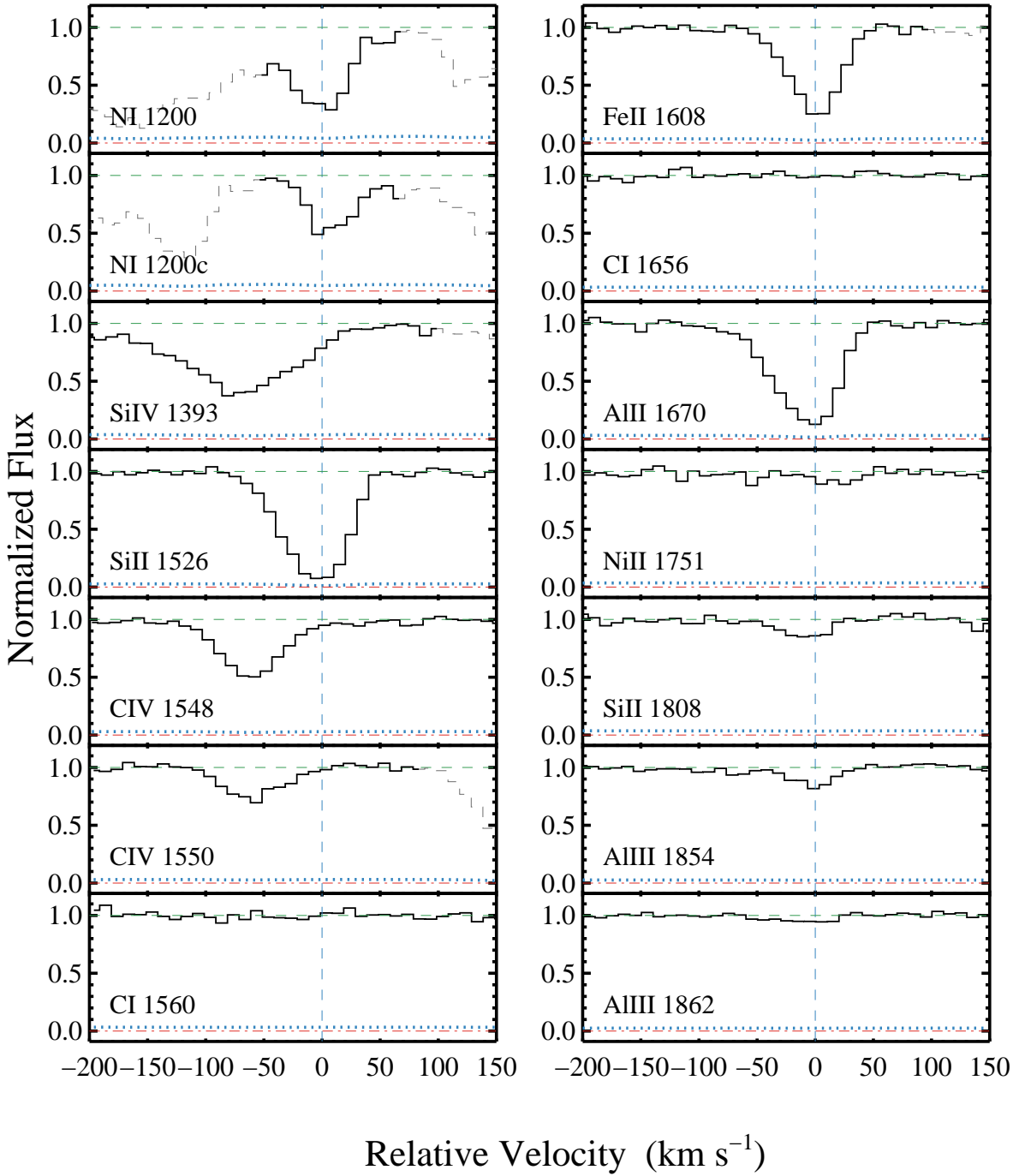


Figure A17. Velocity plot of the ion transitions associated to the DLA J0956+1448 (11:G12) at $z_{\text{dla}} = 2.6606$. See Figure A1 for an explanation of the different line colors.

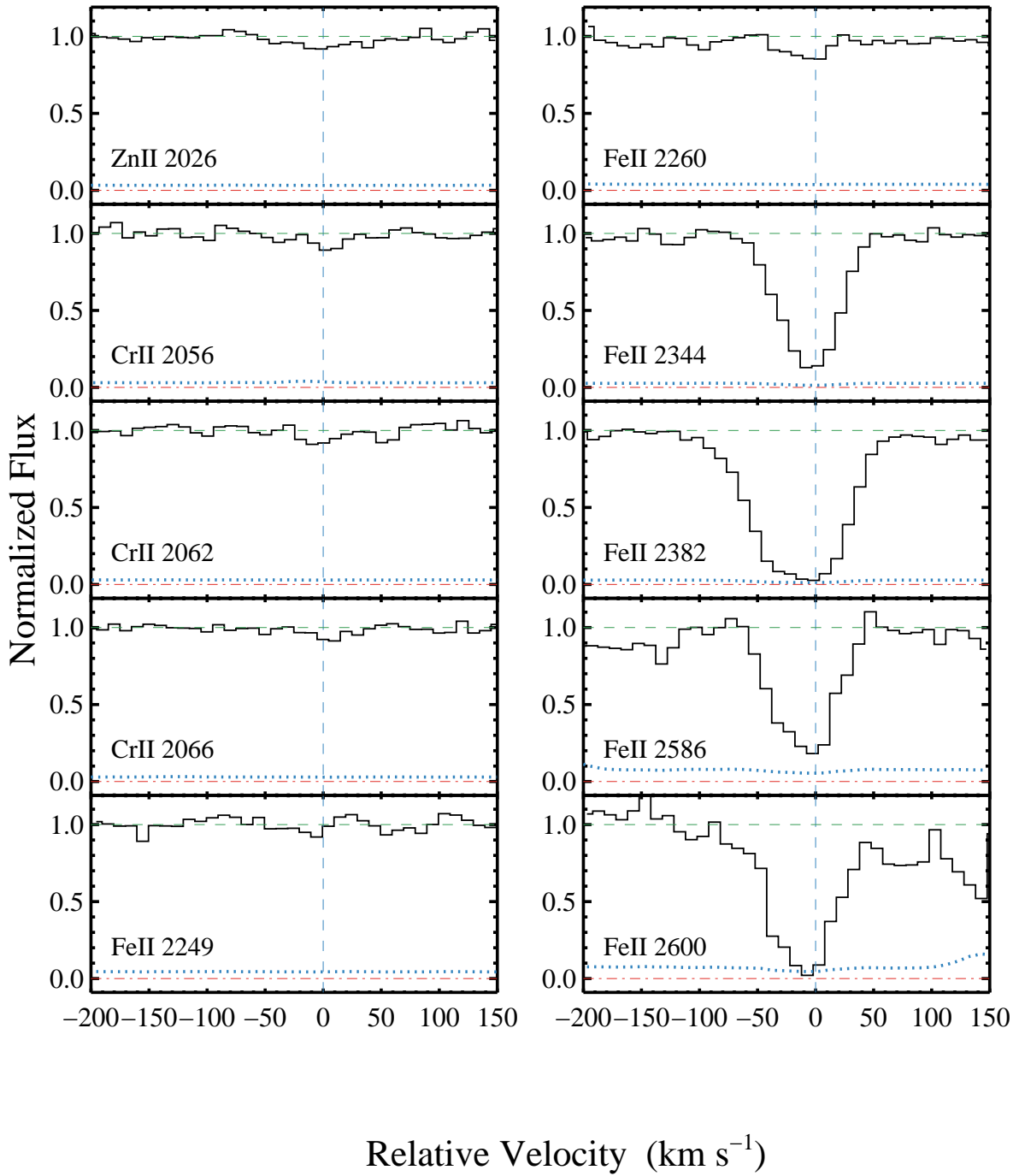


Figure A18. Velocity plot of the ion transitions associated to the DLA J0956+1448 (11:G12) at $z_{\text{dla}} = 2.6606$ (continued). See Figure A1 for an explanation of the different line colors.

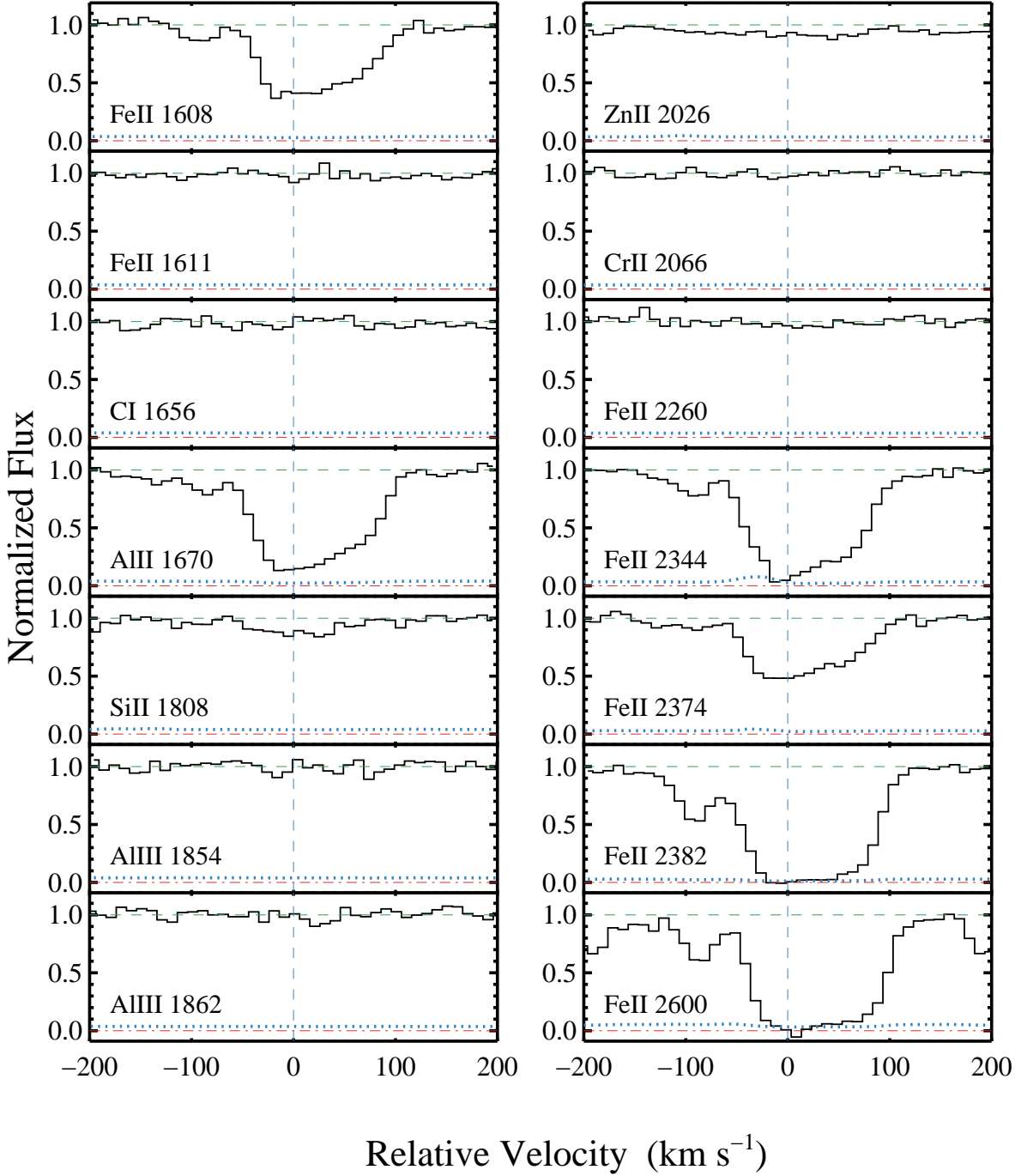


Figure A19. Velocity plot of the ion transitions associated to the DLA J1151+3536 (12:G13) at $z_{\text{dla}} = 2.5978$. See Figure A1 for an explanation of the different line colors.

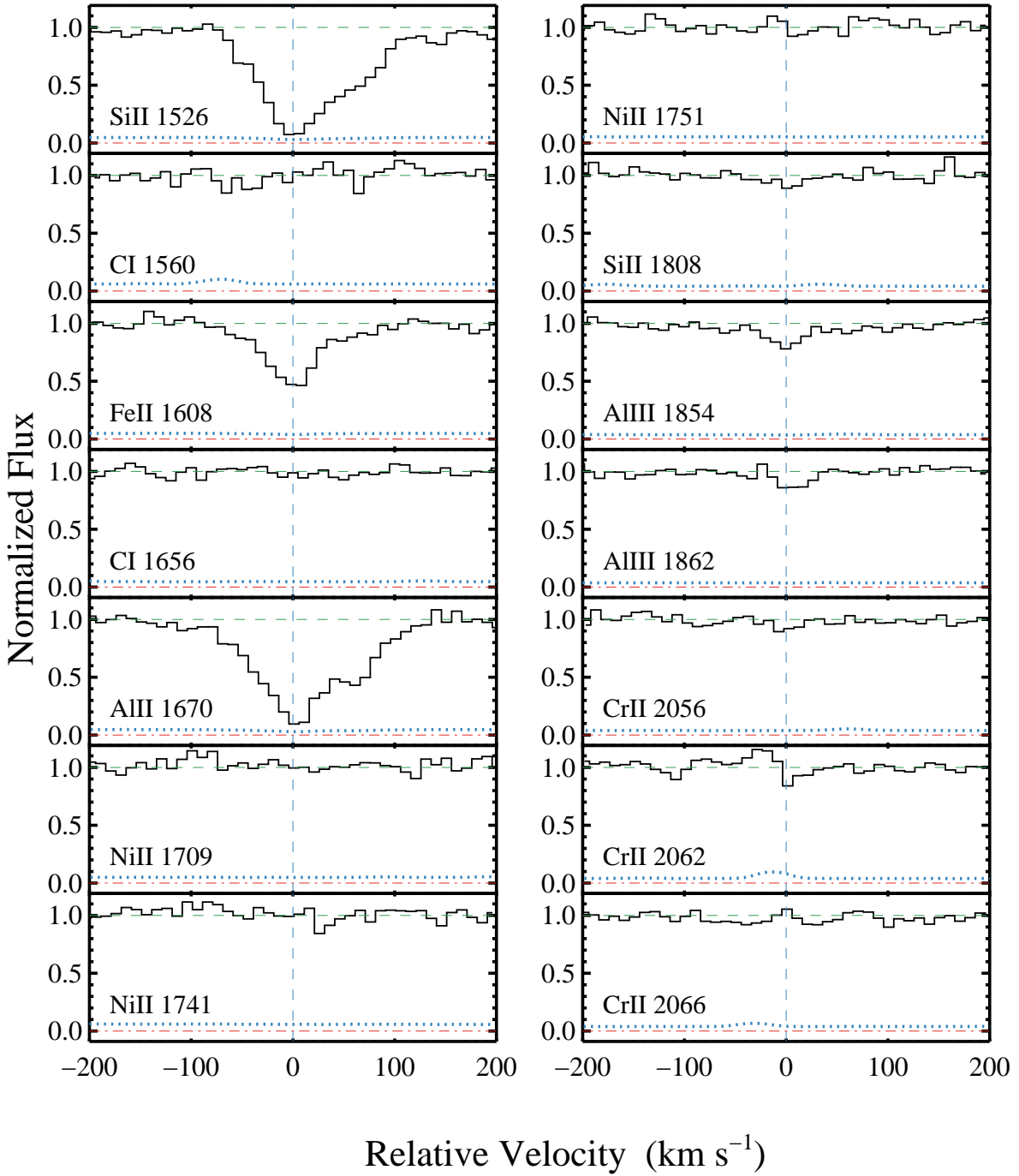


Figure A20. Velocity plot of the ion transitions associated to the DLA J2123-0053 (13:H1) at $z_{\text{dla}} = 2.7803$. See Figure A1 for an explanation of the different line colors.

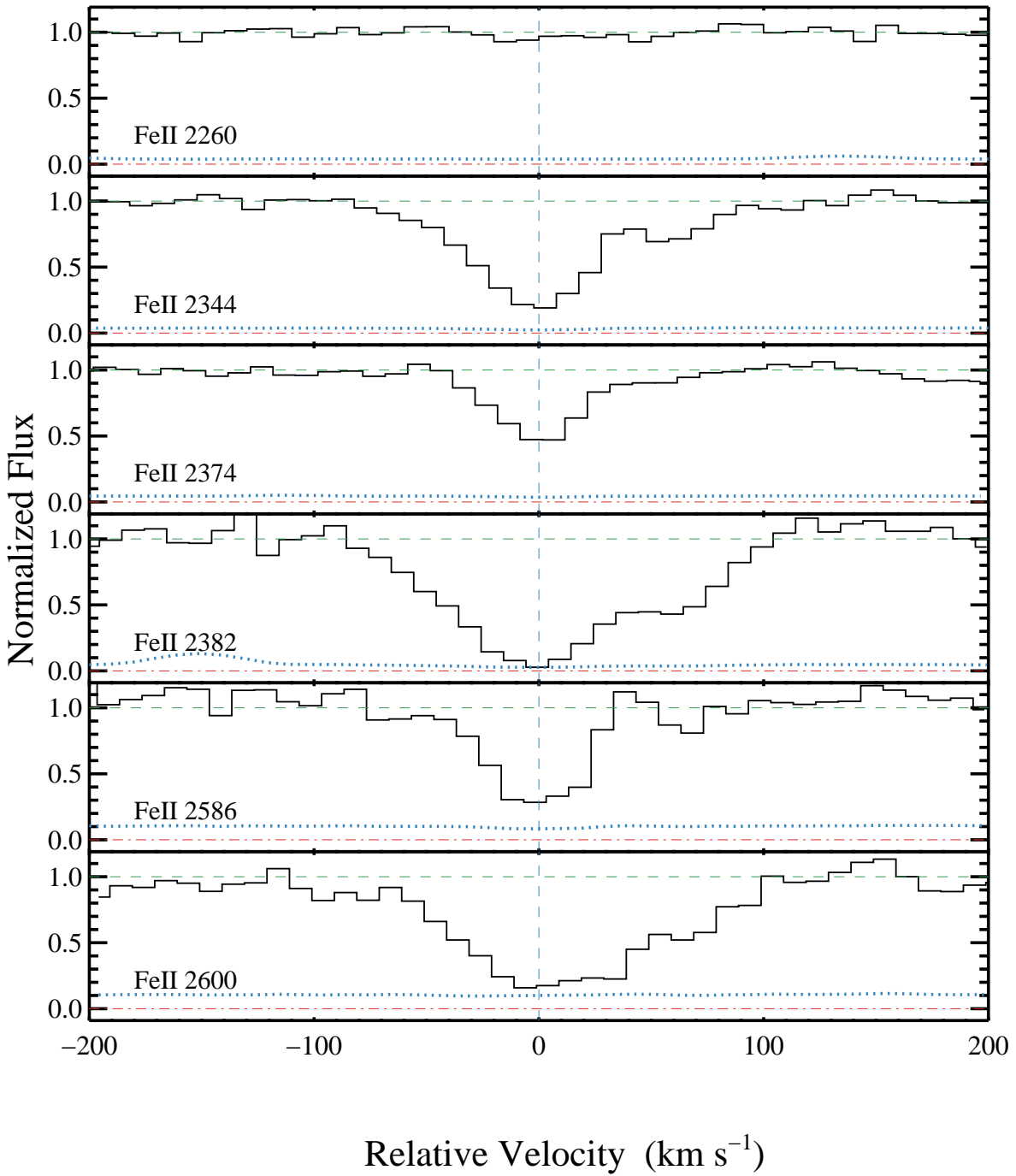


Figure A21. Velocity plot of the ion transitions associated to the DLA J2123-0053 (13:H1) at $z_{\text{dla}} = 2.7803$ (continued). See Figure A1 for an explanation of the different line colors.

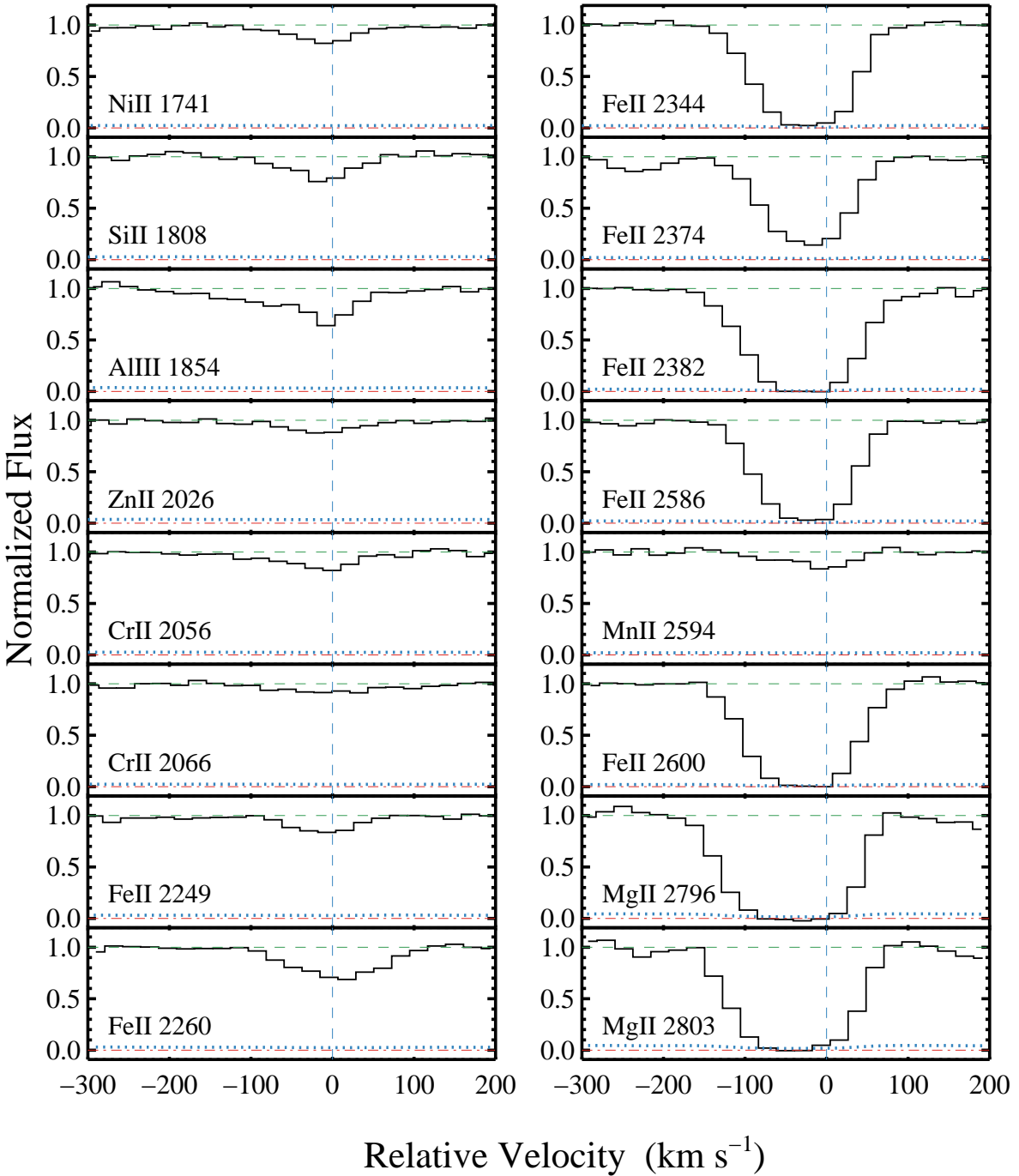


Figure A22. Velocity plot of the ion transitions associated to the DLA J0407-4410 (14:H2) at $z_{\text{dla}} = 1.9127$. See Figure A1 for an explanation of the different line colors.

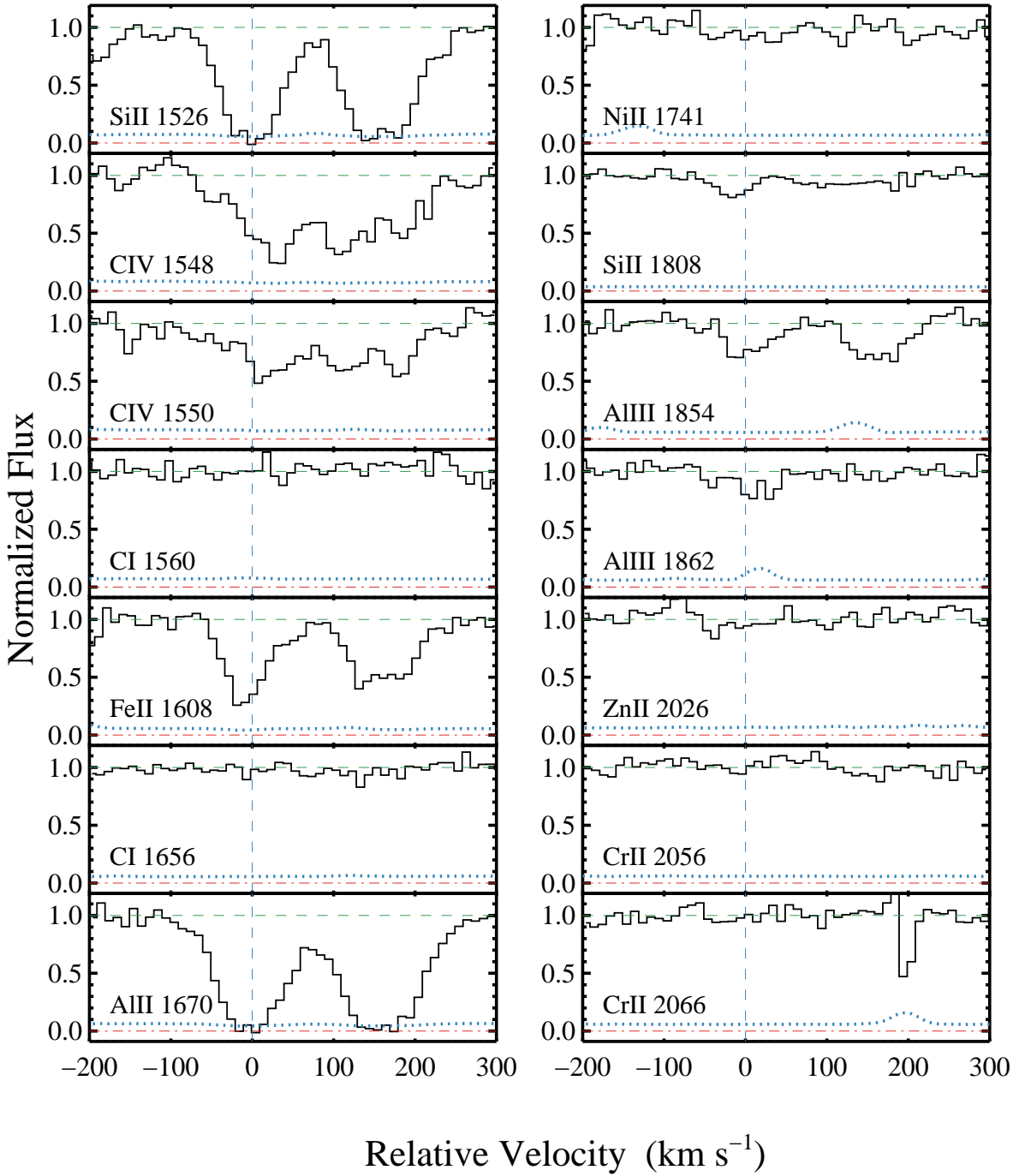


Figure A23. Velocity plot of the ion transitions associated to the DLA J0255+0048 (15:H3) at $z_{\text{dla}} = 3.2530$. See Figure A1 for an explanation of the different line colors.

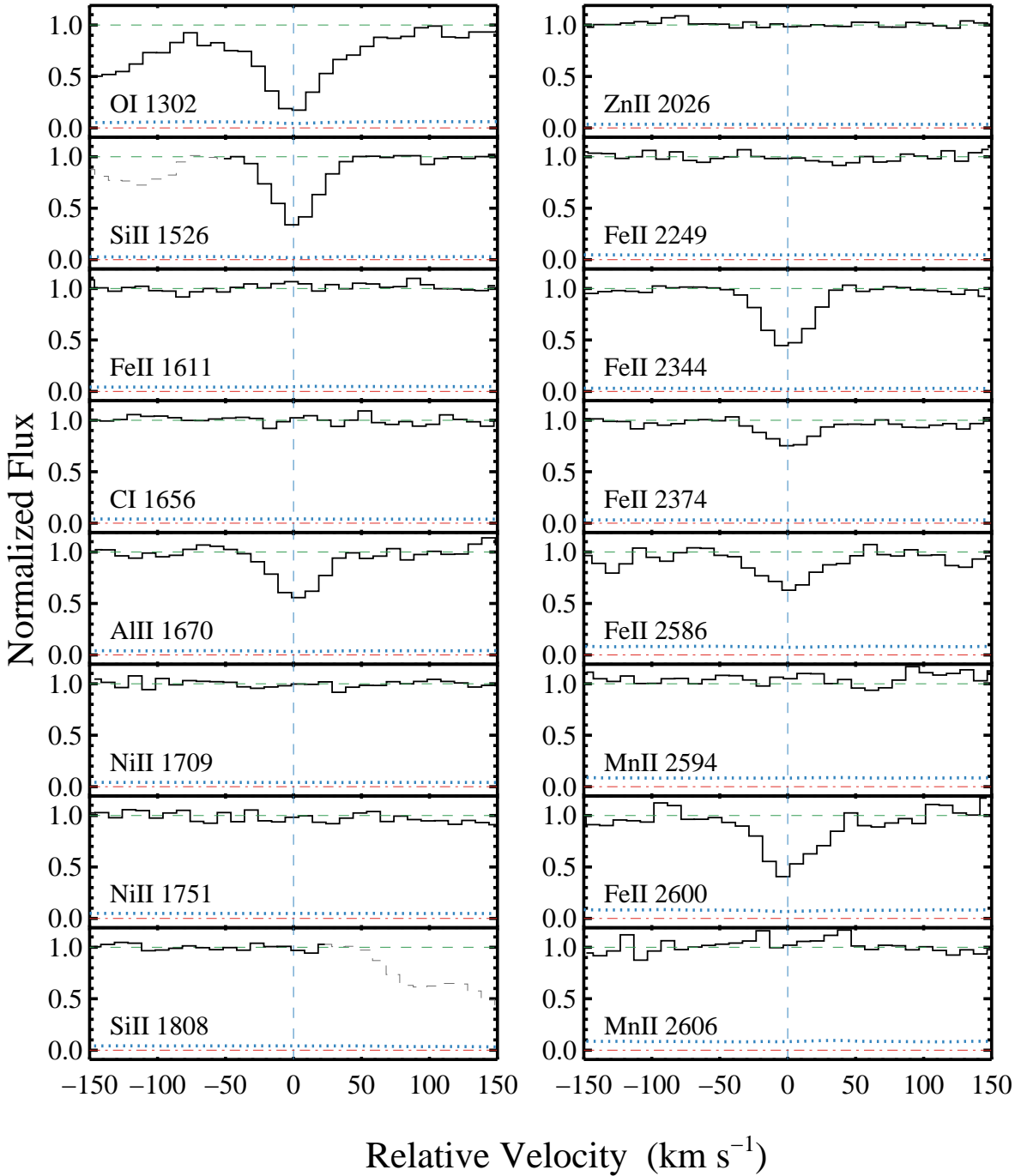


Figure A24. Velocity plot of the ion transitions associated to the DLA J0816+4823 (16:H4) at $z_{\text{dla}} = 2.7067$. See Figure A1 for an explanation of the different line colors.

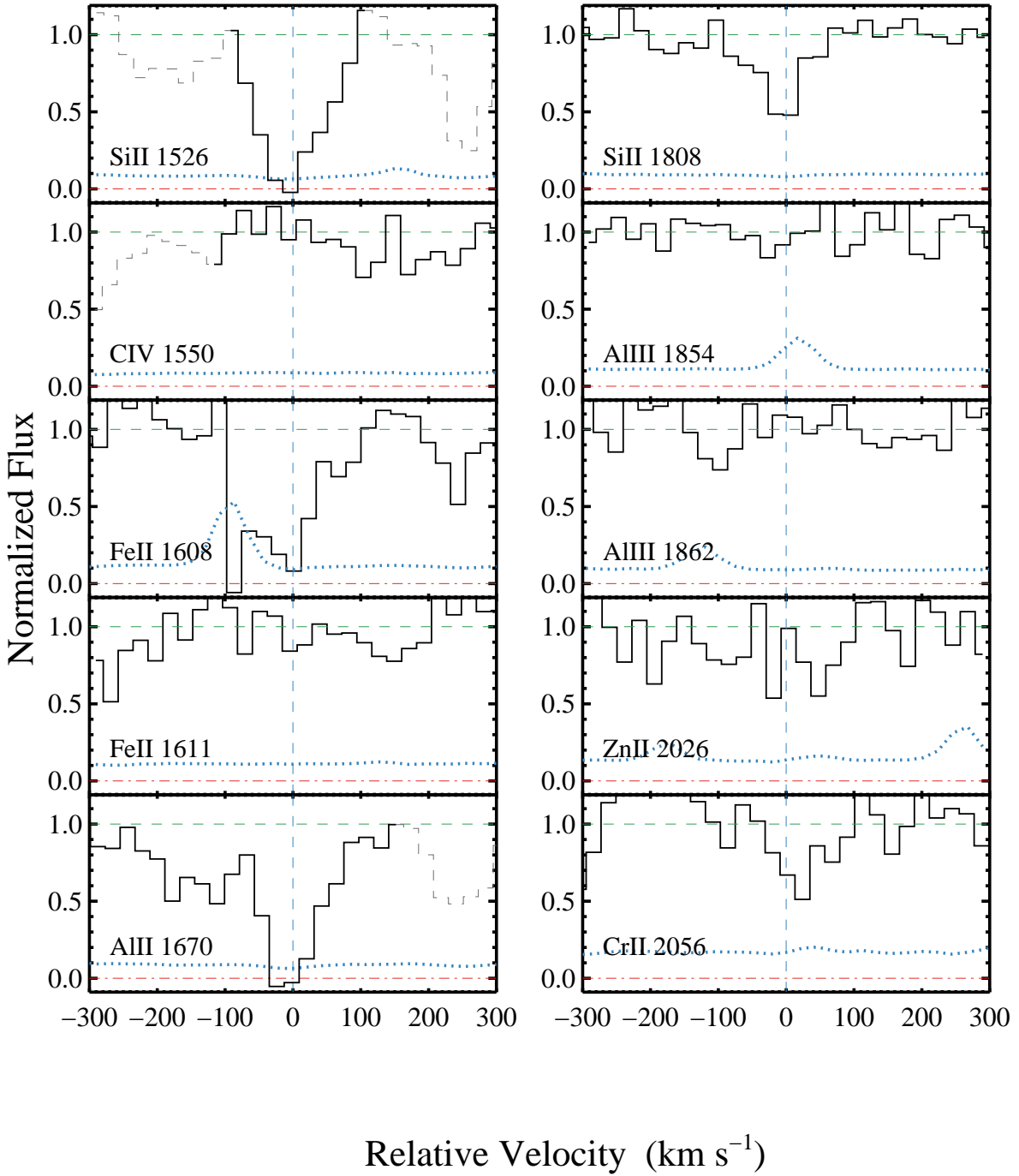


Figure A25. Velocity plot of the ion transitions associated to the DLA J0908+0238 (18:H6) at $z_{\text{dla}} = 2.9586$. See Figure A1 for an explanation of the different line colors.

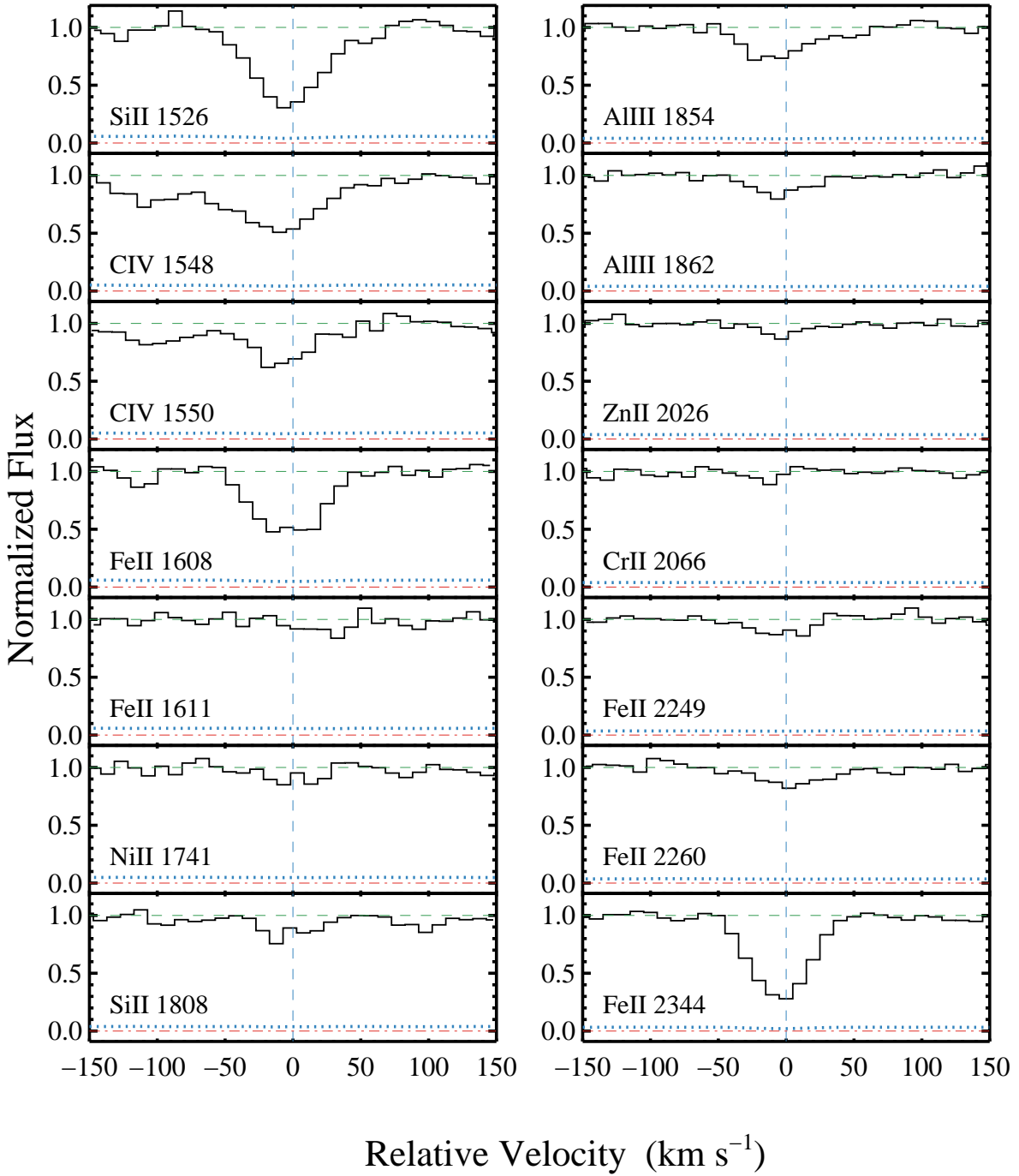


Figure A26. Velocity plot of the ion transitions associated to the DLA J0844+1245 (21:H9) at $z_{\text{dla}} = 1.8639$. See Figure A1 for an explanation of the different line colors.

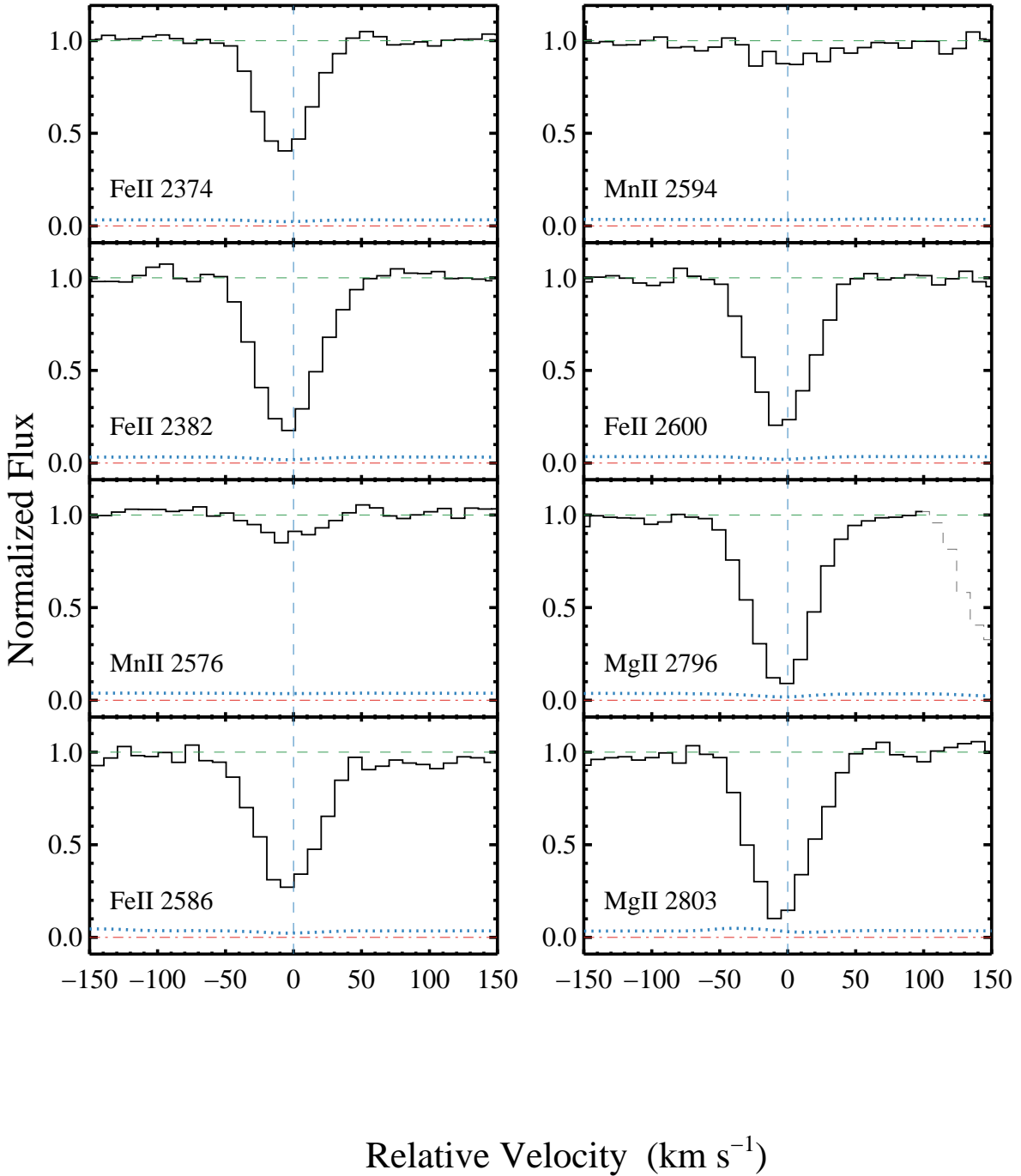


Figure A27. Velocity plot of the ion transitions associated to the DLA J0844+1245 (21:H9) at $z_{\text{dla}} = 1.8639$ (continued). See Figure A1 for an explanation of the different line colors.

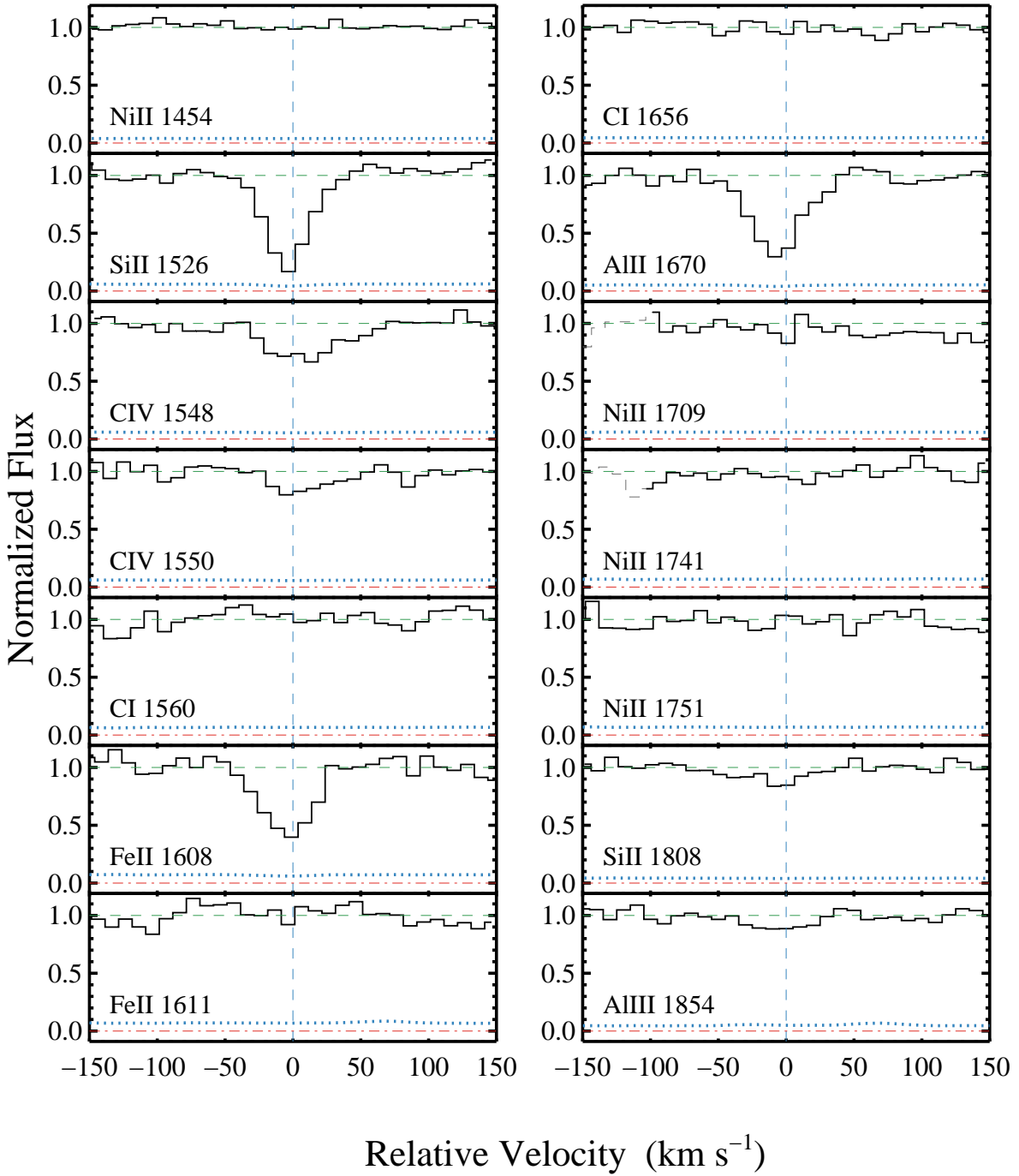


Figure A28. Velocity plot of the ion transitions associated to the DLA J0751+4516 (22:H10) at $z_{\text{dla}} = 2.6826$. See Figure A1 for an explanation of the different line colors.

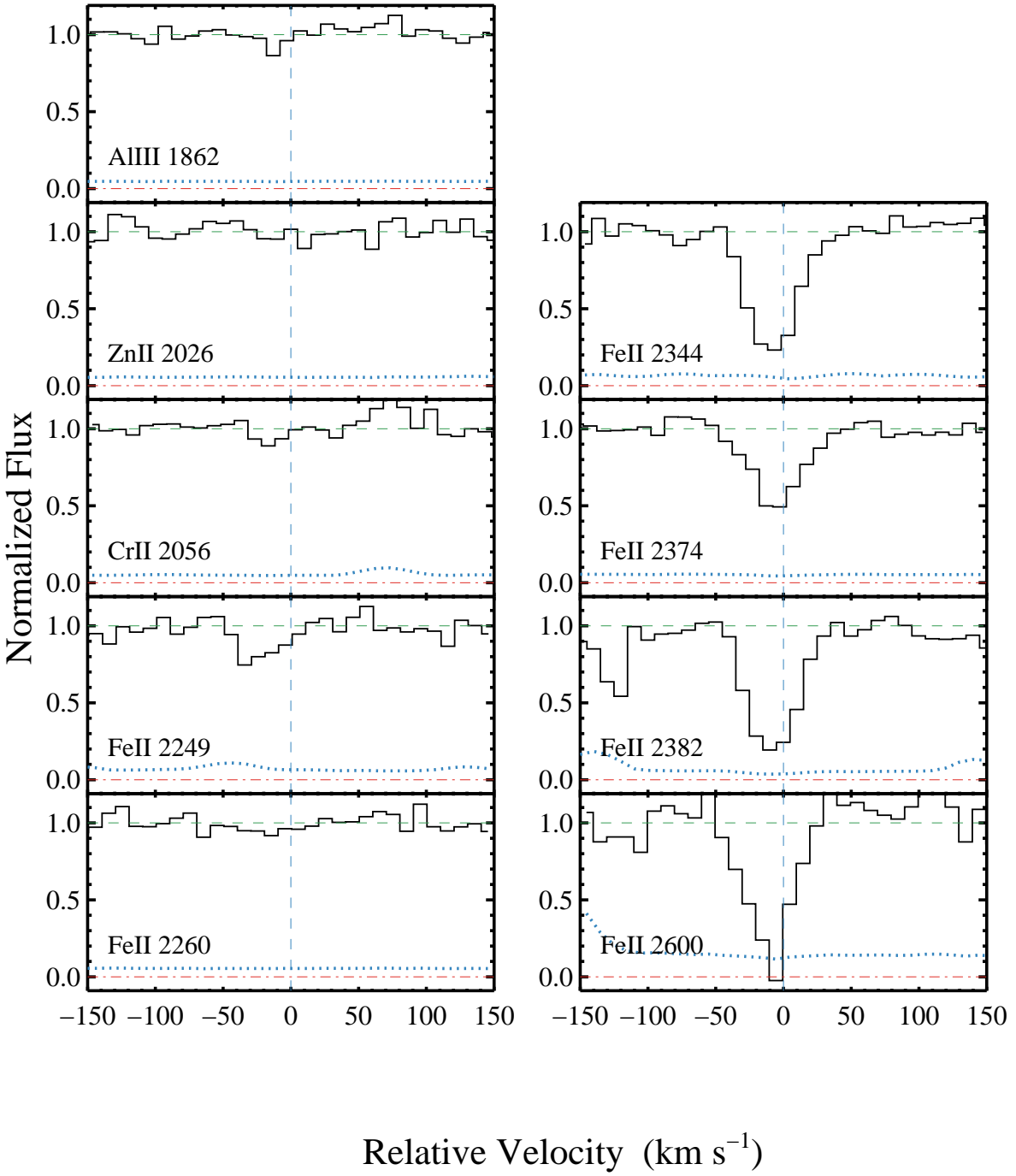


Figure A29. Velocity plot of the ion transitions associated to the DLA J0751+4516 (22:H10) at $z_{\text{dla}} = 2.6826$ (continued). See Figure A1 for an explanation of the different line colors.

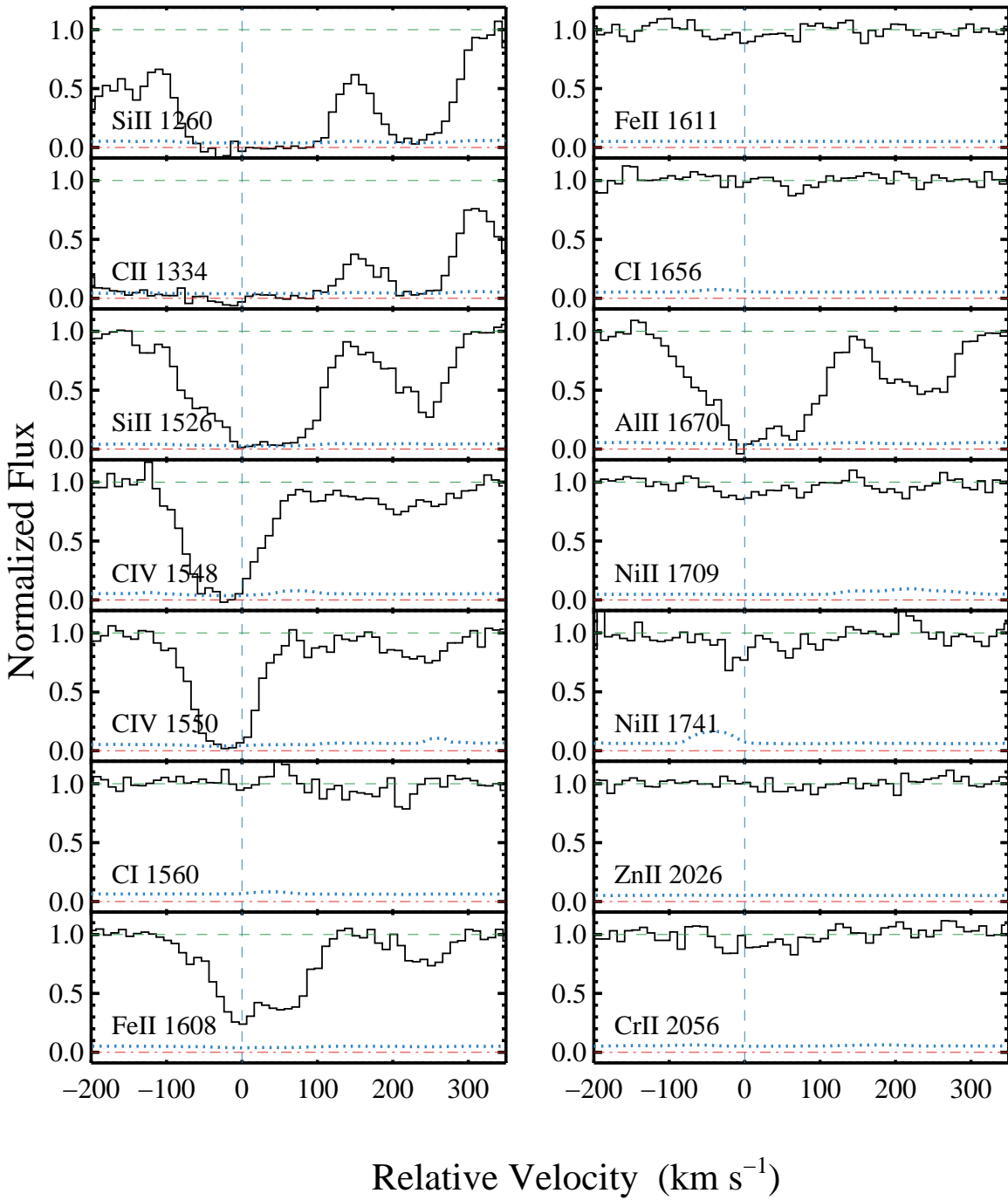


Figure A30. Velocity plot of the ion transitions associated to the DLA J0818+0720 (23:H11) at $z_{\text{dla}} = 3.2332$. See Figure A1 for an explanation of the different line colors.

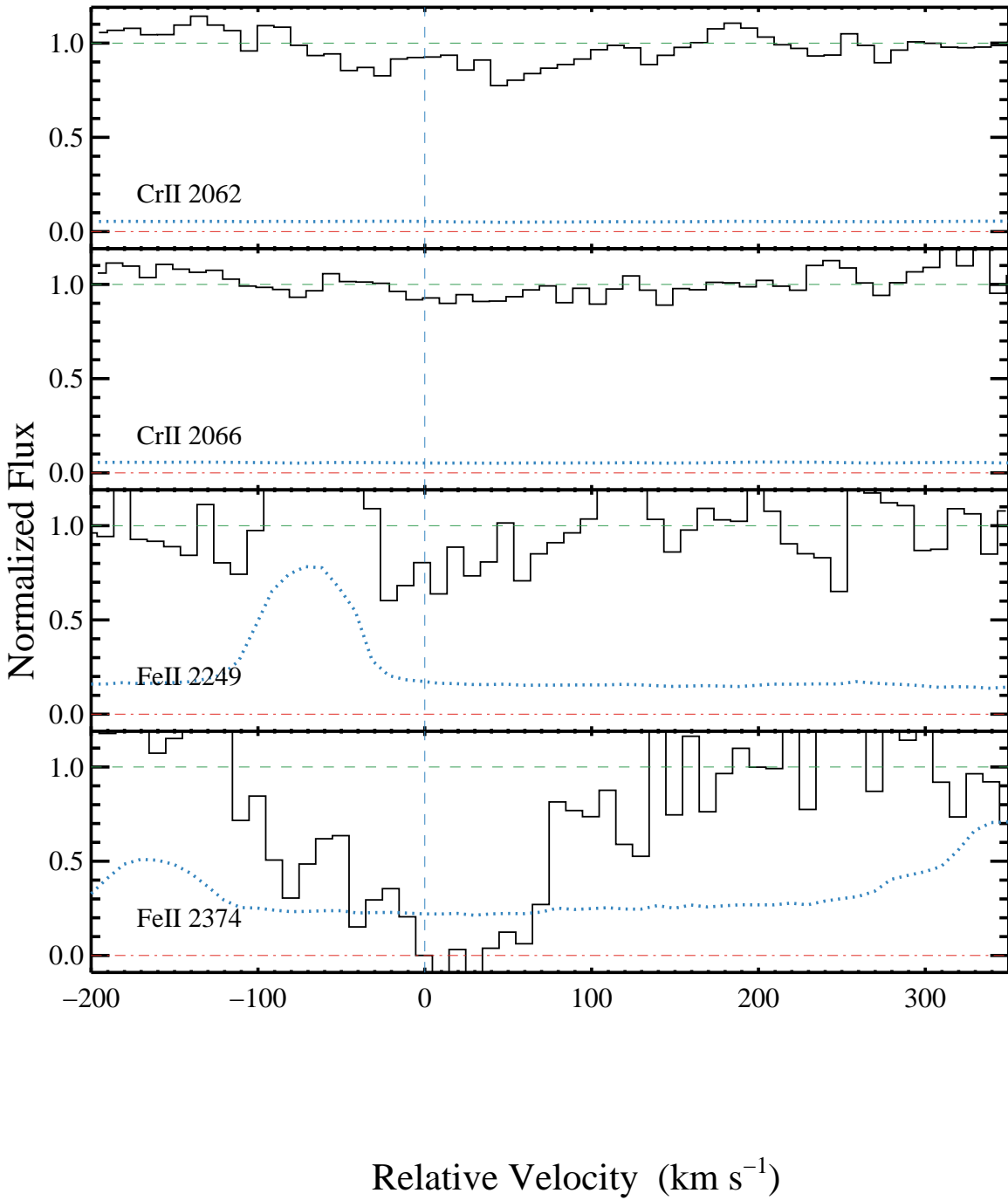


Figure A31. Velocity plot of the ion transitions associated to the DLA J0818+0720 (23:H11) at $z_{\text{dla}} = 3.2332$ (continued). See Figure A1 for an explanation of the different line colors.

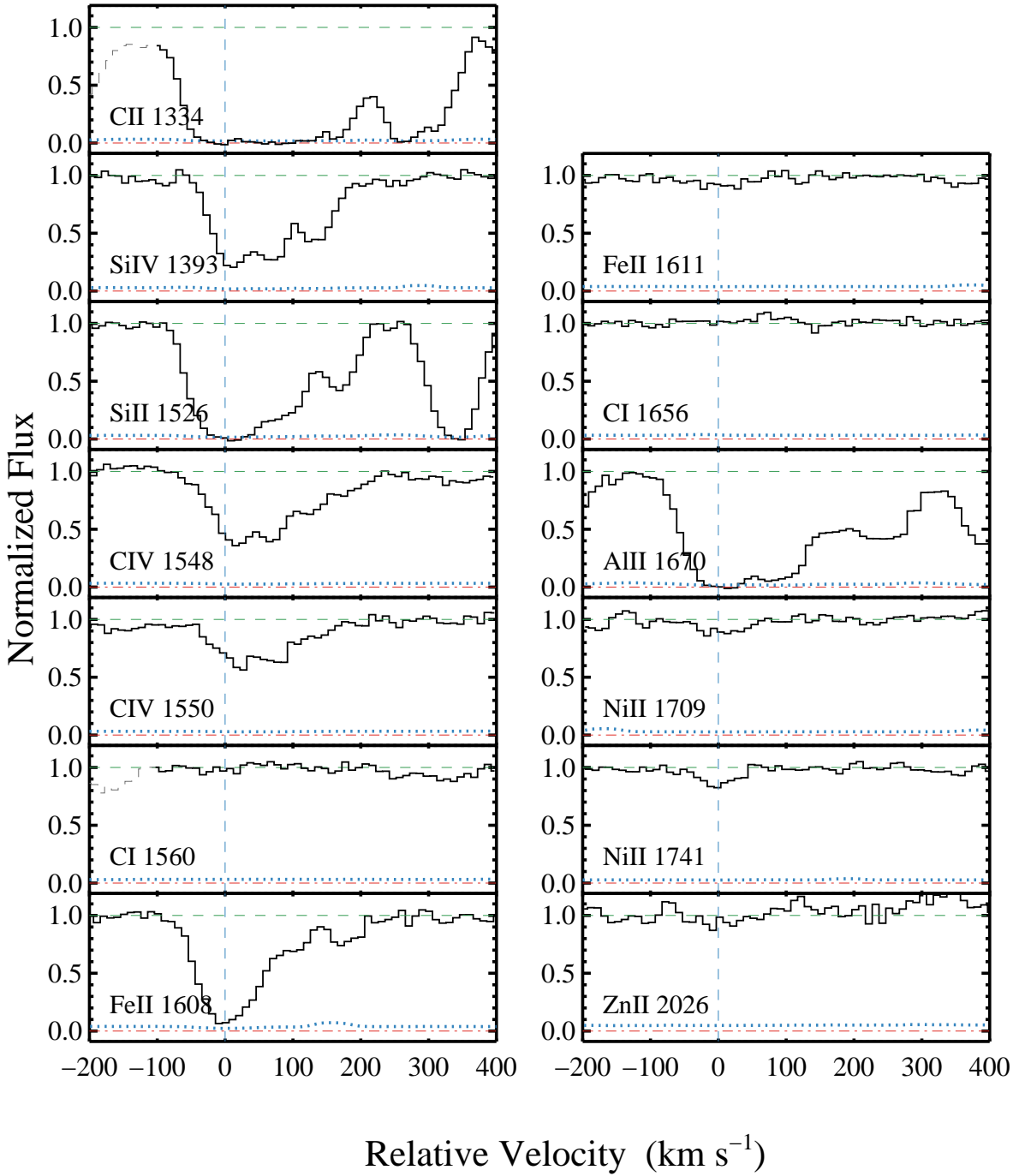


Figure A32. Velocity plot of the ion transitions associated to the DLA J0818+2631 (24:H12) at $z_{\text{dla}} = 3.5629$. See Figure A1 for an explanation of the different line colors.

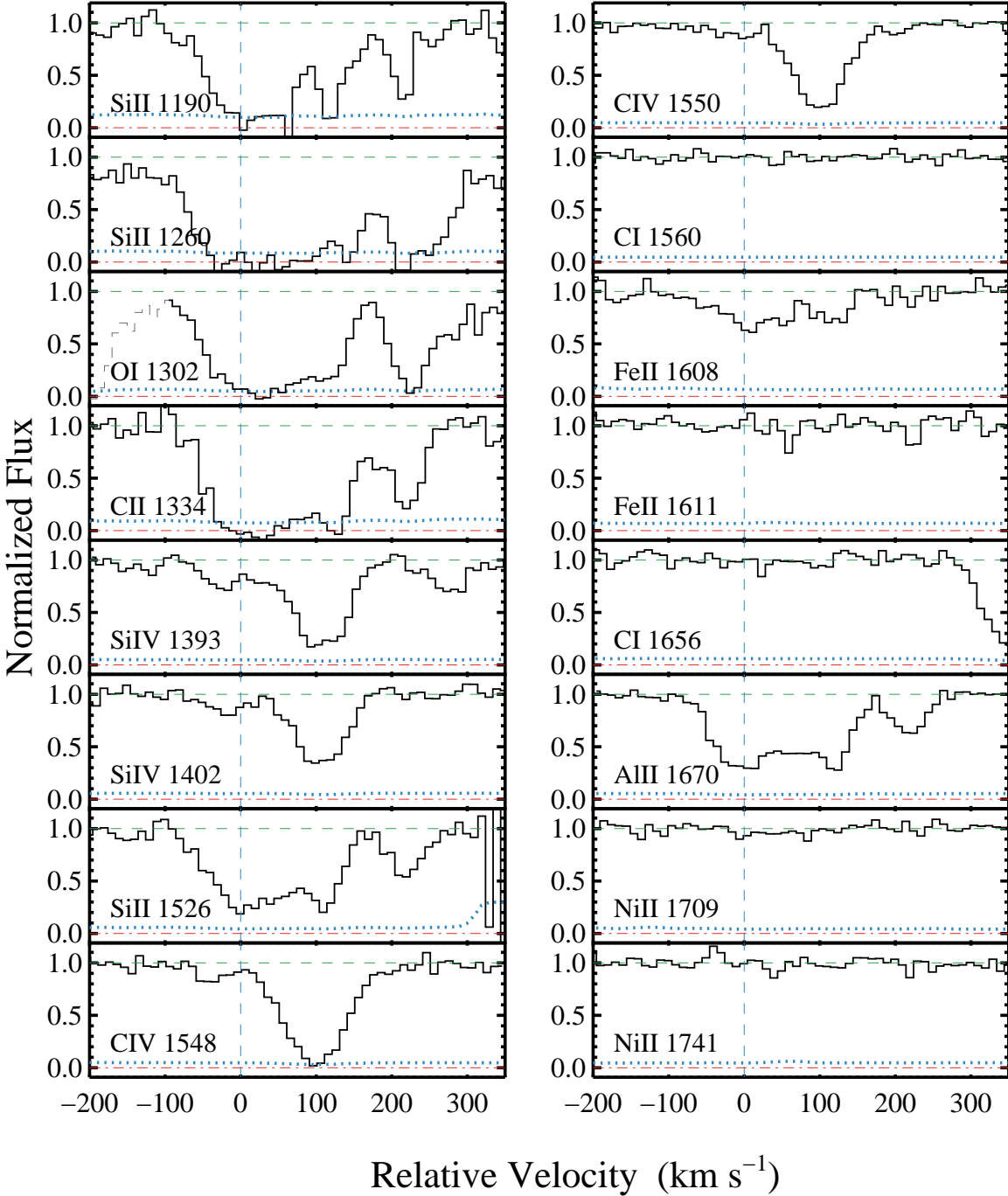


Figure A33. Velocity plot of the ion transitions associated to the DLA J0811+3936 (25:H13) at $z_{\text{dla}} = 2.6500$. See Figure A1 for an explanation of the different line colors.

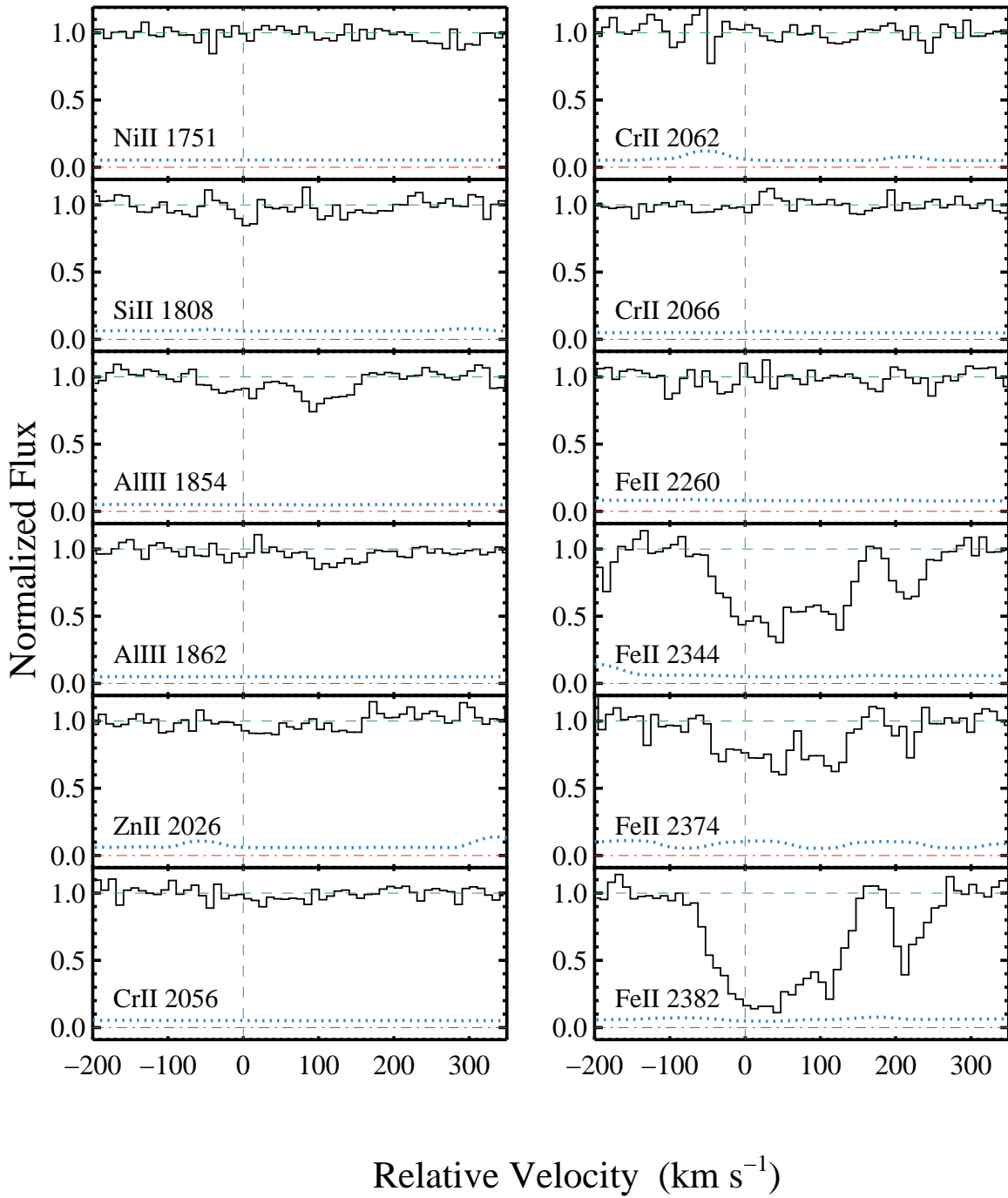


Figure A34. Velocity plot of the ion transitions associated to the DLA J0811+3936 (25:H13) at $z_{\text{dla}} = 2.6500$ (continued). See Figure A1 for an explanation of the different line colors.